AWARD NUMBERS: W81XWH-19-1-0807

TITLE: Targeting the Gut Microbiome to Treat Post-Traumatic Osteoarthritis

PRINCIPAL INVESTIGATOR: Michael Zuscik, PhD

CONTRACTING ORGANIZATION: University of Colorado at Denver

REPORT DATE: OCTOBER 2023

TYPE OF REPORT: Annual

PREPARED FOR: U.S. Army Medical Research and Development Command
Fort Detrick, Maryland 21702-5012

DISTRIBUTION STATEMENT: Approved for Public Release; Distribution Unlimited

The views, opinions and/or findings contained in this report are those of the author(s) and should not be construed as an official Department of the Army position, policy or decision unless so designated by other documentation.

REPORT DOCUMENTATION PAGE

Form Approved
OMB No. 0704-0188

Public reporting burden for this collection of information is estimated to average 1 hour per response, including the time for reviewing instructions, searching existing data sources, gathering and maintaining the data needed, and completing and reviewing this collection of information. Send comments regarding this burden estimate or any other aspect of this collection of information, including suggestions for reducing this burden to Department of Defense, Washington Headquarters Services, Directorate for Information Operations and Reports (0704-0188), 1215 Jefferson Davis Highway, Suite 1204, Arlington, VA 22202-4302. Respondents should be aware that notwithstanding any other provision of law, no person shall be subject to any penalty for failing to comply with a collection of information if it does not display a currently valid OMB control number. **PLEASE DO NOT RETURN YOUR FORM TO THE ABOVE ADDRESS.**

1. REPORT DATE	2. REPORT TYPE	3. DATES COVERED
OCTOBER 2023	Annual	15 Sep 2022 - 14 Sep 2023

4. TITLE AND SUBTITLE

Targeting the Gut Microbiome to Treat Post-Traumatic Osteoarthritis

5a. CONTRACT NUMBER
W81XWH-19-1-0807

5b. GRANT NUMBER

5c. PROGRAM ELEMENT NUMBER

6. AUTHOR(S)
Partnering PIs- Steven Gill, PhD and Michael Zuscik, PhD

E-Mail: MICHAEL.ZUSCIK@CUANSCHUTZ.EDU; STEVEN_GILL@URMC.ROCHESTER.EDU

5d. PROJECT NUMBER

5e. TASK NUMBER

5f. WORK UNIT NUMBER

7. PERFORMING ORGANIZATION NAME(S) AND ADDRESS(ES)

University of Colorado at Denver

1201 Larimer St, Denver, CO 80204

8. PERFORMING ORGANIZATION REPORT NUMBER

9. SPONSORING / MONITORING AGENCY NAME(S) AND ADDRESS(ES)

U.S. Army Medical Research and Development Command
Fort Detrick, Maryland 21702-5012

10. SPONSOR/MONITOR'S ACRONYM(S)

11. SPONSOR/MONITOR'S REPORT NUMBER(S)

12. DISTRIBUTION / AVAILABILITY STATEMENT

Approved for Public Release, Distribution Unlimited

13. SUPPLEMENTARY NOTES

14. ABSTRACT
Osteoarthritis (OA) is a debilitating condition with no disease modifying treatments. We have proposed that the gut microbiome may play a role in its development and progression, and thus may represent a target for treatment. The establishment of a disease modifying treatment of OA has immense ramifications, including improved quality of life, lowered economic burden of treatment, and increased productivity of patients with OA. The purpose of this project is to study the pathogenic role of the microbiome in the development of OA as well as to develop microbiome-targeting treatments of the disease. Fecal microbiota transplants (FMTs) will be used to examine the causal relationship between microbiome dysbiosis that may develop in veterans diagnosed with post-traumatic osteoarthritis (PTOA) and belonging to the Military and Veteran Microbiome: Consortium for Research and Education (MVM-CoRE). Recruitment of the Veterans into the study is completed, setting up analysis of their fecal samples using high dimensional approaches (underway at the time of this report) and FMTs in early 2024. Treatment of PTOA with microbiome pre and probiotics has been ongoing, and we find the dietary supplement hydrolyzed hylaline cartilage (hHC) to have protective effects on cartilage degeneration in a mouse model of PTOA. Progress on all these fronts is significant, with 3 manuscripts that are submitted or about to be submitted for peer review. Despite substantial institutional shutdowns caused by the COVID-19 pandemic, we are now moving ahead quickly, anticipating completion of all proposed aims by September of 2024.

15. SUBJECT TERMS

NONE LISTED

16. SECURITY CLASSIFICATION OF:			17. LIMITATION OF ABSTRACT	18. NUMBER OF PAGES	19a. NAME OF RESPONSIBLE PERSON
a. REPORT	b. ABSTRACT	c. THIS PAGE			USAMRDC
U	U	U	UU	153	19b. TELEPHONE NUMBER *(include area code)*

TABLE OF CONTENTS

	Page
1. Introduction	4
2. Keywords	5
3. Accomplishments	6
4. Impact	8
5. Changes/Problems	9
6. Products	10
7. Participants & Other Collaborating Organizations	12
8. Special Reporting Requirements	25
9. Appendix 1	26
10. Appendix 2	81
11. Appendix 3	106

1. Introduction

This project is focused on 1) studying the pathogenic role of the gut microbiome in the development of osteoarthritis (OA), and 2) developing approaches that target the gut microbiome to treat posttraumatic OA (PTOA), a disease that does not currently have an accepted disease modifying treatment. Our first objective was to study the microbiome dysbiosis that develops in a mouse model of PTOA and military veterans that have been diagnosed with PTOA and have been recruited into the Military and Veteran Microbiome: Consortium for Research and Education (MVM-CoRE). To prove the causal role of this dysbiosis, fecal microbiota transplants (FMTs) will be performed (mouse to mouse and human to mouse), and specific potentially pathogenic microbial species will be gavaged to pinpoint taxa that are PTOA-accelerating. Our second objective is to build on or historical work studying dietary supplements as disease modifiers for OA by examining the impact of daily supplementation with hydrolyzed hyaline cartilage (hHC) on PTOA progression and on the gut microbiome. Again, FMTs between supplemented and non-supplemented mice will test the causal role of the gut community in any joint protection that is observed, and specific microbial species will be studied as potentially active participants in the protective effects. Finally, in the third objective, we will focus on developing pre- and probiotic combinations for dietary supplements involving hHC and taxa identified in the second objective that promote joint protection and decelerated PTOA progression. Multiple dosing regimens will be tested, with the most protective combinations studies with deep analysis of the gut microbiome using cutting edge metagenomic, metatranscriptomic and metabolomic profiling to drill down on specific molecular fractions that are contributing to disease modification that we document. We have completed four years of work on this project, and despite a major interruption by the COVID-19 pandemic, we have continued to make progress in the first and second objectives, nearing completion of those studies, with work now moving forward on Aim 3. This progress is described below in the various sections of this report.

Note: This report provides information on the fourth year of a partnering-PI project, and the specific activity for each aspect of progress is dependent on activity from each contributing PI (CU for Zuscik, UR for Gill). In general, all OA analysis, animal work, and human work occurs at CU with PI Zuscik. All analysis of gut microbiome and microbiology work to expand and maintain taxa of interest is performed at UR with partnering PI Gill.

2. Key Words

Osteoarthritis (OA)
Posttraumatic osteoarthritis (PTOA)
Gut microbiome
Fecal microbiota transplant (FMT)
Military and Veteran Microbiome: Consortium for Research and Education (MVM-CoRE)
Hydrolyzed hyaline cartilage (hHC)
Destabilization of the medial meniscus (DMM)
Peptococcaceae *rc4-4*
Anaeroplasmataceae
Firmicutes
Tenericutes
Cartilage
Chondrocyte
Synovium
Tumor Necrosis Factor-alpha (TNF)

3. Accomplishments

- What were the major goals of the project?

The major goals of the project are 1) to define the role of the gut microbiome in PTOA, 2) to establish that hHC-induced chondroprotection in PTOA is due to effects on the gut microbiome, and 3) to test the efficacy of combined pre- and pro-biotic strategies to treat PTOA. Our aim is to accomplish these goals using state-of-the-art approaches and methods, culminating with a dataset supporting the effectiveness of gut microbiome interventions in treating PTOA and setting the stage for the first in-human trial work to test targeting of the gut microbiome as an OA disease modifying approach.

- What was accomplished under these goals?

i) Experiments have been performed to study the gut microbiome dysbiosis that occurs in PTOA (Objective #1). Using a mouse model of PTOA that involves surgical destabilization of the medial meniscus (DMM) to initiate PTOA, we have collected fecal samples weekly for 16s rDNA analysis, for study of the metagenome, metatranscriptome, and the metabolome. DMM surgeries were initially performed on a cohort of mice in January of 2020, but these samples were destroyed when the COVID-19 pandemic caused CU and UR to shut down operations in March of 2020. Mice, which were in mid-protocol, were euthanized because of the shutdown, essentially rendering collected samples unusable since the full experiment could not be performed. Once the Universities re-opened in the summer of 2020, a new cohort of mice was purchased, and DMMs were performed again in September of 2020. Collection protocols played out (CU), and terminal endpoints in December 2020 and January of 2021 provided fecal and cecal samples that we have now fully analyzed. Microbial 16S rDNA and metatranscriptomic analyses were carried out (UR), and interesting functional alterations were observed that correlate with metabolomic changes that were uncovered (CU). These findings are summarized in a poster from the 2022 Military Health System Research Symposium and the draft of a manuscript that is currently under development for submission to the journal *Arthritis Research and Therapy* (Appendix 1).

ii) To support humanization FMT experiments (Objective #1), an IRB-approved protocol was developed within the MVM-CoRE to collect fecal material from Veterans with a diagnosis of advanced knee osteoarthritis that are otherwise healthy, along with a cohort of healthy control participants. The goal was to enroll and collect samples from 20 for each group. In the end, we were able to collect 14 samples from the OA cohort, and 20 from the healthy cohort, which are currently under analysis (metagenome, metatranscriptome, metabolome). The stringent inclusion and exclusion criteria, which will enhance power to see gut microbiome differences between these cohorts, have made recruitment slower than expected. As a team, we have decided to proceed with the key experiments, which include deep analysis of the fecal material (metagenome, metatranscriptome, metabolome). Cohorts of experimental mice have just been purchased, and we will use these mice for humanization experiments in Objective 1. The humanization transplants will take place starting in November, 2023.

iii) We initiated work with hHC supplements in the past period of activity in the award (Objective #2 & #3). This work has led to a dataset that was presented at the American Society for Bone and Mineral Research conference, with an updated version of the dataset presented at the Orthopedic Research Symposium and D'Ambrosia Diversity Lectureship at the University of Colorado. The findings have been assembled into a manuscript, to be submitted to to the Journal *Nutrients*, which we have included in Appendix 2. This study, which involved quantifying the impact of hHC on PTOA (CU), provides the first data delineating the gut microbiome impact of this supplement (UR), setting the stage for our ongoing studies which involve isolation and expansion of several interesting taxa for in vivo work as a probiotic intervention, which in underway (CU and UR). The net results of this study were collected in the broader context of our work to study the role of the gut microbiome in the action of various nutraceutical products that set the stage for a publication in 2020, and a follow-on White Paper published in *Current Rheumatology Reports* at Springer Nature (see publications).

iv) Our overall focus on gut microbiome-joint connections has expanded over the past several years to include study of how consumption of the Western high fat diet and the development of obesity causes gut microbiome dysbiosis and activates systemic inflammation leading to accelerated OA. This has led to an additional manuscript that uncovers how obesity-induced dysbiosis leads to a novel B cell activation in the colon,

trafficking to the joint, and initiation of inflammation there. Although this work is ancillary to the aims of this project, it involved experimental groups that were pursued in parallel for the trauma-OA studies, and thus has led to datasets that are complimentary and informative. A manuscript is currently under revision at *JCI Insight*, (current version in Appendix 3)

- What opportunities for training and professional development have the project provided?

During years 3 and 4, we had two trainees that were involved in this project: predoctoral student David Villani and Instructor Honey Hendesi MD PhD. We had another postdoctoral fellow on the team in year 2 (Andrew Wu MD), but he graduated from the program and is currently in an Orthopaedic Residency at Johns Hopkins. We also have technical-level staff (Jake Guzetti and Emerald Saltyt) and an Instructor (Lacey Favazzo PhD) that help carry forward the work. These individuals are involved in all aspects of the management and execution of the experimental plan, and thus gain knowledge on how to administer a program of research, how to consider budgets in the context of the work, and scientific aspects of the project. This project-level training and professional development plays out in daily work on the project, weekly work in progress meetings and journal clubs associated with a T32 Training Grant (Zuscik, PI), and ultimately in the presentation of the work in broader contexts.

- How were the results disseminated to communities of interest?

Besides the 2 publications and 3 manuscripts nearing submission, we presented posters at the ORS, ASBMR, and our Regional Symposium. Some of the work was also presented at the Steadman Philippon Research Institute Science Summit in Vail, Colorado on August 22, 2023, at the University of Arizona (April 19, 2023), and at the University of Pennsylvania (May 25, 2023). In aggregate, these were our primary modes of dissemination.

- What do you plan to do in the next reporting period to accomplish the goals?

We plan to complete all remaining work on all objectives by September 2024. Key will be the completion of mouse-mouse FMTs (reciprocal transfers OA to non-OA and vice versa) and mouse humanization experiments with human fecal material collected from OA and non-OA patients enrolled in the MVM-CoRE.

4. Impact

- What was the impact on development of the principle disciplines of the project?

The central impact of the work so far:

- While the microbial community in the gut is not altered significantly by advanced PTOA in the mouse, the community's functional capacity is significantly altered; the first evidence of this unique phenotype (Appendix 1).
- Data generated on this project has provided the first evidence suggesting that nutraceutical supplements may impact joint health and OA degenerative disease via effects on the gut microbiome (Appendix 2). This is a novel concept that provides the first explanation for the purported effects of such agents in the context of joint homeostasis and disease.
- Further establishment of the concept that a dysbiotic and proinflammatory gut microbiome serves to create a proinflammatory environment in the knee and accelerate OA (Appendix 3).

- What was the impact on other disciplines?

Nothing to report.

- What was the impact on technology transfer?

Nothing to report.

- What was the impact on society beyond science and technology?

Nothing to report.

5. Changes/Problems

- Changes in approach and reasons for change.

Nothing to report.

- Actual or anticipated problems or delays and action plans to resolve them

We are in the final stages of the project. All work will be completed by September, 2024, with discussion of translating it to the TTDA or CTA mechanism with the PRMRP.

- Changes that have significant impact on expenditures

Nothing to report.

- Significant changes in use and care of human subjects, vertebrate animals, biohazards, and/or select agents.

Nothing to report.

6. Products

- Publications, conference papers and presentations

a. Publications during the active funding period:

Favazzo LJ, Hendesi H, Villani DA, et al. The gut microbiome-joint connection: implications in osteoarthritis. *Curr Opin Rheumatol*. Jan 2020;32(1):92-101.

Mobasheri A, Mahmoudian A, Kalvaityte U, Uzieliene I, Larder CE, Iskandar MM, Kubow S, Hamdan PC, de Almeida CS Jr, Favazzo LJ, van Loon LJC, Emans PJ, Plapler PG, Zuscik MJ. A White Paper on Collagen Hydrolyzates and Ultrahydrolyzates: Potential Supplements to Support Joint Health in Osteoarthritis? Curr Rheumatol Rep. 2021 Oct 30;23(11):78. doi: 10.1007/s11926-021-01042-6. PMID: 34716494; PMCID: PMC8556166.

Currently, three manuscripts are in various stages of development (see Appendices).

b. Books or other non-periodical, one-time publications

Nothing to report

c. Other publications, conference papers and presentations (Note: during the reporting period only):

David A Villani, Toru Ishii, Celia Xaverine Moneboulou Mbazoa, Honey Hendesi, Samantha H Landgrave, Karin Payne, Ann Gill, Lacey Favazzo, Steven R Gill, Michael Zuscik. Ablation of Monocyte Chemoattractant Protein-1 from the Intestinal Epithelium is Protective in the OA of Obesity. OARSI Conference, Denver, CO (Podium Presentation, March 2023, this award was acknowledged).

David A Villani, Toru Ishii, Honey Hendesi, Samantha H Landgrave, Ann Gill, Lisa Brenner, Lacey Favazzo, Steven R Gill, Michael Zuscik. Murine Posttraumatic Osteoarthritis Does Not Strongly Impact the Gut Microbiome Community Structure, But Significantly Alters the Functional Output of Resident Taxa. OARSI Conference, Denver, CO (Poster Presentation, March 2023, this award was acknowledged).

Zuscik MJ. From Gut to OA. University of Arizona, Department of Orthopaedics Grand Rounds, April 19, 2023. (Seminar Presentation, this award was acknowledged)

Zuscik MJ. Thinking Outside the Joint: Can Targeting the Intestine Support OA Disease Modification? University of Pennsylvania, Department of Orthopaedics Visiting Professor, May 25, 2023. (Seminar Presentation, this award was acknowledged)

David A Villani, Samantha H Landgrave, Honey Hendesi, Celia Xaverine Moneboulou Mbazoa, Toru Ishii, Ann Gill, Lacey Favazzo, Karin Payne, Steven R Gill, Michael Zuscik. Conditional Deletion of MCP1 in the Colonic Epithelium is Protective in the OA of Obesity, ASBMR Conference, Vancouver, B.C., Canada. (Oral Presentation, Young Investigator Award, October 2023, this award was acknowledged

Zuscik MJ. Thinking outside the joint: Can gut interventions support disease modification in OA? 8th Annual Vail Scientific Summit, Steadman Philippon Research Institute, August 22, 2023. (Seminar Presentation, this award was acknowledged)

- Website(s) or other internet site(s)

Nothing to report

- Technologies or techniques

Nothing to report

- Inventions, patent applications, and/or licenses

Nothing to report

- Other products

Nothing to report

7. Participants & Other Collaborating Organizations

- What individuals have worked on the project?

University of Colorado School of Medicine (Zuscik Partnering PI)

Name:	Michael Zuscik PhD
Project role:	Partnering PI
Researcher identifier:	0000-0003-0461-8708 (ORCID)
Nearest person month worked:	3
Contribution to project:	Contribution to design and planning of all aspects of the project
Funding support:	

Name:	Lisa Brenner PhD
Project role:	Co-I
Researcher identifier:	Not available
Nearest person month worked:	0.5
Contribution to project:	IRB development and planning for fecal collection from humans
Funding support:	

Name:	Honey Hendesi MD PhD
Project role:	Instructor-level significant contributor
Researcher identifier:	Not available
Nearest person month worked:	6
Contribution to project:	Contribution to design, planning and execution of all aspects of the project
Funding support:	

Name:	David Villani
Project role:	Graduate student
Researcher identifier:	Not available
Nearest person month worked:	12
Contribution to project:	Contribution to design, planning and execution of all aspects of the project
Funding support:	

Name:	Kelly Stearns-Yoder
Project role:	Clinical Coordinator
Researcher identifier:	Not available
Nearest person month worked:	0.6

Contribution to project:	IRB development
Funding support:	

Name:	Jake Guzzetti and Emerald Saltyt
Project role:	Clinical Coordinators
Researcher identifier:	Not available
Nearest person month worked:	1.8
Contribution to project:	IRB development, recruitment, and sample collection
Funding support:	

University of Rochester School of Medicine and Dentistry (Gill Partnering PI)

Name:	Steven Gill PhD
Project role:	Partnering PI
Researcher identifier:	0000-0002-2408-1373 (ORCID)
Nearest person month worked:	3
Contribution to project:	Contribution to design, planning and execution of all aspects of the project, particularly as related to microbiome analysis and microbiology work.
Funding support:	

Name:	Ann Gill MS
Project role:	Senior technical associate
Researcher identifier:	Not available
Nearest person month worked:	6
Contribution to project:	Contribution to microbiome analysis and microbiology work.
Funding support:	

Name:	Cal Palumbo MS
Project role:	Bioinformatician and Data Analyst
Researcher identifier:	Not available
Nearest person month worked:	2.4
Contribution to project:	Contribution to microbiome analysis.
Funding support:	

- Has there been a change in the active other support of the PD/PI(s) or senior/key personnel since the last reporting period?

A summary of active support for each PI is listed below.

Zuscik

*Title: AIM-for-RA
*Major Goals: The goal of this project is to implement a multidisciplinary team for RA patient recruitment, longitudinal clinical data accrual, and synovial biopsy tissue analysis for the molecular deconstruction and reconstruction of disease pathogenesis.
*Status of Support: Active
Project Number: 1UC2AR081025-01
Name of PD/PI: Moreland, L. (PI); Anolik, J. (Contact PI)
*Source of Support: NIAMS
*Primary Place of Performance: University of Rochester and University of Colorado Denver
Project/Proposal Start and End Date: (MM/YYYY) (if available): 3/2022 – 12/2026
*Total Award Amount (including Indirect Costs): (subcontract)
*Person Months (Calendar/Academic/Summer) per budget period.

Year (YYYY)	Person Months (##.##)
2. 2023	0.17 calendar
3. 2024	0.17 calendar
4. 2025	0.17 calendar
5. 2026	0.17 calendar

*****NO OVERLAP*****

*Title: Interdisciplinary Training in Musculoskeletal Research
*Major Goals: This training program establishes a curriculum and various education elements to support pre- and post-doctoral training in musculoskeletal research, with 4 funded pre-doctoral seats and 2 funded post-doctoral seats.
*Status of Support: Active
Project Number: T32AR080630-01
Name of PD/PI: Zuscik, M. (Contact PI)
*Source of Support: NIAMS
*Primary Place of Performance: University of Colorado Denver
Project/Proposal Start and End Date: (MM/YYYY) (if available): 07/2022 – 06/2027
*Total Award Amount (including Indirect Costs):
*Person Months (Calendar/Academic/Summer) per budget period.

Year (YYYY)	Person Months (##.##)
2. 2023	2.4 calendar
3. 2024	2.4 calendar
4. 2025	2.4 calendar
5. 2026	2.4 calendar

*****NO OVERLAP*****

*Title: Studies on gut microbiome-joint connections in arthritis
*Major Goals: This project aims to 1) definitively establish that a pro-inflammatory dysbiotic gut microbiome is causal in the osteoarthritis of obesity, and 2) demonstrate that correction of this dysbiosis using strategies to expand B. pseudolongum will decelerate the progression of osteoarthritis in the obese context.
*Status of Support: Active
Project Number: 5R01AR078414-02
Name of PD/PI: Zuscik, M. (Contact PI)
*Source of Support: NIAMS
*Primary Place of Performance: University of Colorado Denver
Project/Proposal Start and End Date: (MM/YYYY) (if available): 04/2021 – 02/2026
*Total Award Amount (including Indirect Costs):
*Person Months (Calendar/Academic/Summer) per budget period.

Year (YYYY)	Person Months (##.##)
2. 2023	3.0 calendar
3. 2024	3.0 calendar

Year (YYYY)	Person Months (##.##)
4. 2025	3.0 calendar
5. 2026	3.0 calendar

*****NO OVERLAP*****

*Title: Collaborative Research: RECODE: Organoid model of growth plate development
*Major Goals: This research will provide fundamental insight into the mechanisms that govern stem cell differentiation and organization into a mature, functional growth plate organoid.
*Status of Support: Active
Project Number: NSF 2135032
Name of PD/PI: Payne, K.A. (PI), Zuscik, M. (Co-PI)
*Source of Support: National Science Foundation
*Primary Place of Performance: University of Colorado Denver
Project/Proposal Start and End Date: (MM/YYYY) (if available): 12/2021 – 11/2025
*Total Award Amount (including Indirect Costs):
*Person Months (Calendar/Academic/Summer) per budget period.

Year (YYYY)	Person Months (##.##)
2. 2023	0.6 calendar
3. 2024	0.6 calendar
4. 2025	0.6 calendar

*****NO OVERLAP*****

(Reduced effort from 2.40 calendar months to 1.20 calendar months)
*Title: Development of Chondroregenerative Therapy for Human Osteoarthritis
*Major Goals: This phase II, double blind, placebo controlled clinical trial will determine if teriparatide is chondroregenerative in early-mid stage osteoarthritis in humans.
*Status of Support: Active
Project Number: Hansjörg Wyss Award
Name of PD/PI: Zuscik, M.
*Source of Support: Wyss Medical Foundation & Eli Lilly LLC
*Primary Place of Performance: University of Rochester and Duke University
Project/Proposal Start and End Date: (MM/YYYY) (if available): 11/2016 – 12/2023
*Total Award Amount (including Indirect Costs):
*Person Months (Calendar/Academic/Summer) per budget period.

Year (YYYY)	Person Months (##.##)
7. 2023	1.20 calendar

*****NO OVERLAP*****

*Title: Investigation of the joint protective effect of hydrolyzed hyaline cartilage (hHc)
*Major Goals: This phase II, double blind, placebo controlled clinical trial will determine if hHC, via prebiotic effects playing out in the gut microbiome, is chondroprotective in early-mid stage osteoarthritis in humans.
*Status of Support: Active
Project Number: Contract Agreement 200709
Name of PD/PI: Zuscik, M.
*Source of Support: Rousselot BVBA
*Primary Place of Performance: University of Colorado Denver
Project/Proposal Start and End Date: (MM/YYYY) (if available): 01/2021 – 12/2023
*Total Award Amount (including Indirect Costs):
*Person Months (Calendar/Academic/Summer) per budget period.

Year (YYYY)	Person Months (##.##)
3. 2023	1.0 calendar

*****NO OVERLAP*****

THIS AWARD:

*Title: Targeting the gut microbiome to treat posttraumatic osteoarthritis
*Major Goals: The goal of this project is to study the role of the gut microbiome in the chondroprotective effects of oral dietary supplements containing hydrolyzed type I collagen in posttraumatic osteoarthritis.
*Status of Support: Active
Project Number: W81XWH-19-1-0807
Name of PD/PI: Zuscik, M. (PI) and Gill, S. (Partnering PI)
*Source of Support: Department of the Army
*Primary Place of Performance: University of Colorado Denver
Project/Proposal Start and End Date: (MM/YYYY) (if available): 09/2019 – 09/2023
*Total Award Amount (including Indirect Costs):
*Person Months (Calendar/Academic/Summer) per budget period.

Year (YYYY)	Person Months (##.##)
4. 2023	3.0 calendar

*Title: Abaloparatide as the first chondroregenerative therapy for osteoarthritis
*Major Goals: This project focuses on study of the role of the chondrocyte in the joint preserving effects of abaloparatide, along with in vitro experiments to study the effects of abaloparatide in human articular chondrocytes.
*Status of Support: Active
Project Number: Grubstake 03-2021
Name of PD/PI: Zuscik, M.
*Source of Support: Gates Center for Regenerative Medicine
*Primary Place of Performance: University of Colorado Denver
Project/Proposal Start and End Date: (MM/YYYY) (if available): 01/2021 – 12/2023
*Total Award Amount (including Indirect Costs):
*Person Months (Calendar/Academic/Summer) per budget period.

Year (YYYY)	Person Months (##.##)
3. 2023	0.6 calendar

*****NO OVERLAP*****

*Title: Regulation of microRNA homeostasis: Implications in bone fracture healing
*Major Goals: This work will energize the development of novel therapeutic approaches tailored to correct the specific bone-healing defect that manifests in the obese/type 2 diabetic patients.
*Status of Support: Active
Project Number: 5R01DK121327-04
Name of PD/PI: Elbarbary, R. (PI), Zuscik, M. (Consultant)
*Source of Support: NIDDK
*Primary Place of Performance: Pennslyvania State University
Project/Proposal Start and End Date: (MM/YYYY) (if available): 09/2019 – 06/2024
*Total Award Amount (including Indirect Costs):
*Person Months (Calendar/Academic/Summer) per budget period.

Year (YYYY)	Person Months (##.##)
4. 2023	0.12 calendar
5. 2024	0.12 calendar

*****NO OVERLAP*****

*Title: Therapeutic Targeting of GPCR Gbetagamma-GRK2 in Osteoarthritis
*Major Goals: This study is to determine if Gbetagamma/GRK2 signaling inhibition, either genetically or via inhibitors is protective in osteoarthritis.
*Status of Support: Active
Project Number: 5R01AR071968-04
Name of PD/PI: Kamal, F. (PI), Zuscik, M. (Consultant)
*Source of Support: NIAMS
*Primary Place of Performance: Pennslyvania State University
Project/Proposal Start and End Date: (MM/YYYY) (if available): 02/2019 – 12/2023

* Total Award Amount (including Indirect Costs):
* Person Months (Calendar/Academic/Summer) per budget period.

Year (YYYY)	Person Months (##.##)
4. 2023	0.12 calendar

*****NO OVERLAP*****

*Title: Defining the Unique Synovial Transcriptome and Proteome of Ankle Post-traumatic Osteoarthritis
*Major Goals: Our proposal aim is to further elucidate synovium's role in the development of fracture-induced ankle post-traumatic osteoarthritis (PTOA).
*Status of Support: Active
Project Number: None
Name of PD/PI: Hunt, K. (Contact PI), Zuscik, M. (Co-PI)
*Source of Support: Arthritis Foundation
*Primary Place of Performance: University of Colorado Denver
Project/Proposal Start and End Date: (MM/YYYY) (if available): 01/2024 – 01/2026
*Total Award Amount (including Indirect Costs):
*Person Months (Calendar/Academic/Summer) per budget period.

Year (YYYY)	Person Months (##.##)
1. 2024	0.6 calendar
2. 2025	0.6 calendar

*****NO OVERLAP*****

PENDING:

*Title: Inhibiting angiogenesis in growth plate injuries to prevent bony repair tissue formation
*Major Goals: This project aims to investigate the role that angiogenic processes play in the formation of the bony bar, and to develop biomaterial delivery systems that are capable of blocking them. The delivery of microRNA to target various parts of angiogenic pathways will be investigated to determine their effect on blocking bony bar formation in growth plate injuries.
*Status of Support: Pending
Project Number: 1R01AR079512-01A1
Name of PD/PI: Payne, K.A. (Contact PI), Zuscik, M. (Co-I)
*Source of Support: NIAMS
*Primary Place of Performance: University of Colorado Denver
Project/Proposal Start and End Date: (MM/YYYY) (if available): 07/2023 – 06/2028
*Total Award Amount (including Indirect Costs):
*Person Months (Calendar/Academic/Summer) per budget period.

Year (YYYY)	Person Months (##.##)
1. 2024	0.25 calendar
2. 2025	0.25 calendar
3. 2026	0.25 calendar
4. 2027	0.25 calendar
5. 2028	0.25 calendar

*****NO OVERLAP*****

*Title: Microphysiological joint-on-chip platform for the study of arthritic diseases
*Major Goals: Understanding homeostatic and pathologic change in the joint using the joint-on-chip platform described in this application.
*Status of Support: Pending
Project Number: R01
Name of PD/PI: Neu, C. (Contact PI), Zuscik, M. (Co-I)
*Source of Support: NIH
*Primary Place of Performance: University of Colorado Boulder
Project/Proposal Start and End Date: (MM/YYYY) (if available): 7/2024 – 6/2029
*Total Award Amount (including Indirect Costs): (total sub-award)
* Person Months (Calendar/Academic/Summer) per budget period.

Year (YYYY)	Person Months (##.##)
1. 2024	1.0 calendar
2. 2025	1.0 calendar
3. 2026	1.0 calendar
4. 2027	1.0 calendar
5. 2028	1.0 calendar

*****NO OVERLAP*****

*Title: A minimally invasive multimodal biomaterial approach to tissue regeneration in OA
*Major Goals: We propose a transformative concept combining novel engineered orthogonal regenerative therapeutic biomaterials, gene therapy, and an FDA-approved chondro-/osteo-regenerative drug in a multimodal approach to reestablish joint tissues affected by OA.
*Status of Support: Pending
Project Number: N/A, Novel Innovations for Tissue Regeneration in Osteoarthritis (NITRO)
Name of PD/PI: Bryant, S. (Contact PI), Payne, K. (Co-PI), Zuscik, M. (Co-PI)
*Source of Support: Advanced Research Projects Agency for Health (ARPA-H)
*Primary Place of Performance: University of Colorado Boulder
Project/Proposal Start and End Date: (MM/YYYY) (if available): 1/2024 – 12/2028
*Total Award Amount (including Indirect Costs): (total sub-award)
*Person Months (Calendar/Academic/Summer) per budget period.

Year (YYYY)	Person Months (##.##)
1. 2024	3.0 calendar
2. 2025	3.0 calendar
3. 2026	3.0 calendar
4. 2027	3.0 calendar
5. 2028	3.0 calendar

*****NO OVERLAP*****

Gill

*Title: Understand biological factors underlying early childhood caries disparity from the oral microbiome in early infancy
Major Goals: Leveraging an archived underserved birth cohort, our multidisciplinary team proposes using cutting- edge metagenomic sequencing and analysis tool, combined with a high-dimensional statistical machine learning approach, to examine the early-life oral microbiome development and identify its multilevel determinant and association to ECC. ECC risk factors revealed via prediction models could be used as targets for ECC early prediction and prevention specifically suitable for underserved racial minority children.
*Status of Support: ACTIVE
Project Number: R01 DE031025
Name of PD/PI: Gill, S, Xiao, J. and Wu, T. MPIs
*Source of Support: NIDCR
*Primary Place of Performance: University of Rochester, Rochester NY
Project/Proposal Start and End Date: (MM/YYYY) (if available): 5/2022 – 1/2027
*Total Award Amount (including Indirect Costs):
*Person Months (Calendar/Academic/Summer) per budget period.

Year (YYYY)	Person Months (##.##)
1. 2022	1.92 calendar months
2. 2023	1.92 calendar months
3. 2024	1.92 calendar months
4. 2025	1.92 calendar months
5. 2026	1.92 calendar months

*****NO OVERLAP*****

*Title: Povidone Iodine Efficacy Study (PIES)
Major Goals: Severe Early Childhood Caries (S-ECC) is an infectious disease that continues to be a significant global public health problem among young, preschool children. The clinical, social and public health impact of S-ECC is underscored by its association with increased risk of new cavities in the primary dentition, a higher risk of cavities in the permanent dentition, hospitalizations and emergency room visits, high treatment costs, lost school days, diminished ability to learn and a profound impact on a child's quality of life. Results of treatment of S-ECC are poor; approximately 40% of children treated for S-ECC will develop new cavities within 12 months after dental surgery. This proposal will assess the efficacy of topical antibacterial therapy in improving clinical outcomes for S-ECC.
*Status of Support: Awarded
Project Number: 4UH3DE030434
Name of PD/PI: D. Kopycka-Kedzierawski
*Source of Support: NIH
*Primary Place of Performance: University of Rochester
Project/Proposal Start and End Date: (MM/YYYY) (if available): 5/1/22-4/30/27
*Total Award Amount (including Indirect Costs):

Year (YYYY)	Person Months (##.##)
1. 2022	2.04 calendar months
2. 2023	2.04 calendar months
3. 2024	2.04 calendar months
4. 2025	2.04 calendar months
5. 2026	2.04 calendar months

*****NO OVERLAP*****

*Title: Targeting the gut microbiome to treat posttraumatic osteoarthritis
Major Goals: The goal of this project is to study the role of the gut microbiome in the chondroprotective effects of oral dietary supplements containing hydrolyzed type I collagen in posttraumatic osteoarthritis.
*Status of Support: ACTIVE
Project Number: W81XWH-19-1-0808
Name of PD/PI: Gill, S and Zuscik, M. –partnering PIs
*Source of Support: Department of the Army
*Primary Place of Performance: University of Rochester, Rochester NY
Project/Proposal Start and End Date: (MM/YYYY) (if available): 9/2019-9/2023 NCE
*Total Award Amount (including Indirect Costs):
*Person Months (Calendar/Academic/Summer) per budget period.

Year (YYYY)	Person Months (##.##)
1. 2019	3.0 calendar months
2. 2020	3.0 calendar months
3. 2021	0.96 calendar months
4. 2022	0.36 calendar months

THIS AWARD
*Title: Role of the gut Microbiome in the osteoarthritis of obesity
Major Goals: The major goals of this project are to definitively establish that a pro-inflammatory dysbiotic gut microbiome is causal in the osteoarthritis (OA) of obesity, and demonstrate that correction of this dysbiosis using strategies to expand Bifidobacterium pseudolongum will decelerate the progression of OA in the obese context.
*Status of Support: ACTIVE
Project Number: R01 AR078414
Name of PD/PI: Gill, S. and Zuscik, M. MPIs
*Source of Support: NIH/NIAMS
*Primary Place of Performance: University of Rochester, Rochester NY
Project/Proposal Start and End Date: (MM/YYYY) (if available): 4/2021-2/2026
* Total Award Amount (including Indirect Costs):

* Person Months (Calendar/Academic/Summer) per budget period.

Year (YYYY)	Person Months (##.##)
1. 2021	3.0 calendar months
2. 2022	1.8 calendar months
3. 2023	1.8 calendar months
4. 2024	1.8 calendar months
5. 2025	1.8 calendar months

*Title: Biomarker Identification, Viral Susceptibility and Management in S. aureus Colonized AD Patients Major Goals: To determine the impact of the pathogen, Staphylococcus aureus (which is commonly present on the skin of atopic dermatitis patients), on systemic inflammation (measured in the circulation), response to treatments, and viral skin infections in atopic dermatitis patients.
*Status of Support: Active
Project Number: U01 AI152011
Name of PD/PI: Beck, L.
*Source of Support: NIH
*Primary Place of Performance: University of Rochester, Rochester NY
Project/Proposal Start and End Date: (MM/YYYY) (if available): 4/2020-3/2027
*Total Award Amount (including Indirect Costs):
*Person Months (Calendar/Academic/Summer) per budget period.

Year (YYYY)	Person Months (##.##)
1. 2020	0 calendar months
2. 2021	1.8 calendar months
3. 2022	1.8 calendar months
4. 2023	1.8 calendar months
5. 2024	1.2 calendar months
6. 2025	1.2 calendar months
7. 2026	1.2 calendar months

*****NO OVERLAP*****

*Title: Neurobiological and neurocognitive consequences of diverse microbiome functional trajectories
Major Goals: We are testing the central hypothesis that neurodevelopment is dependent on age-driven biosynthesis of NAMs through the postnatal period of infant gut-microbiome (IGM) development. In Aim 1, we use metagenomic analysis of the prenatal maternal vaginal microbiome (MVM) to identify species and functional biosynthetic pathways for NAMs associated with PNA. We also assess the potential transfer of maternal anxiety through the initial colonization of the infant gut microbiome by an anxiety “imprinted” MVM. In Aim 2, we use metagenomic and metabolomic analyses to determine the association between key stages of IGM development and differential synthesis of NAMs over the first year, attending to confounds and competing exposures, most notably, maternal diet and infant feeding. In Aim 3, we apply this rich data to predict neurocognitive assessments from age 1 to 4 years to formally test the temporal relationship between microbiome phase and neurodevelopment in the first year of life and durability of the microbiota-neurodevelopment relationship through 4 years of age.
*Status of Support: Active
Project Number: R01 MH125103
Name of PD/PI: Gill, S./O’Connor, T./Scheible, K. MPI
*Source of Support: NIH
*Primary Place of Performance: University of Rochester, Rochester NY
Project/Proposal Start and End Date: (MM/YYYY) (if available): 7/2022-05/2027
*Total Award Amount (including Indirect Costs):
*Person Months (Calendar/Academic/Summer) per budget period.

Year (YYYY)	Person Months (##.##)
1. 2022	2.28 calendar months

Year (YYYY)	Person Months (##.##)
2. 2023	2.28 calendar months
3. 2024	2.28 calendar months
4. 2025	2.28 calendar months
5. 2026	2.28 calendar months

*****NO OVERLAP*****

*Title: Center of Research Translation on the Osteoimmunology of Bone Infection (CoRTOBI)
Major Goals: Bone infection caused by S. aureus remains the bane of orthopaedic surgery, as diagnostics, prophylaxis and treatments have significant shortcomings that result in catastrophic outcomes for patients, and crippling healthcare costs. To address this, we propose renewal of the Center of Research Translation on the Osteoimmunology of Bone Infection (CoRTOBI), which will increase our knowledge on pathogenesis and immunity, and develop novel diagnostics and interventions for patients with serious bone infections.
*Status of Support: Active
Project Number: P50 AR072000
Name of PD/PI: Schwarz, E.
*Source of Support: NIAMS
*Primary Place of Performance: University of Rochester, Rochester NY
Project/Proposal Start and End Date: (MM/YYYY) (if available): 09/2022 – 08/2027
*Total Award Amount (including Indirect Costs):
*Person Months (Calendar/Academic/Summer) per budget period.

Year (YYYY)	Person Months (##.##)
1. 2022	0 calendar months
2. 2023	0 calendar months
3. 2024	1.2 calendar months
4. 2025	1.8 calendar months
5. 2026	1.2 calendar months

*****NO OVERLAP*****

*Title: Complement C1q and sepsis associated fatalities
Major Goals: This study will determine the underlying mechanisms that lead to the accumulation of neutrophils in the organs that causes fatal hyper-inflammatory responses in septic patients
Aim 1. Determine the relationship between C1q expression in peripheral blood neutrophils and organ failure and death in critically ill septic patients.
Aim 2. Explore the mechanisms by which neutrophil C1q hastens sepsis resolution.
Aim 3. Investigate the mechanisms underlying the heterogeneous C1q expression associated with sepsis mortality
*Status of Support: Active
Project Number: R01 HL160723
Name of PD/PI: Kim, M./Pietropaoli A. MPI
*Source of Support: NIH
*Primary Place of Performance: University of Rochester, Rochester NY
Project/Proposal Start and End Date: (MM/YYYY) (if available): 7/2022-06/2027
*Total Award Amount (including Indirect Costs):
*Person Months (Calendar/Academic/Summer) per budget period.

Year (YYYY)	Person Months (##.##)
1. 2022	0.48 calendar months
2. 2023	0.48 calendar months
3. 2024	0.48 calendar months
4. 2025	0.48 calendar months
5. 2026	0.48 calendar months

*****NO OVERLAP*****

PENDING

*Title: Interactions of polyamines and macrophages on obesity-related type 2 diabetes during implant associated osteomyeltis

Major Goals: In this study, we will examine polyamine-mediated immunomodulatory mechanisms during *S. aureus* implant-associated osteomyelitis in obesity/T2D. We will assess if dysfunctional macrophages that are recruited to the site of S. aureus bone infection accentuate disease severity in obese/T2D mice (AIM 1) and if oral polyamine treatments correct macrophage dysfunction to decrease the disease burden in obese/T2D mice (AIM 2).

*Status of Support: PENDING

Project Number: R21 AI178267

Name of PD/PI: Gill, S. - MPI, Muthukrishnan, G. - MPI

*Source of Support: NIAID

*Primary Place of Performance: University of Rochester, Rochester NY

Project/Proposal Start and End Date: (MM/YYYY) (if available): 7/1/2023-06/30/2025

*Total Award Amount (including Indirect Costs):

*Person Months (Calendar/Academic/Summer) per budget period.

Year (YYYY)	Person Months (##.##)
1. 2024	0.6 calendar months
2. 2025	0.6 calendar months

*****NO OVERLAP*****

PENDING

*Title: Microbiome-Host-RSV Interactions and Illness Severity

Major Goals: This proposal will study the mechanisms by which non-typeable *Haemophilus influenzae* (NTHi) delays interferon responses (IFN) and enhances infant Respiratory Syncytial Virus (RSV) disease severity and the role of defective viral genomes (DVGs) in regulating the NTHi-induced responses. We will use in vitro and ex vivo models to characterize the host molecular and cellular mechanisms, the role of RSV DVGs in mediating the IFN response, and investigate NTHi functions that potentiate severe host responses and effect respiratory host-microbiota community interactions.

*Status of Support: PENDING

Project Number: R01 AI179777

Name of PD/PI: Gill, S./Mariani, T. - MPI

*Source of Support: NIH

*Primary Place of Performance: University of Rochester, Rochester NY

Project/Proposal Start and End Date: (MM/YYYY) (if available): 9/1/2023-08/31/2028

*Total Award Amount (including Indirect Costs):

*Person Months (Calendar/Academic/Summer) per budget period.

Year (YYYY)	Person Months (##.##)
1. 2023	1.8 calendar months
2. 2025	1.8 calendar months
3. 2026	1.8 calendar months
4. 2027	1.8 calendar months
5. 2028	1.8 calendar months

*****NO OVERLAP*****

PENDING

*Title: Metabolic Effects of Differing Carbohydrate Sources in Infant Formula – A Randomized Control Trial

Major Goals: This Randomized Controlled Trial (RCT) will study the impact of different carbohydrate sources in infant formula on infant physiology. Formula-fed infants will be randomized to consume a formula that has a carbohydrate source of either lactose, glucose, or glucose/sucrose. Impact on infant glycemic control, intestinal gene expression, and metabolomic profile will be studied. A group of exclusively breastfed infants will be included as a control group.

*Status of Support: PENDING

Project Number: R01 HD113587
Name of PD/PI: Young, B. (Role: Co-Investigator)
*Source of Support: NIH
*Primary Place of Performance: University of Rochester, Rochester NY
Project/Proposal Start and End Date: (MM/YYYY) (if available): 12/01/2023 – 11/30/2028
*Total Award Amount (including Indirect Costs):
*Person Months (Calendar/Academic/Summer) per budget period.

Year (YYYY)	Person Months (##.##)
1. 2023	0.0 calendar months
2. 2024	0.0 calendar months
3. 2025	0.0 calendar months
4. 2026	0.6 calendar months
5. 2027	0.6 calendar months

*****NO OVERLAP*****

PENDING
*Title: Statistical methods to facilitate the translation of microbiome research into clinical practice
Major Goals: This project aims to develop statistical and computational methods for human microbiome data analysis. The proposed methods are expected to 1) reduce the irreproducibility issue of microbiome studies; and 2) gain more insights into the mediating roles (i.e., being affected by external factors and modulating phenotypes) of the microbiome. These are minimum requirements to determine microbes truly contributing to a specific disease, thus facilitating the translation of microbiome research into therapeutic and preventative applications.
*Status of Support: PENDING
Project Number: R01 DE033388
Name of PD/PI: Sohn, M. (Role: Co-Investigator)
*Source of Support: NIH
*Primary Place of Performance: University of Rochester, Rochester NY
Project/Proposal Start and End Date: (MM/YYYY) (if available): 01/01/2024 – 12/31/2028
*Total Award Amount (including Indirect Costs):
*Person Months (Calendar/Academic/Summer) per budget period.

Year (YYYY)	Person Months (##.##)
1. 2024	1.2 calendar months
2. 2025	1.2 calendar months
3. 2026	1.2 calendar months
4. 2027	1.2 calendar months
5. 2028	1.2 calendar months

*****NO OVERLAP*****

- What other organizations were involved as partners?

a. Organization Name:
Rousselot BVBA

b. Location of Organization:
Gent, Belgium

c. Partner's Contribution to the Project:
Other: Study material, hydrolyzed hyaline cartilage

8. Special Reporting Requirements

- Collaborative Award

This is a collaborative award. Partnering PIs Michael Zuscik PhD and Steven Gill PhD are located at the University of Colorado and University of Rochester, respectively. This report has denoted which aspects of the project have been completed at each site, so both partnering PIs will be submitting this same document.

- Quad Charts

Not applicable

9. Appendix 1: Villani et al, Manuscript Draft

POST-TRAUMATIC OSTEOARTHRITIS DOES NOT STRONGLY IMPACT GUT MICROBIOME COMMUNITY COMPOSITION BUT SIGNIFICANTLY ALTERS THE FUNCTIONAL OUTPUT OF RESIDENT TAXA – results from a murine study

Introduction

Osteoarthritis(OA), the leading cause of disability in the United States (US), is a degenerative disease that involves the loss and destruction of cartilage within diarthrodial joints (Chen et al., 2017). OA afflicts more than 25% of the population over 18 years, with the incidence of OA increasing by more than 100% between 1990 and 2017 (Chen et al., 2017; Jin et al., 2020). Numerous risk factors contribute to OA development, most prominently obesity, genetics, age, sex, and injury (Martel-Pelletier et al., 2016). Injury dramatically increases the likelihood of OA onset, with 35% of patients developing symptomatic knee OA within 10 years of sustaining an injury, commonly referred to as pos-traumatic OA (PTOA) (Lie et al., 2019). The alarming fact that all currently existing OA therapeutic options remain palliative, makes understanding the OA etiopathogenesis of critical relevance.

Gut microbiota refers to the ecosystem of bacteria, fungi, viruses, phages, parasites, and archaea that inhabit digestive tract (Tasnim et al., 2017). Gut microbiota has a recognized role in host wellbeing, and alterations in both its composition and function affect not only the colon but also peripheral organs (Clarke et al., 2014). Previous studies demonstrate that altering the gut microbiota with either a prebiotic or a probiotic can prevent the development of OA (Favazzo et al., 2020; I et al., 2022; Schott et al., 2018). When compared to specific pathogen-free mice, both germ-free and antibiotic-treated mice showed protection against the development of OA (Guan et al., 2020; Ulici et al., 2018). Findings from human studies also suggest that gut flora may contribute to the development of OA. Thus, *Streptococcus* abundance correlates with the severity of knee pain in OA (Boer et al., 2019). Lipopolysaccharide (LPS) levels are elevated within both the synovial tissue and serum of people with OA (Huang et al., 2016). Metabolomics on fecal samples from subjects who are obese, with or without OA, indicated that propionic acid, indoles, and other tryptophan metabolites were altered in OA patients (Rushing et al., 2022). Notably, metabolites involved in the OA of

obesity markedly differ from those involved in PTOA (Ejtahed et al., 2020; Liu et al., 2017), provoking an idea of the instrumental role of gut microbiota functional capacity in OA development.

We and others demonstrated that targeting the microbiome is protective against OA development (Rios et al., 2019; Schott et al., 2018). However, its role in PTOA remains insufficiently understood. Human gut microbiome heterogeneity limits the possibilities of modifying the abundances of specific taxa in the context of clinical disease, making a controlled animal study a pivotal approach. Therefore, in order to identify the gut microbiota fingerprints in post-traumatic OA, we applied a multi-omics approach in a murine model of PTOA. Following 16S rRNA gene sequencing, we performed metatranscriptomics and metagenomics to determine what genes and microbial taxa contribute to the PTOA. In order to provide a functional readout of the microbiome, we then conducted a pathway analysis of both cecal and fecal contents, followed by metabolomics analysis in fecal samples. Next, we performed RNA-Seq on the colon to determine how the functional alterations affected the host tissue that directly communicates with the microbiome. Results from this study suggest that despite minor compositional changes within the gut of mice with PTOA, the function of the gut microbiome is altered during PTOA. Neither fecal nor caecal microbiome composition was altered in PTOA, which was confirmed upon metagenome sequencing in caecum. Functional readouts indicated that the aspartate-derived amino acid pathway and Bifidobacterium shunt were diminished in the tissues of injured animals. Modified microbiota activity in the injured animals was further confirmed by the metatranscriptomics analysis in caecum. Furthermore, the fecal metabolomics analysis confirmed the downregulation of short-chain fatty acid synthesis and polyamines in injured animals, potentially indicative of lower adaptive response to inflammatory stress. Lipid metabolism was significantly downregulated in caecal samples from injured animals, specifically phosphatidylcholines, sphingomyelin, and middle-chain fatty acids. Interestingly, uric and citric acid were upregulated in the serum of injured animals, indicating enhanced catabolic activity and oxidative metabolism in the condition of imposed stress. Taken together, our study provided high-dimensional data supportive of

extensive metabolic reprogramming and functional microbiota response in the condition of PTOA.

Results

Reproducibility and morphometry of the PTOA murine model

Destabilization of the medial meniscus was utilized to model the pathological OA process. A bilateral surgery was performed to induce OA in both knees (Fig 1A). Control animals remained unmanipulated and had significantly more cartilage present on both the femur and tibia (Fig 1B-C). Injured animals had a significant decrease in total cartilage on both the femur and tibia compared to healthy controls (Fig 1D). The total chondrocytes and Safranin O+ matrix-producing chondrocytes were reduced in mice with PTOA (Fig 1E-H). Osteoarthritis Research Society International (OARSI) scores were significantly different between injured and uninjured animals, confirming the presence of OA within injured joints (Fig 1I).

Micro-CT analysis expectedly revealed a significant increase in medial meniscus volume within injured animals compared to uninjured controls (Fig 1J). Representative images of the joint show increased ectopic mineralization around the meniscus of injured animals. These results, combined with histomorphometric data, validate that injured mice have a severe and reproducible OA phenotype.

16s sequencing reveals PTOA does not significantly alter the fecal microbiome

To determine if PTOA induces shifts in the gut microbiome, we collected fecal pellets biweekly from injured animals and uninjured controls and performed 16S rRNA sequencing. Principle coordinate analysis (PCoA) of microbial community dissimilarity utilizing the Bray-Curtis index of all fecal samples collected throughout the study reveals that the microbiome of animals with PTOA remains similar to control animals (Fig 2A). Nonmetric multidimensional scaling (NMDS) analysis over the course of the study indicates that only one distinct microbial profile is present between both groups, signifying joint injury and PTOA progression did not lead to discernable changes in the composition of the gut microbiome in our cohort of animals (Fig 2B). At the phylum level, microbial communities did not differ dramatically over the course of 24 weeks, as evidenced by nearly identical bar charts (Fig 2C). This was also true at the family level, as bar plots again did not show any discernible differences (Fig 2D).

To further characterize the fecal gut microbiome, a PCoA plot of fecal samples collected at the time of harvest was generated (Fig 3A). At both the phylum and genus levels the fecal microbiome at the time of harvest did not differ between the animals with PTOA and control animals (Fig 3 B and C). This was further evidenced by the lack of statistically significant differences in any of the members of the microbiome in the 24-week fecal samples (Fig 3D). These results indicate that the composition of the fecal microbiome shows little change due to the presence of OA in our cohort of animals.

16S sequencing reveals that PTOA does not drastically alter the composition of the cecal microbiome

Cecal and fecal contents differ in taxonomic structure (REF); thus, we performed 16S rRNA characterization of the cecal contents of animals with end-stage PTOA. The microbial composition of the cecal contents changed slightly, but the general organization of the microbiome remained largely similar between injured and uninjured animals, as demonstrated by the overlap in the PCoA plot (Fig 4A). The Firmicutes to Bacteroides ratio (F/B), a ratio that has been shown to increase in inflammatory states (REF), was increased in the injured cohort, mirroring published data (Kelsey H. Collins et al., 2021). Firmicutes accounted for 79% of the cecal microbiome composition in injured animals, with that number decreasing to 69% in uninjured animals. Bacteroides made up 15% of the ceca, compared to 26% in uninjured animals (Fig 4B-C). No significant alterations in the level of microbial species were present within the ceca (Fig 4D). In injured animals, *Bifidobacterium pseudolongum* and family *Bacillaceae* were reduced, whereas the family *Lachnospiraceae* and genera *Anaeroplasma* increased in the caecal microbiome (Fig 2.4 C and D). *Bifidobacterium pseudolongum* exerts favorable health outcomes, including protection in the OA of obesity (Moya-Pérez et al., 2015; Schott et al., 2018).

Caecal metagenomics identifies microbial taxa altered in the PTOA

Shotgun sequencing revealed four microbial species significantly altered between injured mice and matched controls, three of which were not present in our 16S rRNA sequencing. *Asaccharobacter celatus, Adlercreutzia equolifaciens*, *Clostridium*

sp. ASF502, and *Bifidobacterium pseudolongum* were altered in the ceca of animals with PTOA (Fig 5A-B). Interestingly, *Adlercreutzia equolifaciens* has previously been implicated in other musculoskeletal diseases but has not been studied in the context of OA (Dekker Nitert et al., 2020). Validating our 16S rRNA findings, the F/B ratio was increased in injured animals, a phenotype largely driven by the increase of *Clostridium sp. ASF502 (*Fig 5A-B*).* The PCoA plot reiterated that although these novel species are altered in PTOA, the general structure of the community did not change significantly (Fig 5C). Mirroring previous human findings, these data indicate that the microbiome of animals with and without PTOA does not display significant compositional changes.

The functional capacity of the cecum is altered in the colon of animals with PTOA.

We performed in silico bacterial pathway profiling utilizing HUMAnN 3 (Beghini et al., 2021). DNA metagenomic analysis revealed 110 pathways that were differentially abundant between uninjured and PTOA animals. Of these pathways, 71 were associated with biosynthesis, 21 with degradation, utilization, or assimilation, 14 with the generation of precursor metabolites and energy, 2 with super pathways, and 1 with macromolecule modification (Fig 6A, Table 1). The *Bifidobacterium* shunt pathway, a key indicator of *Bifidobacterium* activity was overly abundant in uninjured animals (Fig 6B). The result of this pathway is the production of ATP, acetate, and lactate. This reaction is symbiotic in nature, as *Bifidobacterium* gains ATP while the host gains acetate, which can be used for host ATP production, and lactate, an antimicrobial metabolite that can hamper the growth of pathogenic microbes.

Of note, the pathway for 2-oxobutanoate degradation II was overrepresented in the microbiome of uninjured mice compared to animals with PTOA (Fig 6C). This pathway is associated with the production of propionate, a SCFA with anti-inflammatory effects on the colon and other distal tissues (A. Filippone et al., 2020; Tedelind et al., 2007). Six methionine synthesis pathways were more abundant in uninjured animals, L-methionine can be broken down into 2-oxobutanoate (Fig 6D-E, Table 1). To further understand our metagenomic dataset, we utilized SqueezeMeta to determine molecular functions via KeggOntology (Tamames & Puente-Sánchez, 2019). In total, 111 orthologs were identified, with 42 of these mapping to metabolic pathways and 17

mapping to the biosynthesis of secondary metabolites (Table 2). These data indicate that although the composition of the gut microbiome of animals with PTOA does not show large-scale compositional alterations, the functional capacity of the gut microbiome has shifted.

Metatranscriptomic analysis reveals altered metabolism pathways in the gut microbiome of animals with PTOA.

Metatranscriptomics on the cecal contents provided insight into active pathways within the cecal microbiota. SqueezeMeta uncovered a total of 8 KEGG orthology groups that were differentially expressed between uninjured controls and injured animals, 5 of which were downregulated in the injured animals and 3 of which were activated in the injured animals. Of the 5 orthologs downregulated in OA, 2 were involved in environmental information and processing (Fig 7A-C). Interestingly, all 3 of the ortholog groups upregulated in the cecal microbiome during PTOA were associated with metabolism (Fig 7B-C). In addition to Kegg orthology groups, 125 significant Clusters of Ortholog Groups (COGs) and 30 Protein Families (PFAMs) were identified, with the top 30 of each indicated in (Table 3-4). One of the most upregulated PFAMs was the Membrane Attack Complex/Perforin domain (MACPF) (coefficient=4.792) (Fig 7D). The MACPF is an important component of microbial virulence. In fact, certain microbial species can also utilize this domain as a competitive advantage by releasing MACPF in vesicles, which can act on competing commensals of the gut (Chatzidaki-Livanis et al., 2014). The GLUG motif was elevated in the ceca of animals with PTOA (coefficient =2.81) (Fig 7E). The GLUG motif is a bacterial immunoglobulin protease that can cleave IgA proteins produced by the host immune system. This bacterial defense system is another example of how pathogenic bacteria in the microbiome of animals with PTOA could avoid host surveillance. These findings show that the cecal microbiome of PTOA animals is functionally altered, with increases in ortholog groups associated with bacterial metabolism and bacterial competition altered in the cecum of animals with PTOA.

PTOA alters metabolites produced by the gut microbiome

We performed targeted metabolomics in fecal and cecal samples, revealing large-scale changes (Fig 8-9). In total, 8 metabolites were altered in the cecum and 18 were differentially produced in the feces of animals with PTOA. PCoA plot demonstrates the shift in the metabolites in the fecal (Fig 8A) and cecal (Fig 9A). Volcano plots display significantly altered metabolites in the fecal (Fig 8B) and cecal (Fig 9B) samples. Butyric acid, a SCFA protective properties in pre-clinical models of PTOA, was reduced in the fecal pellets of animals with PTOA (Fig 8C) (Cho et al., 2022; Zhou et al., 2021). Butyrate supplementation in PTOA is protective through direct action on both chondrocytes and cells of the synovium (Han et al., 2020; Pirozzi et al., 2018). Hitherto studies did not explain how the loss of butyrate affects PTOA progression; however, based on our findings, loss of butyrate could play a role in the OA disease process. The propionic acid levels were also lower in the feces of animals with PTOA (Fig 8D).

The cartilage breakdown products trans-hydroxyproline and proline were reduced in fecal samples from PTOA animals (Fig 8E-F). Trans-hydroxy proline has anti-inflammatory effects on the colon and has mainly been studied as a biomarker in OA (Ahmed et al., 2015; Ji et al., 2018). Trans-hydroxyproline may also play a role in the shaping of the bacteria present in the gut, favoring microbes with the capability to utilize trans-hydroxyproline (Huang et al., 2018).

Polyamines spermidine and spermine were decreased in the fecal pellets of injured animals (Fig 8G-H). Polyamines have recently been implicated as playing a role in other musculoskeletal diseases, with evidence indicating that these metabolites can interact with both cells of the joint and immune system cells in the colon.

Our data strongly suggest that the functional output of the gut microbiome differs between animals with PTOA compared to healthy controls.

Citric acid and uric acid are altered in the serum of animals with PTOA.

Serum was harvested from the mice at the time of euthanasia for targeted metabolomics. Only two metabolites differed in the serum of animals with PTOA. Citric acid and uric acid were both elevated in the serum of injured animals (Fig 2.10). Human studies show that uric acid increases in the serum of OA patients (Ma & Leung, 2017).

Bacteria in the gut microbiome can both breakdown and release uric acid (Tong et al., 2022), future studies in OA should determine this mechanism.

The colon transcriptome is altered in animals with PTOA.

Surprisingly, targeted metabolomics revealed no changes in SCFAs, polyamines, cartilage breakdown products, and fatty acids identified in the serum. Thus, to determine if these metabolites have a biological effect on the tissue they most closely interact with, we performed RNA-Seq on the colon of animals with and without PTOA. Transcriptome analysis of the murine colon tissue demonstrated significant changes in the colon gene profile in injured animals (Fig 11 A). Principle component analysis (PCA) based on quantification of gene signature dissimilarity indicated that the colons of animals with PTOA differed from healthy control animals (Fig 11 B). In order to further understand the differences in gene expression, we performed cell type enrichment utilizing cTen, which utilizes an enrichment algorithm that identifies cell type demographics based on differentially expressed genes (DEG) (Shoemaker et al., 2012). Cell type enrichment of the upregulated DEG from injured animals revealed an enrichment of genes associated with the macrophage lineage, suggesting increased macrophage activity in the colon of animals with PTOA (Fig 11C). Macrophages in the colon produce inflammatory cytokines that can disrupt intestinal integrity; however, they have not been studied in the context of PTOA (Kawano et al., 2016).

We utilized Enrichr, a tool that contains a variety of gene libraries capable of identifying gene ontology, to perform enrichment analysis. In the top 25 enriched ontologies, 11 of these terms were associated with lipid and fat signaling (Fig 11D). The effects of decreased lipid signaling in the colon have scarcely been studied.

Two distinct gene ontologies associated with phagocytosis were reduced in the top 25 ontologies, indicating that macrophage function may have been altered in PTOA mice (Table 5) Together with cTen cell type enrichment, these data indicate that although macrophage activity is increased in the colon, the phagocytic function of these macrophages maybe altered.

To identify pathways that are involved in the onset of PTOA in the colon, we performed KEGG analysis utilizing Enrichr with the DEGs. Two pathways were

identified as significantly altered: terpenoid backbone biosynthesis and fat digestion and absorption. Like signatures identified in gene ontology, fat digestion, and absorption pathways are altered in animals with PTOA, indicating the alteration of metabolic pathways in the colon may be involved in the onset of PTOA.

DISCUSSION

In the controlled study in a murine model, we found that PTOA induces minimal changes in the composition of the gut microbiome, but results in large functional changes evidenced by metatranscriptomic and metabolomic shifts. Similarly, evidence from human studies shows negligible change in the gut microbiome composition in patients with PTOA (Boer et al., 2019). On the mechanistic level, pathways associated with SCFA production and bacterial competition emerge as important factors in PTOA progression potentially altering colon transcriptome.

Boer et al. demonstrated that Streptococcus was associated with knee joint pain in the Rotterdam and Lifeline-DEEP cohorts, but, similar to our findings in mice, they found no significant variation in microbial composition when evaluating OA development (Boer et al., 2019). Loeser et al. also performed 16S rRNA compositional analyses on patients with and without OA who had a BMI greater than 30, finding no significant compositional differences between the two groups (Loeser et al., 2022). Metabolomics on the serum and fecal contents of obese OA patients revealed changes in LPS, osteopontin, propanoic acid, indoles, and other tryptophan metabolites (Loeser et al., 2022; Rushing et al., 2022). Obesity, however, has substantial effects on the microbiota and its metabolites, making the effect of OA harder to examine due to the obesity overlay (Canfora et al., 2019). Furthermore, Collins et al demonstrated a shift in the B/F ratio during OA progression and identified 9 taxa correlated with cartilage loss, irrespective of diet status or fat composition (Kelsey H. Collins et al., 2021). In our study, the F/B ratio increased in animals with PTOA. An increase in the F/B ratio has been linked to an increase in inflammation and a decline in overall health (Favazzo et al., 2020; Ley et al., 2005). This conclusion is consistent with clinical studies in OA, indicating the increased F/B ratio throughout OA development and progression (Chisari et al., 2021).

We performed 16S rRNA sequencing longitudinally over the course of the study to uncover compositional shifts in the microbiome that develop during PTOA progression. Surprisingly, the microbiomes of PTOA-affected animals remained comparable to those of control animals, with very minor species differences found over the length of the study. To examine the composition of the microbiome in animals with

end-stage PTOA, cecal contents were extracted and 16S rRNA analysis was performed, again indicating no significant changes.

Bifidobacterium pseudolongum was altered in the cecum if injured animals, and functional readouts delineated its diminished activity. Although utilized as a probiotic, its mechanism of action remains unknown. The bacteria have previously been linked to general health (Arboleya et al., 2016) and the treatment of obesity-related OA (Schott et al., 2018). Previous research has shown favorable effects in the colon, with *B. pseudolongum* outcompeting mucin-degrading bacteria and, as a result, boosting mucus thickness (Mangin et al., 2018). Furthermore, Bifidobacterium reduces inflammation in the colon while enhancing barrier function by upregulating tight junctions and inhibiting the NF-kB pathway (Guo et al., 2022). The expansion of *Bifidobacterium pseudolongum* in the gut microbiome may also explain the increases in both SCFAs and polyamines that were observed via metabolomics, since previous data indicate that *Bifidobacterium pseudolongum* can increase butyric acid, propanoic acid, spermine and spermidine (Guo et al., 2022; LeBlanc et al., 2017; Sugiyama et al., 2018). Using *Bifidobacterium pseudolongum* as a PTOA therapy remains an attractive proposition.

To further understand the gut microbiome's role in PTOA, we performed shotgun metagenomic and metatranscriptomic analyses. Shotgun metagenomic analysis revealed altered abundance of pathways and orthologs in the cecal contents of animals with PTOA compared to controls. Bifidobacterium shunt was a pathway that decreased in abundance in the injured cohort, centered around the enzyme fructose-6-phosphate phosphoketolase, which involves the breakdown of hexose sugars such as glucose and fructose, with the metabolites from this pathway being used to produce SCFAs. On the other hand, SCFAs are produced in the microbiome via bacterial fermentation of dietary fibers and starches. Dietary fibers are typically broken down in the distal colon, where SCFAs can serve as an energy source for colonocytes while also influencing immune cells (Silva et al., 2020). SCFAs play several roles in the colon, including intestinal barrier integrity, mucus production, and inflammation reduction (Parada Venegas et al., 2019; Willemsen et al., 2003). The anti-inflammatory nature of SCFAs makes them an appealing candidates for studies in PTOA. In line with that, the metagenomic pathway analysis of the ceca, indicated upregulation of SCFA pathways abundance, while the

oxobutanoate degradation II pathway decreased animals with PTOA (Fig 2.6). Oxobutanoate degradation results in the formation of propionate, a SCFA with numerous anti-inflammatory properties (Alessia Filippone et al., 2020; Tedelind et al., 2007). Propionic acid was likewise one of the most drastically reduced SCFAs in the feces of mice with PTOA. The effects of propionate in PTOA have not been investigated, propionate has protective effects in collagen-induced rheumatoid arthritis models via a reduction in inflammation. Namely, supplementation of propionate in drinking water or by injection, reduced antigen-induced arthritis, targeting synoviocytes, a key cell type involved in the OA process (Friščić et al., 2021; Ma et al., 2022). In addition to cells of the joint, propionate affects macrophage populations and cells of the colon by reducing the expression of pro-inflammatory cytokines and limiting the activation of the NF-kB pathway, a key pathway that has been implicated in OA development (Liu et al., 2012; R. Yang et al., 2020). With no studies performed in the context of OA, propionic acid emerges as an enticing target for future microbially derived DMOADs.

Butyric acid was another metabolite in our study found elevated in the fecal contents of mice with PTOA. Butyric acid has anti-inflammatory effects in a variety of tissues (Canani et al., 2011), and serves as one of the primary energy sources for colonocytes impacting immune cell development (Parada Venegas et al., 2019). Butyric acid has been shown to decrease autophagy and mediate inflammatory chondrocyte death in murine models of OA, making it a target for therapeutic development (Cho et al., 2022). Furthermore, cell culture experiments utilizing human chondrocytes revealed butyrate has both chondrogenic and anti-inflammatory effects on chondrocytes, demonstrated by a decrease in pro-inflammatory cytokines and type 2 collagen degradation (Zhou et al., 2021). These findings are consistent with our discovery that butyrate levels are lowered in injured animals.

Metabolomics also revealed a decrease in hydroxyproline in the fecal contents of injured animals (Fig 2.8). Hydroxyproline is one of the most abundant amino acids found in collagen, derived via posttranslational hydroxylation of proline. In OA, hydroxyproline has been implicated as a potential biomarker, with arthritic patients demonstrating an increase in serum hydroxyproline (Ahmed et al., 2015). Hydroxyproline may have

protective effects on the colon, as seen in colitis studies via the targeting of the NF-kB pathway (Ji et al., 2018). These anti-inflammatory capabilities of hydroxyproline were also evident in co-culture experiments with macrophages (Ji et al., 2018). Further on, polyamines, spermine and spermidine, were lower in the feces of animals with PTOA. Spermidine can decrease pro-inflammatory cytokines and act directly on both chondrocytes and synoviocytes in the joint (Chen et al., 2020; Sacitharan et al., 2018). In collagen-induced models of rheumatoid arthritis, spermidine inhibits macrophage activation and ultimately reduces disease progression (Yuan et al., 2021). Both spermine and spermidine are also important in the activation of T and B cells in the colon (Hesterberg et al., 2018). The significant decrease in proline and glutamic acid in the feces of uninjured animals may explain the decrease in spermine and spermidine in the feces of PTOA animals. Although non-significantly, acetyl-ornithine was also decreased in the feces of animals with PTOA. Since acetyl-ornithine is a microbially derived product involved in the formation of polyamines, this decrease could provide an explanation for the loss of spermine and spermidine in the microbiome of mice with PTOA.

Our metatranscriptomic study of the microbiome revealed three KEGG pathways that were enriched in PTOA mice. All three processes are involved in metabolism. K18687 is a HIP-CoA ligase is involved in steroid degeneration and a cholesterol degeneration pathway active in the microbiome. The elevation of this pathway in the microbiome of injured mice could be one plausible explanation for the decrease in cholesterol signaling seen in the colon of the PTOA cohort, as the degeneration of cholesterol may be limiting the availability of cholesterol in the colon. Meta-transcriptomic analysis of the microbiome provides definitive evidence that the gut microbiome is functionally, and not compositionally, altered during PTOA.

Serum metabolomics did not reveal an increase in microbially derived metabolites. To this end, we performed RNA-Seq on the colon of animals with PTOA to gain a deeper understanding of how PTOA alone impacts the tissue that most closely interacts with the gut microbiome. Cell type enrichment analysis uncovered a macrophage signature in the colon. We previously demonstrated that a macrophage enrichment in the colon is a driver of inflammation in the OA of obesity (Schott et al.,

2018). Recently, Cho et al. demonstrated that animals with OA have an increase in MCP-1 production within the intestinal epithelium, one of the key recruiters of monocytes and macrophages to sites of inflammation (Cho et al., 2022). In OA, both prebiotic and probiotic treatment restored inflammatory gene networks and MCP1 expression in the colon (Cho et al., 2022) (Schott et al., unpublished data). Depletion of infiltrating macrophages into the colon has been shown in different disease systems to reduce inflammation and improve overall health (Kawano et al., 2016; Rohm et al., 2022). Of the top 25 enriched ontologies identified by Enrichr, two are associated with phagocytosis. These ontologies were reduced in PTOA animals. With an enrichment of macrophages but a decrease in genes associated with phagocytosis, further investigations into both the presence and function of infiltrating macrophages in the colon could not only provide valuable information on the PTOA disease process but also potential therapeutic options.

Surprisingly, seven of the top ten gene ontologies found in the colons of PTOA mice involved a decrease in metabolic processes involving lipid and fat signaling, prominently lipid biosynthetic process. This, combined with the other enriched ontologies in the top ten, such as fatty acid metabolism and steroid metabolism, implies that the colon of animals with PTOA undergoes fundamental metabolic changes. With fatty acids and lipid molecules decreasing in the ceca and feces of PTOA-affected animals, these metabolites may explain the decrease in lipid signaling within the colon. Stearic acid has been shown to have anti-inflammatory effects on the colon (Mitchel et al., 2021); decreases in steric acid and other lipid molecules in the ceca could offer explanations for the altered fatty acid and lipid signaling within the colon of animals with PTOA.

Cholesterol biosynthetic pathway was the third most significant Gene Ontology, with three cholesterol-related ontologies decreasing among the top 25 enriched ontologies in the colons of mice with PTOA. Previous work in OA, particularly the OA of obesity, has targeted elevated cholesterol as a treatment; however, this has resulted in conflicting results (Farnaghi et al., 2017; Papathanasiou et al., 2021; van Gemert et al., 2021). The liver is considered the central location for cholesterol maintenance in the body, but recent work has implicated the colon as a potential source of cholesterol (Kruit

et al., 2006). This was further validated by the increase of metatranscriptomic pathways associated with cholesterol degeneration within the microbiome of animals with PTOA. Further investigations need to be conducted to determine if pathways associated with cholesterol signaling in the colon play a role in PTOA development.

Strengths and Limitations. Our study provides a comprehensive set of high-dimensional multiomics data, establishing for the first time mechanistic basis of the gut microbiota-PTOA axis. It should be noted that in our studies of PTOA, only five animals were sampled per group. Follow-up experiments will be needed that utilize a larger n which may provide more power to identify smaller compositional changes.

Conclusion

This study provides the first metatranscriptomic analysis of the gut microbiome in the context of PTOA. We validated results found in human clinical studies, which showed that PTOA alone does not cause significant changes in the composition of the gut microbiome. We demonstrate via metatranscriptomics, metagenomics, and metabolomics of the cecal and fecal compartments that, despite the small shift in the composition of microbes in the gut, the functional capacity and output are altered due to PTOA. The identification of multiple SCFAs provides insights into future therapies that can be tested in human populations with limited safety concerns. Finally, we performed RNA-Seq on the colon of animals with PTOA to determine metabolic pathways that are altered in PTOA development and may provide key insight into the understanding of the effect of gut microbiota on PTOA development.

MATERIALS AND METHODS

Animal handling and study approval

C57BL/6J mice were purchased from the Jackson Laboratory and housed in groups of 3–5 mice per cage. Mice were housed in microisolator cages with a 12-hour light/dark schedule. Mice were allowed to age, and at 18 weeks of age, they were administered bilateral destabilization of the medical meniscus surgery (DMM). Briefly, mice were anesthetized with inhaled isoflurane, and their knees were shaved. Prior to surgery, mice were given buprenorphine SR at a dose of 1 mg/kg. Under a dissecting microscope, a #10 blade was used to make an initial cut of 5 mm on the medial side to expose the knee joint. Next, using micro-scissors and a #25 syringe, a cut was made on the medial side of the patella tendon to expose the medial meniscus. With a number 11 blade, the medial meniscotibial ligament was transected. Following surgery, incisions were closed with 5-0 silk sutures. Sutures were removed after 10 days. All mouse work was approved by the University of Colorado Anschutz under protocol #904.

Knee joint harvest for histology

Mice were sacrificed 24 weeks after DMM surgery to ensure advanced OA progression. Organs were harvested using American Veterinary Medical Association-approved methods. Both knee joints were removed, and excess muscle tissue was cut away. Joints were placed in cassettes, secured to plastic brackets at 30-degree joint flexion, and fixed in 10% neutral buffered formalin (NBF) for 3-5 days. Knee joints were then washed in PBS and decalcified in Webb-Jee EDTA for 14 days. The joints were processed utilizing a microwave processor and embedded in paraffin as previously described (REF). Tissue blocks were sectioned in the midsagittal plane, with serial sections taken from the joint. Knee tissues were stained with Safranin O/Fast Green, and cartilage was quantified by a blinded observer using Zeiss software.

Histomorphometric analysis of cartilage

Cartilage area, hypertrophic chondrocytes, and safranin O+ chondrocytes were quantified using Zeiss Zen Blue software by a blinded observer. A touch screen and

stylus pen were used to outline the cartilage area in six sections of each animal's joint. Two sections at each level (50 uM apart) were averaged. To count chondrocytes, the stylus pen was used to mark and count over 3 levels and 6 sections.

Micro CT of the knee joint

Prior to decalcification, knee joints were taken from NBF and scanned in PBS using X-ray microcomputed tomography (μCT50, Scanco Medical AG, Bassersdorf, Switzerland). Joints were imaged at 70 kV (200 μA) within a 35 mm diameter field of view, employing 2000 cone beam projections per revolution, and an integration time of 500 msec. Reconstruction of three-dimensional images occurred at 17.2 μm resolution using standard convolution back projection algorithms with Shepp and Logan filtering. Images were rendered at a discrete voxel density of 196,524 voxels/mm3 (isometric 17.2 μm voxels). Images were transposed to longitudinal views, and by manual contouring, menisci were separated from the joint. Mineral density threshold of 550 mg HA/cm^3 was utilized. The mineral was calibrated to a discrete-step hydroxyapatite phantom and segmented from unmineralized meniscal cartilage in conjunction with a constrained Gaussian filter to reduce noise.

OARSI scoring

To quantify OA progression and cartilage degeneration, a semiquantitative histopathologic grading system established by OARSI was employed. Safranin O/fast green-stained sections were graded according to the scale previously described [7]. Scoring was performed by four blinded observers (DAV, MJZ, SLP and MD)

Statistics

Non-omics data were analyzed and plotted with GraphPad Prism (Version 9.4.1). Standard t-tests were used to test significance, with p values < 0.05 considered significant.

METATRANSCRIPTOMICS

Colon preparation for RNA-Seq

At the time of harvest, murine colon tissue was removed. Fecal pellets and mucous were removed from the colon with 5 mL of PBS and a blunt needle. The tissue was then transected with ball scissors, cut in half longitudinally with a razor blade, and flash-frozen in liquid nitrogen. The tissue was then placed at -80 °C for long-term storage.

RNA isolation from the colon

Flash-frozen tissue was submerged in Trizol before being placed in a lysing matrix A tube (MP Biomedicals) and homogenized using Bead Ruptor 12 (Omni International). The tissue was homogenized at a speed of 5 m/s for 15 seconds and placed on ice for 5 minutes; this step was then repeated. Phenol chloroform was added to the homogenized tissue. Tubes were mechanically shaken and then centrifuged at 12000 rcf for 15 minutes at 4 C. The aqueous phase was then extracted and combined with pure ethanol at a ratio of 1:1. RNA was purified from the ethanol: phenol chloroform solution via the Genejet RNA purification kit (Thermo Fisher) following the manufacturer's instructions.

RNA-Seq library construction, sequencing, and data analysis

Novogene was contracted to perform RNA-seq. Messenger RNA was purified using poly-T oligo attached magnetic beads. Following fragmentation, random hexamer primers were used to synthesize the first strand of cDNA. The second strand cDNA synthesis occurred using either dUTP for directional library or dTTP for non-directional library. A bioanalyzer and real time PCR were used for quantification and size distribution detection. Libraries were pooled and sequenced on an illumina platform. Raw reads in the fastq format were processed through novogenes in house Perl scripts. Low quality and reads containing adapters were removed. All downstream analysis only used the clean data. Paired-end clean reads were aligned to the reference genome using HIsat2 v2.05. To generate read counts mapped to each gene, featureCounts v1.5.0-p3 was utilized. The FPKM of each gene was calculated based on the length of the gene and read count mapped to the gene. To determine differential expression

DESeq2 R package (1.20.0) was used. The resulting p-values were adjusted using the Benjamini and Hochberg's approach for controlling false discovery rate. An adjusted p-value <=0.05 was considered differentially expressed. Gene ontology enrichment analysis was implemented by clusterProfiler R package. GO terms with an adjusted pvalue <= 0.05 were considered significantly enriched by differentially expressed genes. KEGG pathways were analyzed using clusterProfiler R package.

METAGENOMICS

Fecal collection:

Fecal pellets were freshly collected from scruffed animals weekly and flash-frozen in cryovials. Vials were then transferred for long-term storage at - 80 °C.

DNA and RNA extractions from fecal and cecal samples

RNA and DNA were extracted using ZymoBIOMICSTM DNA/RNA Miniprep Kit (Zymo Research) with mechanical lysis performed with a FastPrep mechanical lysis (MPBiomedicals).

16S rRNA sequencing

Phusion High-Fidelity DNA polymerase (New England Biolabs) was used to amplify the 16S ribosomal RNA, with primers specific to the V3-V4 hypervariable regions (338F: TCGTCGGCAGCGTCAGATGTGTATAAGAGACAGACTCCTACGGGAGGCAGCAG and 806R: GTCTCGTGGGCTCGGAGATGTGTATAAGAGACAGGGACTACHVGGGTWTCTAAT) followed by dual-indexed adapters P5: AATGATACGGCGACCACCGAGATCTACACxxxxxxxxTCGTCGGCAGCGTC and P7: CAAGCAGAAGACGGCATACGAGATxxxxxxxxGTCTCGTGGGCTCGG, similar to the method of Holm, et al. (Holm et al., 2019). Pooled and Paired-end amplicons were sequenced on an Illumina MiSeq (Illumina)at the University of Rochester Genomics Research Center. Sequencing runs include a positive control (a mock community of

equal parts *Staphylococcus aureus, Lactococcus lactis, Porphyromonas gingivalis, Streptococcus mutans, and Escherichia coli* DNA) and two negative controls consisting of sterile water (amplification control) or buffer only (extraction control). Sterile reagents were used throughout the course of experimentation, with all plastics UV irradiated to eliminate possible DNA background contamination. Bcl2fastq version 2.19.1 was used to demultiplex the raw reads. DADA2 was utilized for cleaning, joining and denoising.

DNA Library Preparation and Sequencing

Fragment profiles of the extracted genomic DNA (gDNA) was assessed on a TapeStation using a gDNA screen tape. Genomic DNA quantity was measured using a Qubit. Libraries were made using the Illumina Nextera XT kit (Illumina, Inc; Cat #FC-131-1096) with 1 ng of gDNA as input. Fragment size profiles and quantification of the libraries were measured using the Fragment Analyzer and Qubit, respectively. The libraries were normalized to 1.75nM, pooled at equimolar concentrations, and sequenced on NovaSeq 6000 using a S1 flow cell with 150 paired end reads.

RNA Library Preparation and Sequencing

The quality of the extracted RNA was assessed on a BioAnalyzer (Agilent Technologies, Inc.). A total of 200 ng of RNA was used as input into the Illumina TruSeq Stranded Total library prep kit with RiboZero Plus rRNA depletion module (Illumina, Inc; Cat #20040529). Library construction was done according to the manufacturer instructions. Fragment size profiles and quantification of the libraries were measured using the Fragment Analyzer and Qubit (ThermoFisher Scientific), respectively. The libraries were normalized to 2 nM, pooled at equimolar concentrations, and sequenced on a NovaSeq 6000 using a S1 flow cell and 100 cycle paired end reads.

Paired metagenomic and transcriptomic analysis.

Raw sequence reads were run through TrimGalore (v 0.6.7) to remove Illumina adapters, bases with q-scores below 25, and reads less than 50 bps (https://github.com/FelixKrueger/TrimGalore). The trimmed reads were mapped against the mouse genome and coding domain sequences (GRCm39; GCA_000001635.9) and

the SILVA rRNA SSU and LSU Parc databases (release 138.1; https://doi.org/10.1093/nar/gks1219) to remove host and microbial rRNA reads using Bowtie2 (v 2.4.4; https://doi.org/10.1038%2Fnmeth.1923). Uracils within the SILVA databases were substituted for Thymine using the convert_rna.py utility script from KneadData (v 0.7.6). Taxonomic and functional profiling of the filtered reads was done using SqueezeMeta (v 1.6; https://doi.org/10.3389/fmicb.2018.03349) and HUManN (v 3.0.1; https://doi.org/10.7554%2FeLife.65088). SqueezeMeta was run in "merged" mode meaning reads are assembled at a per-sample level and then the resulting contigs are dereplicated and reassembled before taxonomic and functional annotation. A "merged" approach was chosen to overcome RAM and CPU limitations when analyzing the large number of deeply sequenced samples. Other important workflow parameters used include: 1) MEGAHIT (https://doi.org/10.1093/bioinformatics/btv033) for read assembly, 2) the use of both SqueezeMeta-specific scripts and CheckM (https://doi.org/10.1101%2Fgr.186072.114) for taxonomic classification of binned metagenomic assemblies, 3) bowtie2 for read mapping, and 4) removal of all contigs less than 500bps from downstream analysis. Additionally, all metatranscriptome samples were excluded from the contig binning process. This was done as the binning algorithms assume that all parts of the genome have approximately equal coverage. Metratranscriptome data has inherently uneven coverage as some genes are highly expressed relative to others and would bias the binning process unnecessarily. Taxonomic profiles were visualized in R version 4.2.2 using tidyverse_1.3.2. Functional data [KEGG orthologs (KO), protein families (Pfam), and clusters of orthologous groups of proteins (COG) output from SQM and pathway abundance(pathabund) and gene families(genefam) output from HUManN] were analyzed using Maaslin2_1.10.0.

REFERENCES

Under Development

FIGURES AND TABLES

Figures

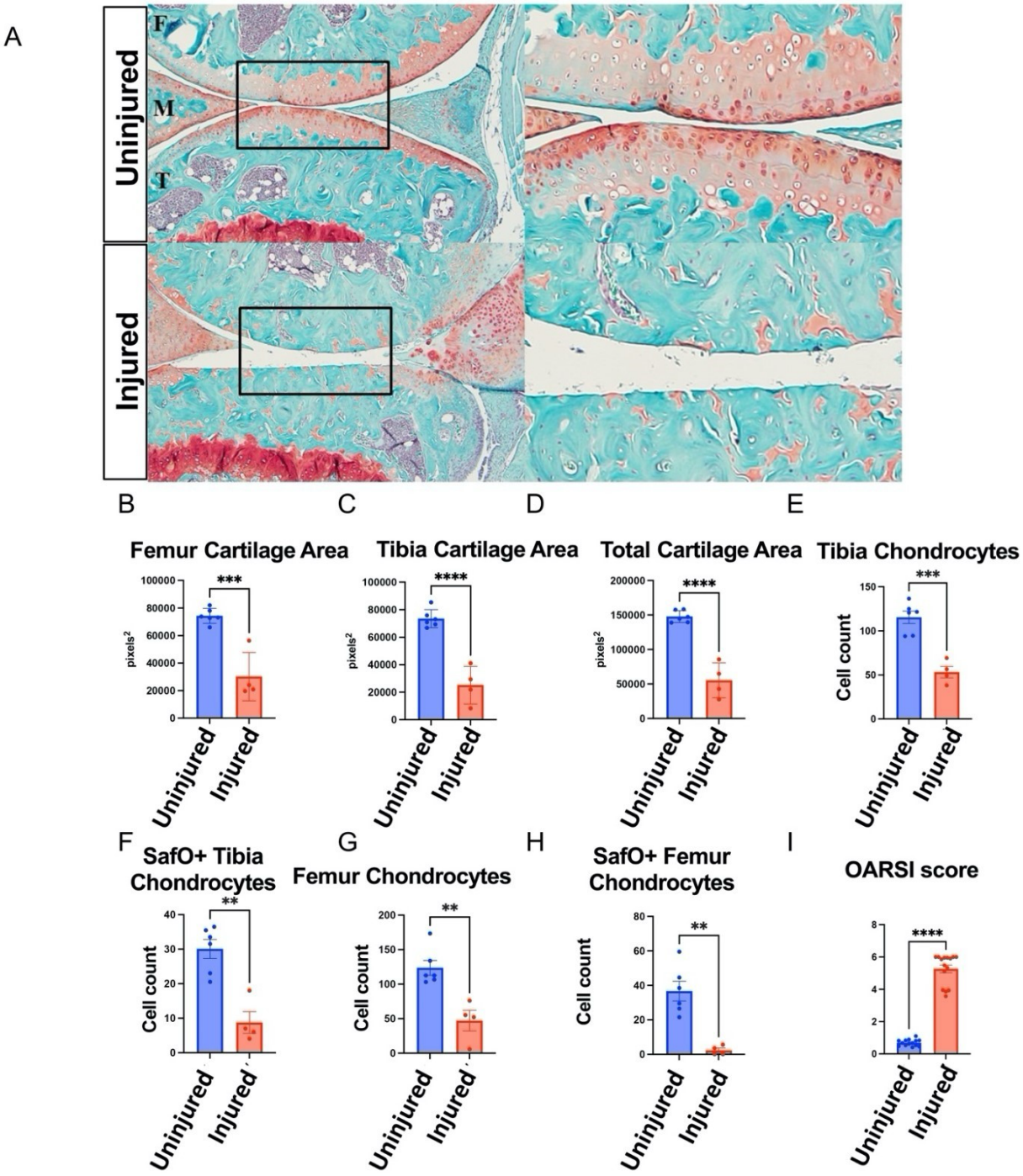

J

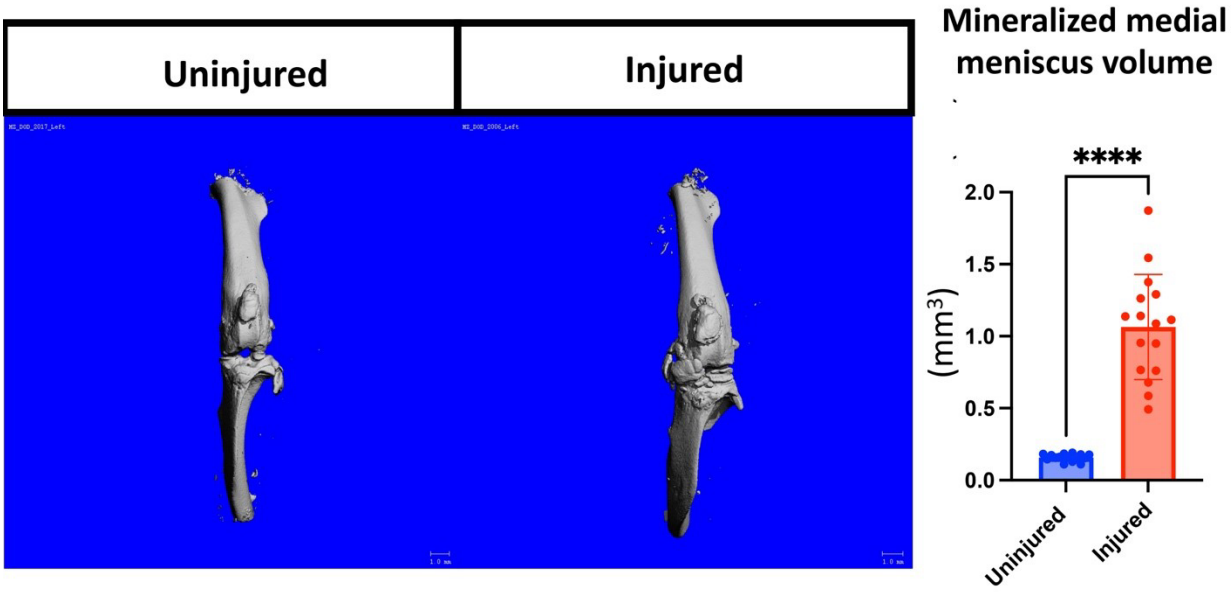

Figure 1. Mice develop PTOA upon DMM

a) Representative histological images of injured and uninjured joints. Graphs depicting the cartilage area in (b) the femur, (c) the tibia, and (d) the total cartilage area are presented. The number of chondrocytes in the (e) tibia, (f) matrix-producing SafO+ tibia, (g) femur, and (h) matrix-producing SafO+ femur chondrocytes were quantified. **i)** OARSI scoring confirms PTOA progression in the injured cohort. j) PTOA increases the amount of mineralized medial meniscus. Representative images from microCT of uninjured and injured joints. Injured animals with PTOA have a significant increase in the mineralized medial meniscus volume.
Student t-test was performed to determine statistical differences, with p values represented by *<0.05, ** <0.01, ***<0.001, and **** < 0.0001. All bars represent the group means (± SEM) with each dot representing the average measurement of three levels of histology. Each dot represents an individual joint, injured, or uninjured.

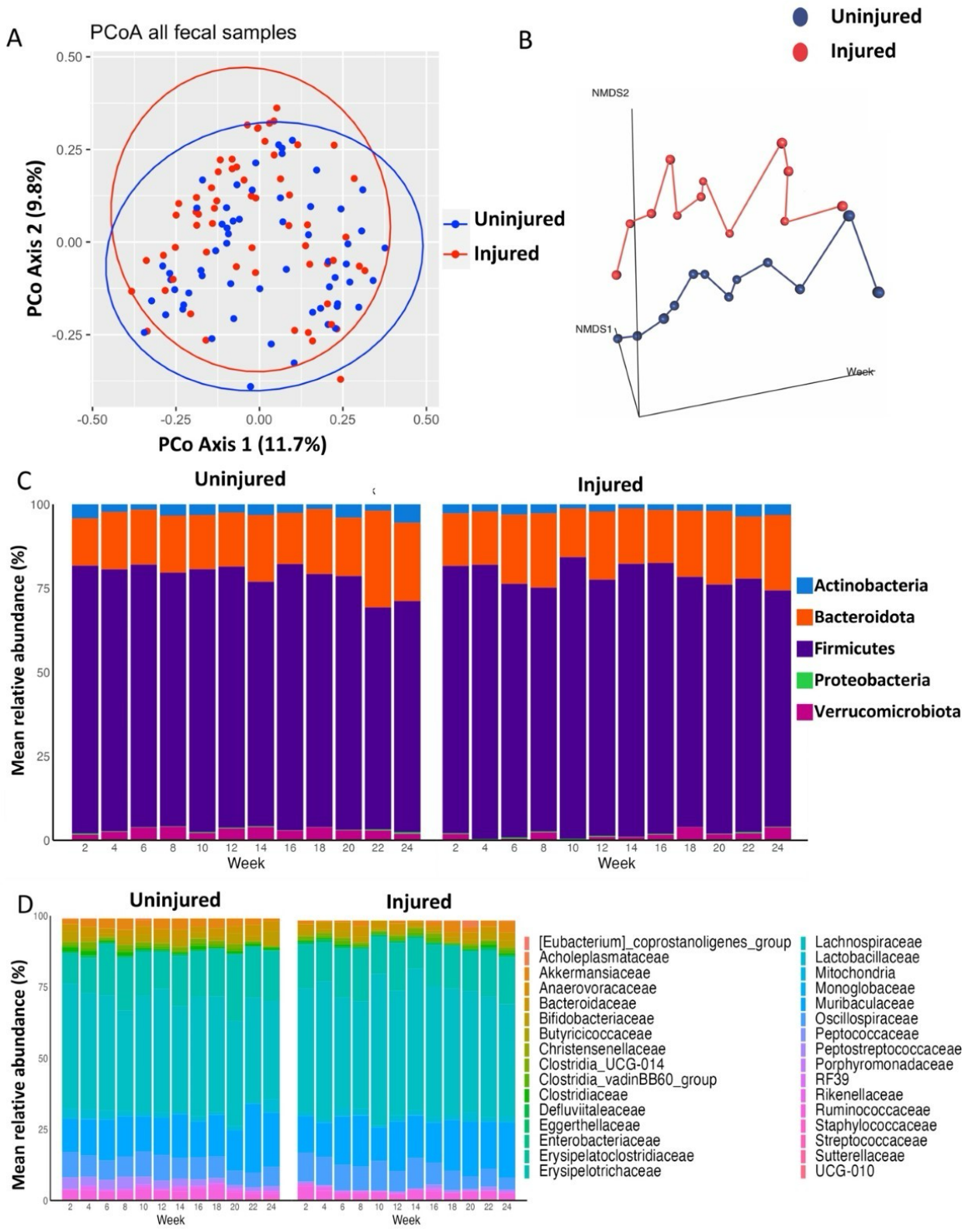
A
PCoA all fecal samples
PCo Axis 2 (9.8%)
PCo Axis 1 (11.7%)
Uninjured
Injured
B
Uninjured
Injured
NMDS2
NMDS1
Week
C
Uninjured
Injured
Mean relative abundance (%)
Week
Actinobacteria
Bacteroidota
Firmicutes
Proteobacteria
Verrucomicrobiota
D
Uninjured
Injured
Mean relative abundance (%)
Week
[Eubacterium]_coprostanoligenes_group
Acholeplasmataceae
Akkermansiaceae
Anaerovoracaceae
Bacteroidaceae
Bifidobacteriaceae
Butyricicoccaceae
Christensenellaceae
Clostridia_UCG-014
Clostridia_vadinBB60_group
Clostridiaceae
Defluviitaleaceae
Eggerthellaceae
Enterobacteriaceae
Erysipelatoclostridiaceae
Erysipelotrichaceae
Lachnospiraceae
Lactobacillaceae
Mitochondria
Monoglobaceae
Muribaculaceae
Oscillospiraceae
Peptococcaceae
Peptostreptococcaceae
Porphyromonadaceae
RF39
Rikenellaceae
Ruminococcaceae
Staphylococcaceae
Streptococcaceae
Sutterellaceae
UCG-010

Figure 2: PTOA does not alter the composition of the fecal microbiome in our cohort of animals. (a) Principal coordinate analysis (PCoA) was performed on all samples from initiation to end-stage disease. Each point represents a biweekly fecal sample, with the distance representing the dissimilarity between the samples. (b) Nonmetric multidimensional scaling was performed using averages of the Bray-Curtis distances at each time point for injured and uninjured animals. The average relative abundance of (c) phylum and (d) family over the course of the disease process. At each time point, an n=5 was used to generate the relative abundance plots.

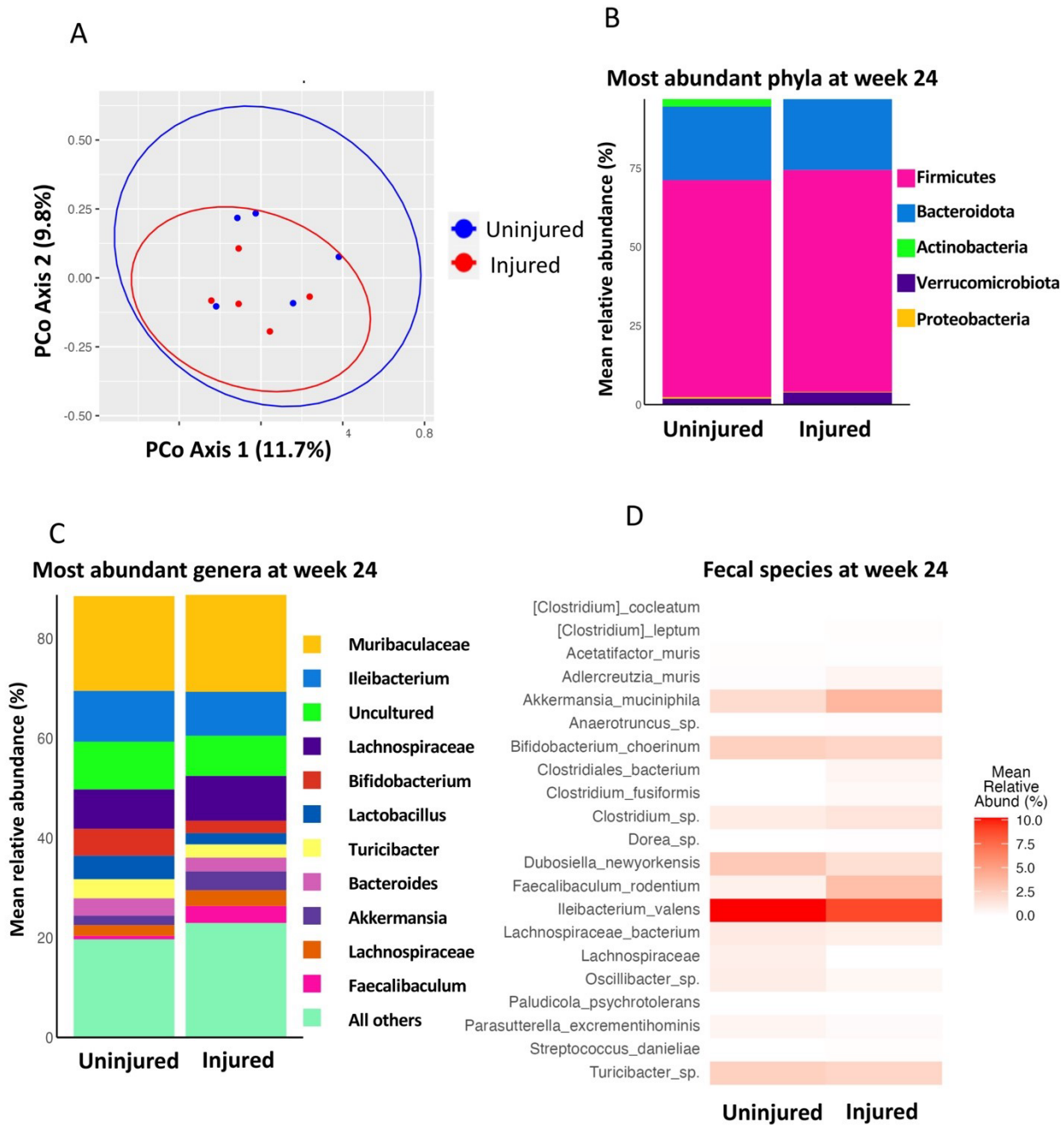

Figure 3: PTOA does not alter the composition of the gut microbiome in feces at the time of harvest in our cohort of animals. (a) PCoA plots of fecal samples collected 24 weeks after PTOA was generated. Each point represents a separate animal. The average relative abundance of (b) phyla and (c) genera of bacteria in the feces of injured and uninjured animals 24 weeks after disease onset. (d) a heat map of the bacteria species found in the feces of healthy and injured animals at harvest. An n=5 was used to generate the abundance plots.

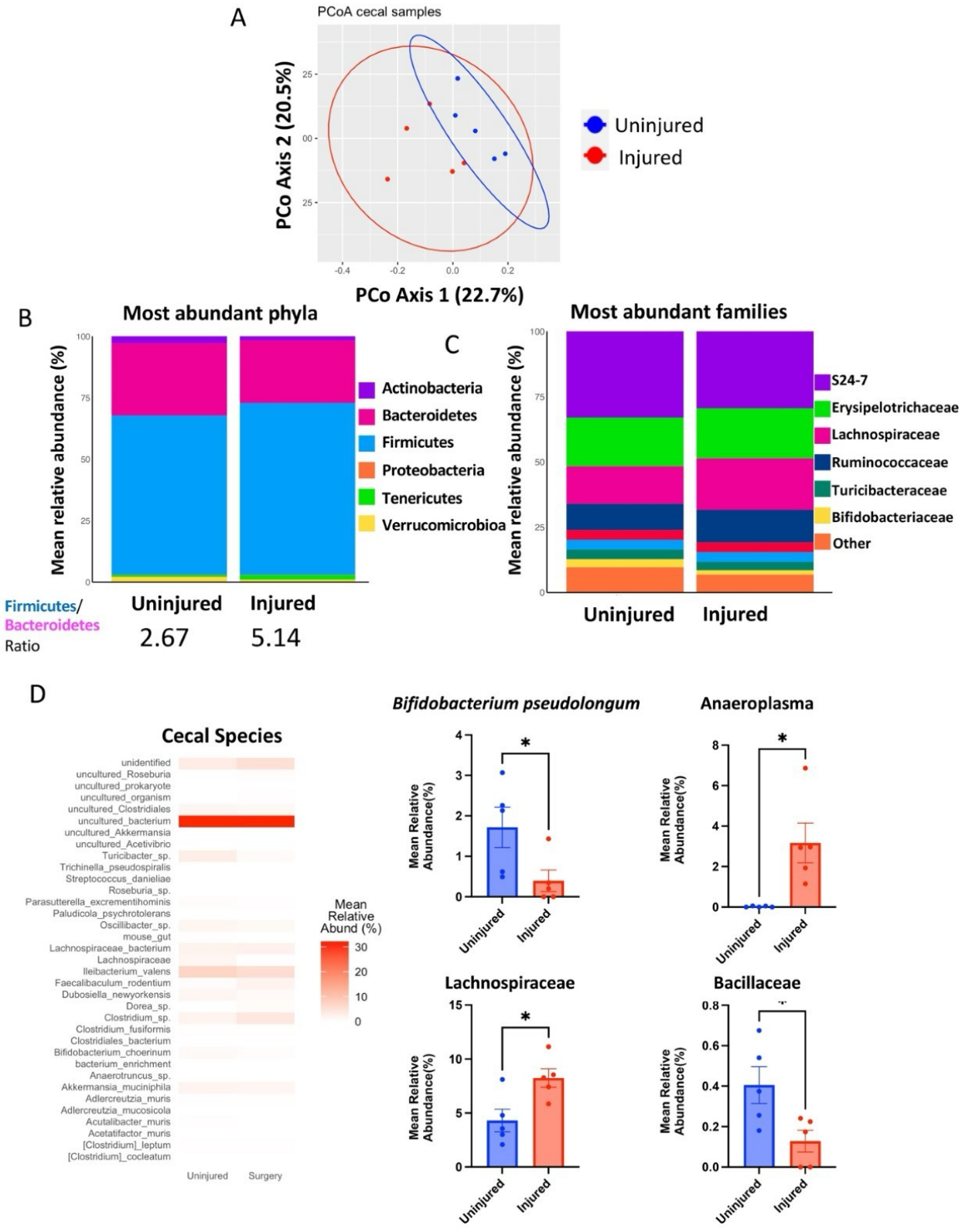
A
PCoA cecal samples
PCo Axis 2 (20.5%)
PCo Axis 1 (22.7%)
Uninjured
Injured
B
Most abundant phyla
Mean relative abundance (%)
Actinobacteria
Bacteroidetes
Firmicutes
Proteobacteria
Tenericutes
Verrucomicrobioa
Firmicutes/ Bacteroidetes Ratio
Uninjured
Injured
2.67
5.14
C
Most abundant families
S24-7
Erysipelotrichaceae
Lachnospiraceae
Ruminococcaceae
Turicibacteraceae
Bifidobacteriaceae
Other
D
Cecal Species
Mean Relative Abund (%)
Bifidobacterium pseudolongum
Anaeroplasma
Lachnospiraceae
Bacillaceae
Mean Relative Abundance(%)

Figure 4: End-stage PTOA does not alter the composition of the cecal microbiome by 16S rRNA sequencing in our cohort of animals. (a) PCoA analysis performed on the cecal microbiome, detailing the composition of the gut, is not dissimilar between injured and uninjured animals. Each point represents a separate animal cecal microbiome. The average (b) phylum and (c) family abundance was determined in cecal samples. Cecal samples (n = 5) were averaged and depicted in the bar charts. The Firmicutes-to-Bacteroides ratio was established by averaging the abundance of Firmicutes and Bacteroides present within the cecum. (d) A heat map was generated to visualize the abundances of bacteria present within the cecum. Graphs were then generated, displaying the bacteria at the genera, families, and species levels that differed between injured and uninjured animals. A student t-test was performed to determine statistical differences, with p values represented by *<0.05.

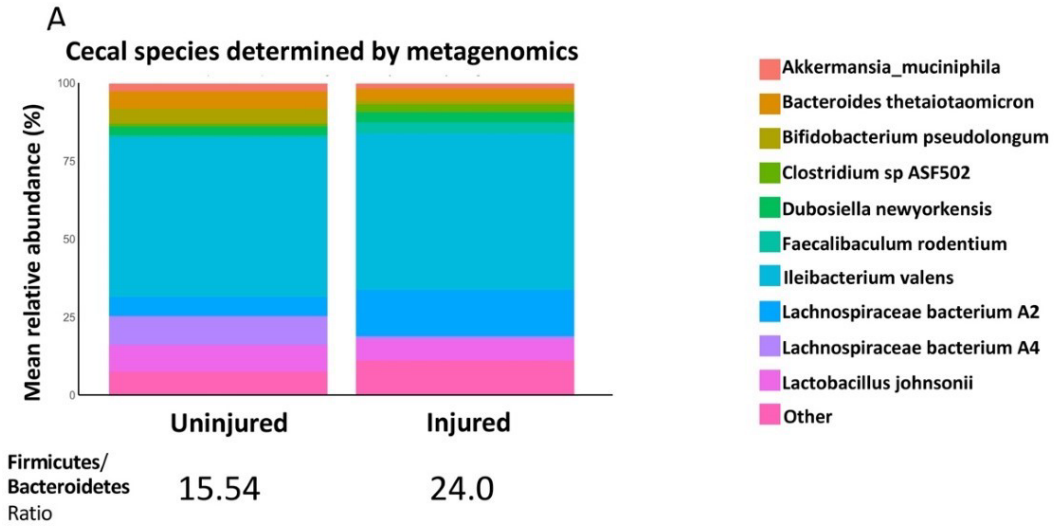
A
Cecal species determined by metagenomics
Mean relative abundance (%)
100
75
50
25
0
Uninjured
Injured
Akkermansia_muciniphila
Bacteroides thetaiotaomicron
Bifidobacterium pseudolongum
Clostridium sp ASF502
Dubosiella newyorkensis
Faecalibaculum rodentium
Ileibacterium valens
Lachnospiraceae bacterium A2
Lachnospiraceae bacterium A4
Lactobacillus johnsonii
Other
Firmicutes/ Bacteroidetes Ratio
15.54
24.0

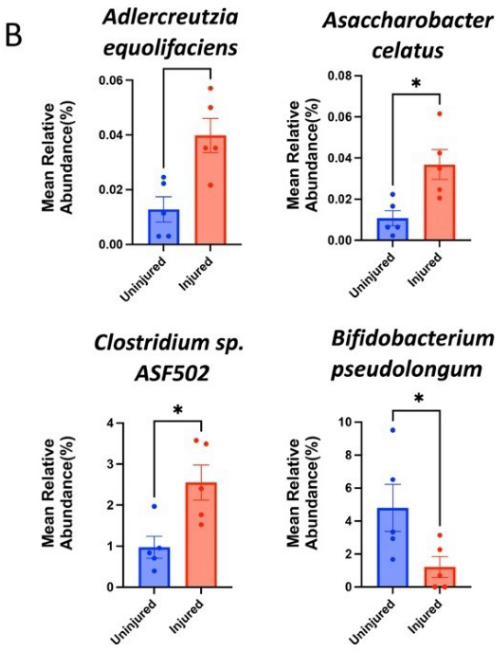
B
Adlercreutzia equolifaciens
Asaccharobacter celatus
Clostridium sp. ASF502
Bifidobacterium pseudolongum
Mean Relative Abundance(%)
Uninjured
Injured
*

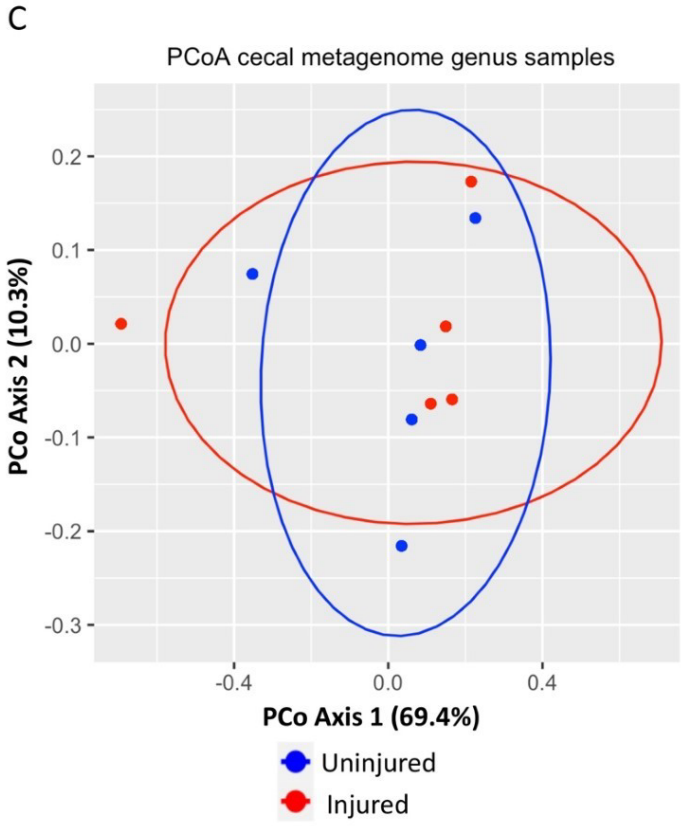
C
PCoA cecal metagenome genus samples
PCo Axis 2 (10.3%)
PCo Axis 1 (69.4%)
0.2
0.1
0.0
-0.1
-0.2
-0.3
-0.4
0.0
0.4
Uninjured
Injured

Figure 5: Metagenomic sequencing indicates a few compositional changes within the cecal microbiome in PTOA mice. (a) The average species abundance in the ceca was determined by metagenomic sequencing. The cecal samples (n = 5) were averaged to display the bar charts. The Firmicutes-to-Bacteroides ratio was determined by averaging the abundance of Firmicutes and Bacteroides in the cecum. (b) graphs showing the mean relative abundance of all significant bacterial species in the cecum (n = 5). (c) PCoA analysis was performed at the genus level from metagenomic data, with each dot representing one mouse. The statistical differences between bacteria were determined using a student t-test, with p values represented by *<0.05 and **<0.01.

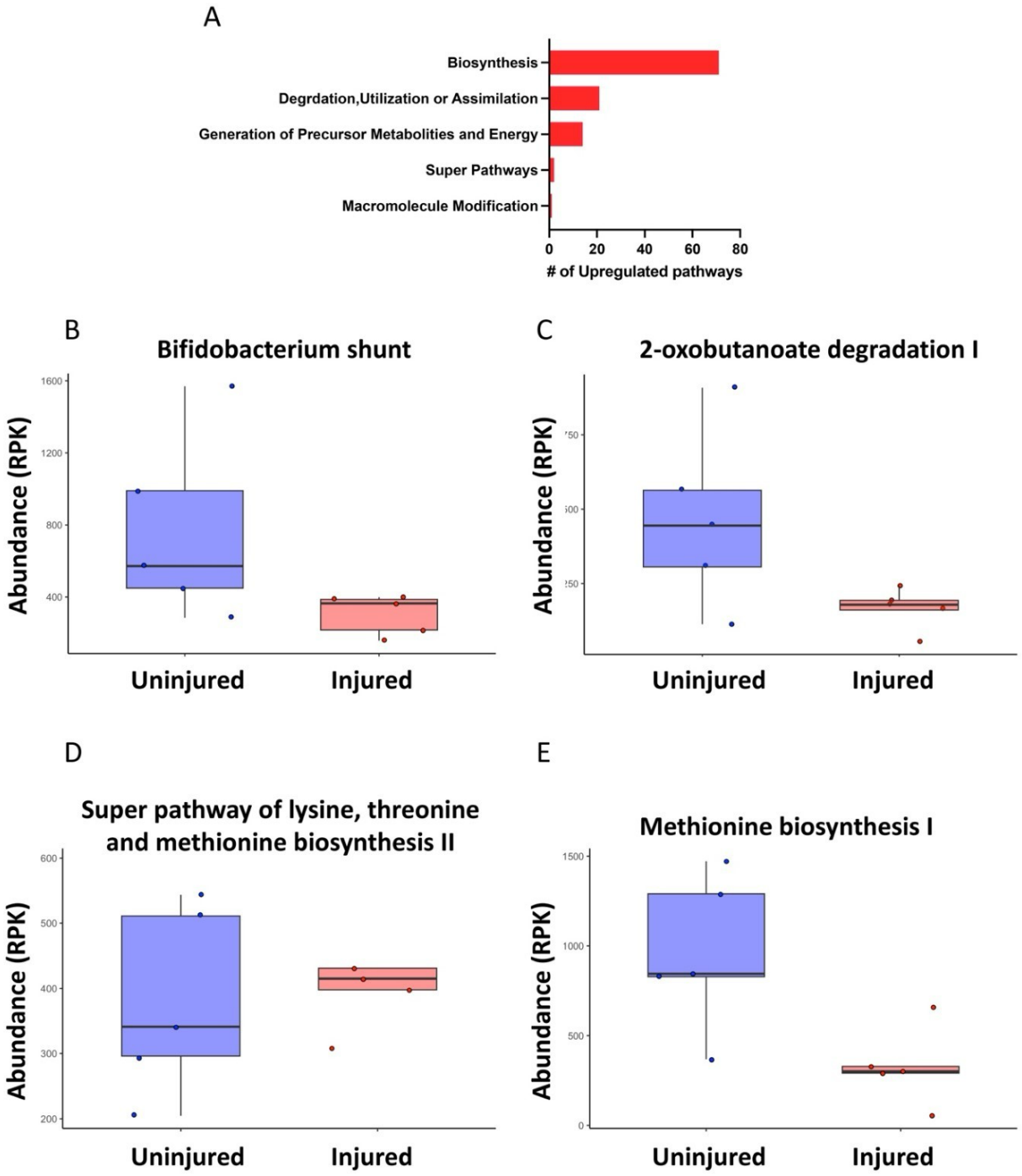
A
Biosynthesis
Degrdation,Utilization or Assimilation
Generation of Precursor Metabolities and Energy
Super Pathways
Macromolecule Modification
0
20
40
60
80
# of Upregulated pathways
B
Bifidobacterium shunt
Abundance (RPK)
1600
1200
800
400
Uninjured
Injured
C
2-oxobutanoate degradation I
Abundance (RPK)
Uninjured
Injured
D
Super pathway of lysine, threonine and methionine biosynthesis II
Abundance (RPK)
600
500
400
300
200
Uninjured
Injured
E
Methionine biosynthesis I
Abundance (RPK)
1500
1000
500
0
Uninjured
Injured

Figure 6. PTOA alters the functional capacity of the gut microbiome. (a) DNA metagenomic analysis reveals 110 pathways that are altered in abundance due to PTOA. Pathways associated with *Bifidobacterium* (b) *Bifidobacterium* shunt and SCFA production (c) 2-oxobutanoate degradation II were decreased in abundance due to the presence of PTOA at the DNA level. Methionine synthesis pathways (d) the super pathway of L-lysine, L-threonine, and L-methionine biosynthesis I, and (e) methionine biosynthesis I, were significantly increased in abundance within uninjured animals.

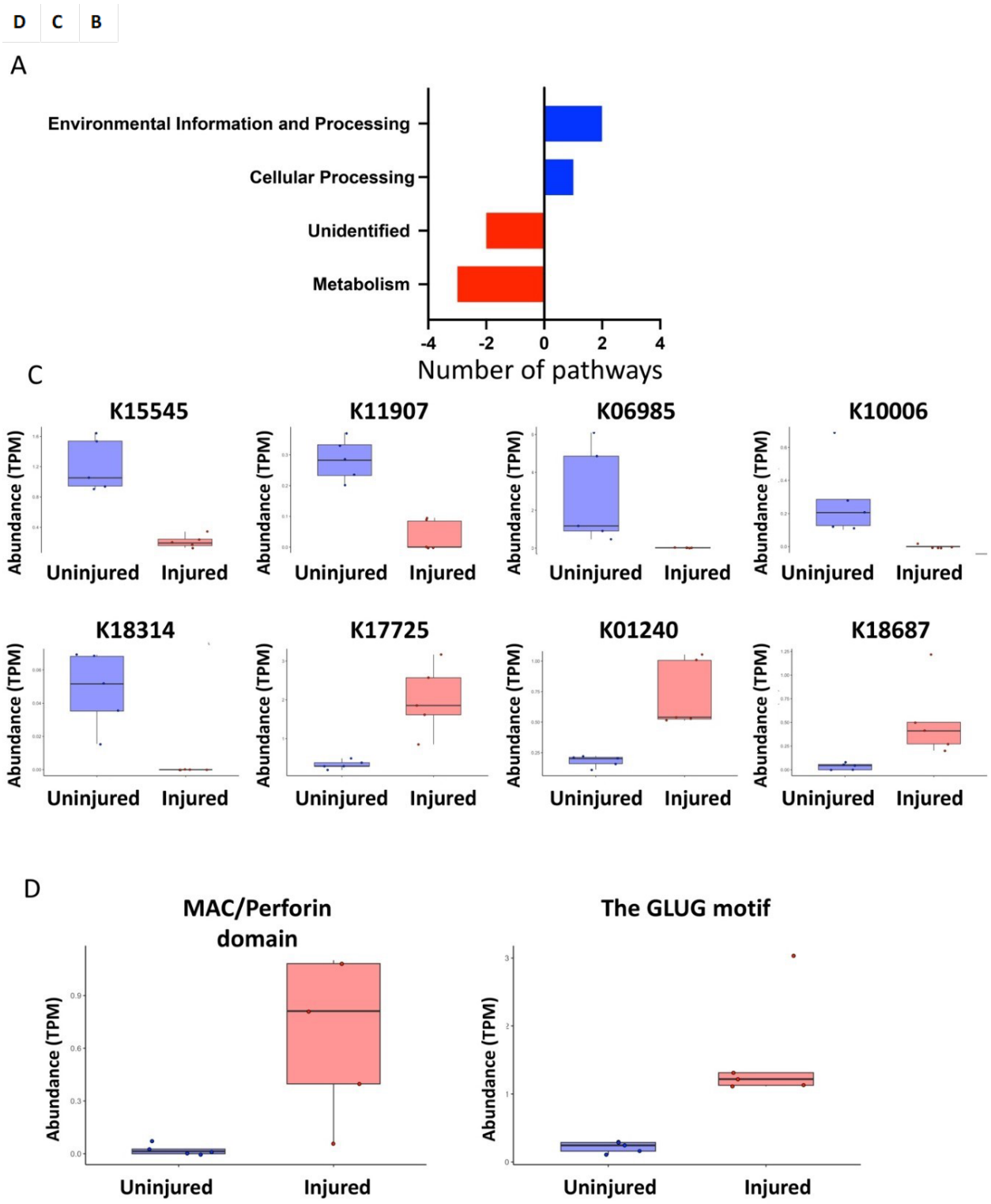

Figure 7: Meta transcriptomics of the cecal microbiota indicates that pathways associated with metabolism, bacterial competition, and immune system avoidance are upregulated

within the microbiome of animals with PTOA. (a) A total of 8 KEGG ortholog groups were differentially expressed between the gut microbiota of injured and uninjured animals. Blue bars represent ortholog groups that increased in expression in injured animals, with red bars indicating ortholog groups that decreased in expression in the injured cohort. (b) Graphs depicting the expression of all 8 KEGG orthologs are displayed (n = 5). Animals with PTOA have a significant increase in PFAMS (c) the Membrane Attack Complex/Perforin domain (MACPF); and (d) the GLUG motif. All graphs were generated with n = 5 from RNA metatranscriptomic sequencing.

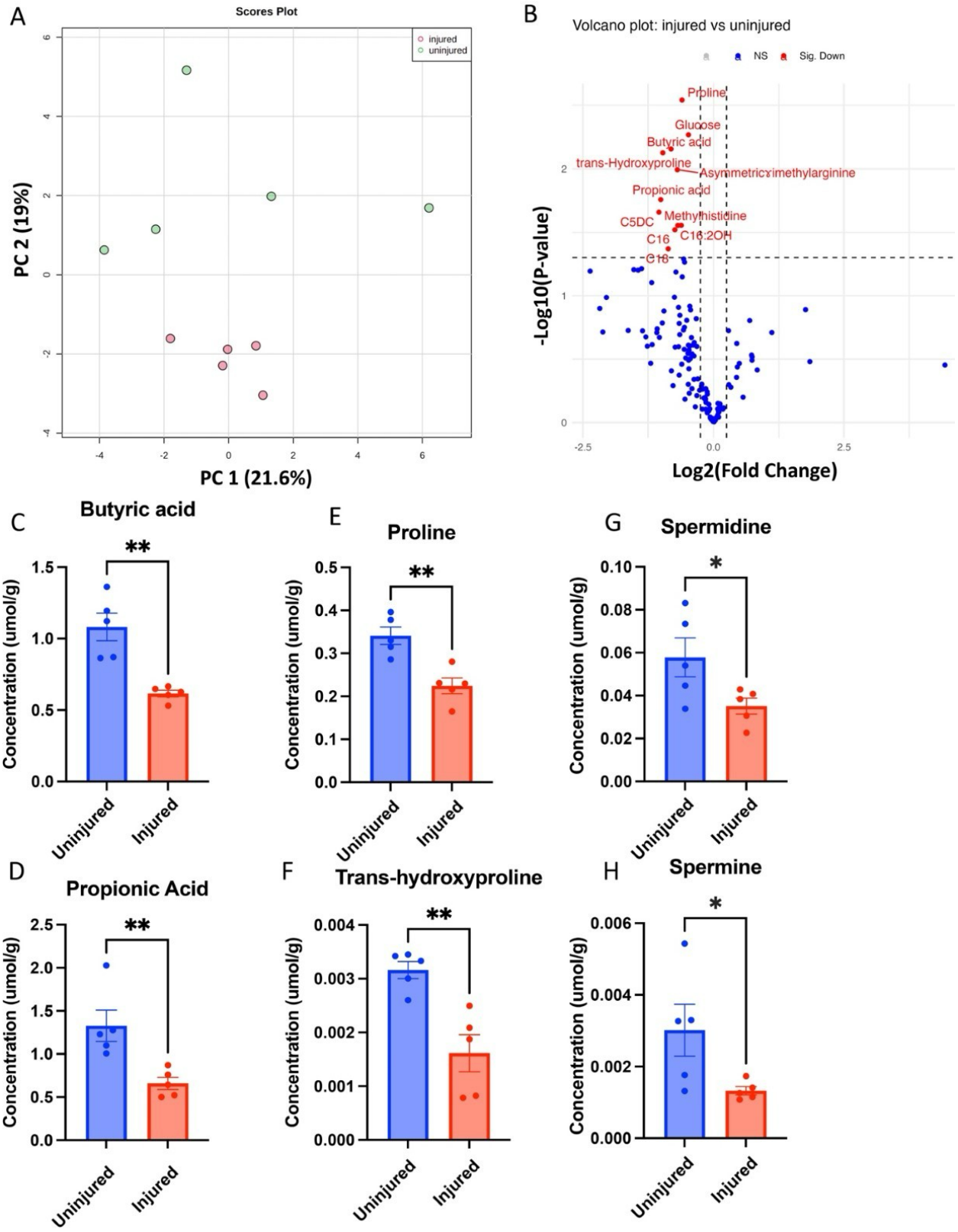
A
Scores Plot
injured
uninjured
PC 2 (19%)
PC 1 (21.6%)
B
Volcano plot: injured vs uninjured
NS
Sig. Down
Proline
Glucose
Butyric acid
trans-Hydroxyproline
Asymmetric dimethylarginine
Propionic acid
C5DC
Methylhistidine
C16
C16:2OH
C18
-Log10(P-value)
Log2(Fold Change)
C
Butyric acid
Concentration (umol/g)
Uninjured
Injured
E
Proline
G
Spermidine
D
Propionic Acid
F
Trans-hydroxyproline
H
Spermine

Figure 8. PTOA alters SCFAs, cartilage breakdown products, and polyamines within the fecal microbiome. PCA analysis was performed on all the metabolites assayed in the feces at end-stage PTOA. Each dot represents one animal, and the distance between each dot indicates the dissimilarity between animals. (b) A volcano plot displaying the metabolic differences between injured and uninjured animals. The concentrations of SCFAs (c) butyric acid and (d) propionic acid. The concentrations of cartilage breakdown products (e) proline and (f) trans-hydroxyproline. The concentrations of polyamines (g) spermidine and (h) spermine. All points represent one animal with an n=4 or 5. A student t test was utilized to determine significance on all graphs, with p values represented by *<0.05 and **<0.01. All graph bars represent the group mean (± SEM).

C B A

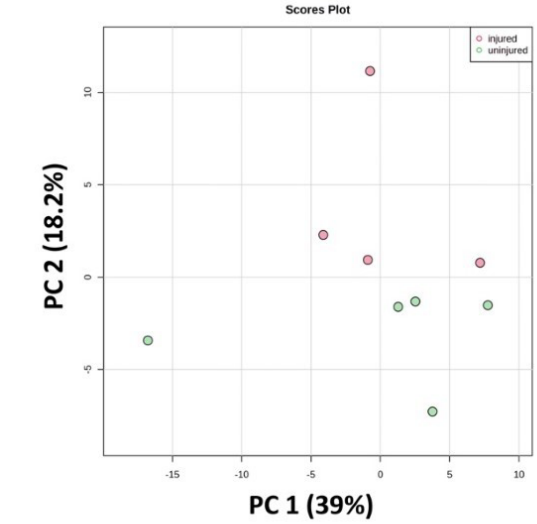
Scores Plot
injured
uninjured
PC 2 (18.2%)
PC 1 (39%)

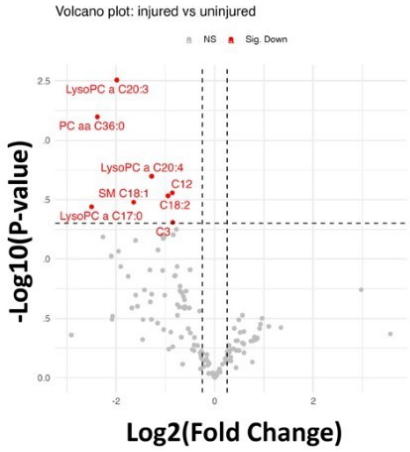
Volcano plot: injured vs uninjured
NS
Sig. Down
LysoPC a C20:3
PC aa C36:0
LysoPC a C20:4
C12
SM C18:1
C18:2
LysoPC a C17:0
C3
-Log10(P-value)
Log2(Fold Change)

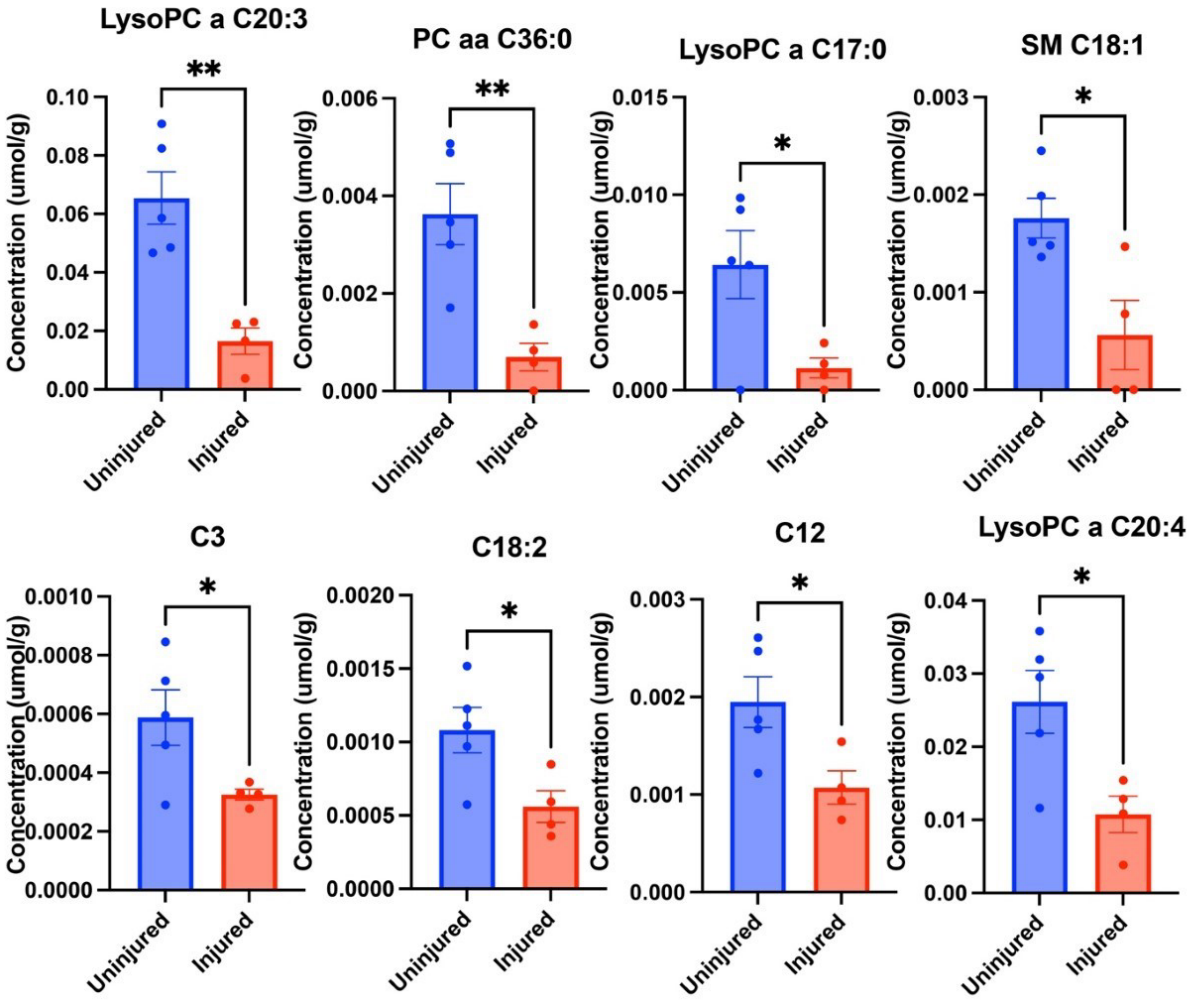
LysoPC a C20:3
PC aa C36:0
LysoPC a C17:0
SM C18:1
C3
C18:2
C12
LysoPC a C20:4
Concentration (umol/g)
Uninjured
Injured

Figure 9: Cecal metabolites are altered by PTOA, particularly lipid metabolites. PCA analysis was performed on all the metabolites assayed in the ceca at end-stage PTOA. Individual animals are represented by each dot, with the distance between each point representing the dissimilarity between the animals. (b) The volcano plot displaying the differences in metabolites between injured and uninjured animals. (c) The concentrations of significantly different metabolites, with each bar representing the group mean **(±** SEM). Significance for metabolites in (c) was determined using a student t test, with p values represented by *<0.05 and **<0.01.

B A

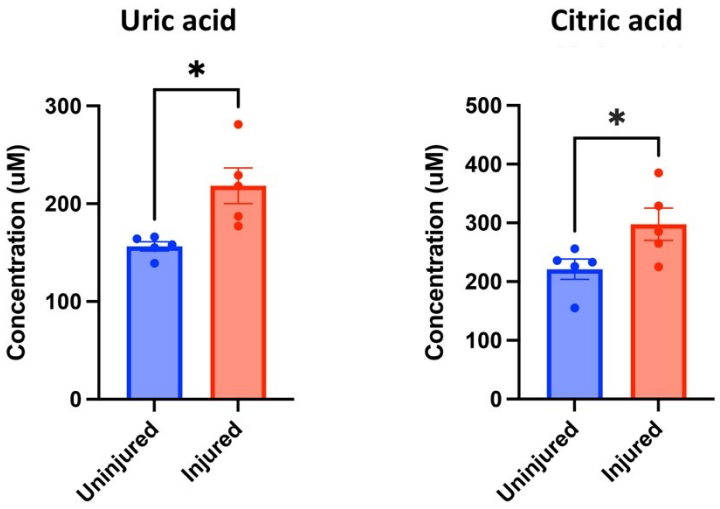

Figure 10. PTOA increases the amount of uric and citric acid in the serum. The concentration of (a) uric acid and (b) citric acid within the serum of injured and uninjured animals. All statistics are determined by a student t test, with p values represented by *<0.05. The group mean (SEM) is represented by each bar.

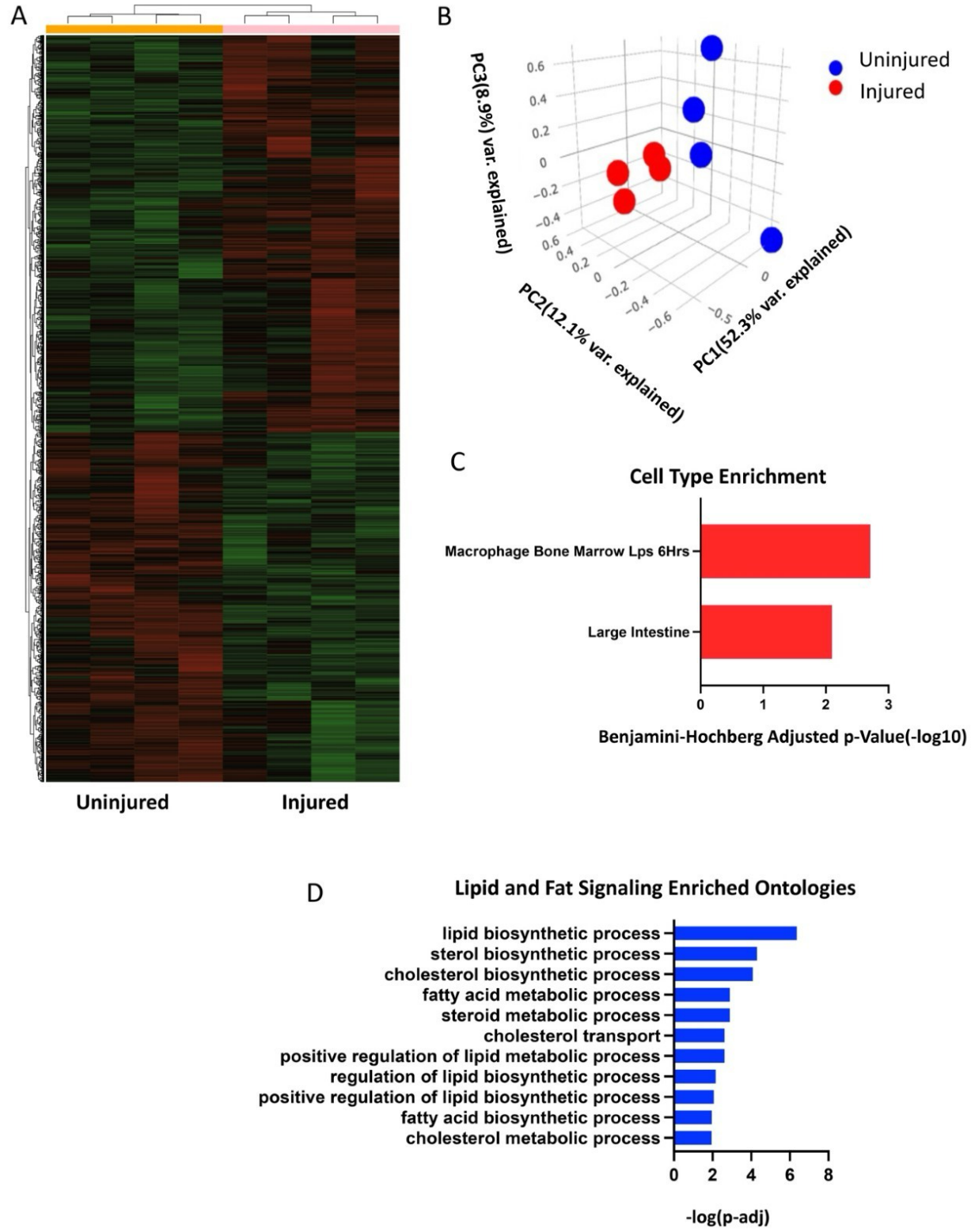
A
Uninjured
Injured
B
Uninjured
Injured
PC3(8.9%) var. explained)
PC2(12.1% var. explained)
PC1(52.3% var. explained)
C
Cell Type Enrichment
Macrophage Bone Marrow Lps 6Hrs
Large Intestine
Benjamini-Hochberg Adjusted p-Value(-log10)
D
Lipid and Fat Signaling Enriched Ontologies
lipid biosynthetic process
sterol biosynthetic process
cholesterol biosynthetic process
fatty acid metabolic process
steroid metabolic process
cholesterol transport
positive regulation of lipid metabolic process
regulation of lipid biosynthetic process
positive regulation of lipid biosynthetic process
fatty acid biosynthetic process
cholesterol metabolic process
-log(p-adj)

Figure 11. RNA-Seq indicates alterations in the colon transcriptome, with a reduction in pathways associated with fat signaling. (A) A heatmap displaying the clustering of differentially expressed genes in the colon. (b) A three-dimensional PCoA analysis was performed on the expression profiles of all animals, with each dot representing one animal. (c) Cell type enrichment was performed with cTen using the DEG list. PTOA was associated with a macrophage cell type. (d) Of the top 25 enriched ontologies, 11 of them are associated with lipid and fat signaling. These 11 ontologies are depicted with a log (p-adjusted) value displayed to visualize the differences.

Tables

Table 1: Significantly altered pathways by DNA metagenomic analysis. All significantly abundant pathways as identified by HUMAnN 3. All values are listed in rank order, with the most upregulated displayed first. Values in orange cells represent pathways that are increased in abundance in injured animals. Qval represents the p-adjusted value, with.25 used as a cutoff for significance.

feature	value	coef	stderr	pval	qval	Classification
PWY-7434	uninjured	-1.7242202	0.3243472	0.0007145	0.1207499	Macromolecule Modification
PWY-7616	uninjured	1.8016242	0.3269436	0.0005666	0.1207499	Degradation/Utilization/Assimilation
PWY-4041	uninjured	0.7275955	0.1472834	0.0011349	0.1278672	Biosynthesis
UNINTEGRATED	uninjured	0.2851778	0.1263962	0.0540401	0.2248389	#N/A
BRANCHED-CHAIN-AA-SYN-PWY	uninjured	0.3780560	0.1454223	0.0316320	0.2248389	Biosynthesis
COBALSYN-PWY	uninjured	0.6404560	0.1877247	0.0092003	0.2248389	Biosynthesis
COLANSYN-PWY	uninjured	0.4869272	0.2098130	0.0488609	0.2248389	Biosynthesis
COMPLETE-ARO-PWY	uninjured	0.3342835	0.1480264	0.0538676	0.2248389	Biosynthesis
GLCMANNANAUT-PWY	uninjured	0.3040811	0.1345827	0.0537696	0.2248389	Degradation/Utilization/Assimilation
GLUCONEO-PWY	uninjured	0.6753414	0.3033035	0.0565947	0.2248389	Biosynthesis
HISDEG-PWY	uninjured	1.0801662	0.4083266	0.0294677	0.2248389	Degradation/Utilization/Assimilation
HOMOSER-METSYN-PWY	uninjured	1.7810333	0.6906938	0.0326866	0.2248389	Biosynthesis
ILEUSYN-PWY	uninjured	0.3525413	0.1440216	0.0400717	0.2248389	Biosynthesis
MET-SAM-PWY	uninjured	1.8458445	0.7062878	0.0309641	0.2248389	Biosynthesis
METSYN-PWY	uninjured	1.7296420	0.6741431	0.0333504	0.2248389	Biosynthesis
NONMEVIPP-PWY	uninjured	0.3023070	0.1271271	0.0446855	0.2248389	Biosynthesis
NONOXIPENT-PWY	uninjured	0.2698923	0.1174256	0.0505962	0.2248389	Generation of Precursor Metabolites and Energy
P122-PWY	uninjured	1.1684487	0.4930070	0.0452432	0.2248389	Generation of Precursor Metabolites and Energy
P124-PWY	uninjured	1.178405	0.5089105	0.0492608	0.2248389	Degradation/Utilization/Assimilation
P162-PWY	uninjured	0.6379860	0.2550389	0.0368544	0.2248389	Degradation/Utilization/Assimilation

P4-PWY	uninjured	1.46896972	0.65690683	0.05575575	0.2248389	Biosynthesis
P42-PWY	uninjured	0.78090717	0.24864973	0.01379292	0.2248389	Degradation/Utilization/Assimilation
P441-PWY	uninjured	0.65957858	0.28751369	0.05093963	0.2248389	Degradation/Utilization/Assimilation
P461-PWY	uninjured	0.69638748	0.26332192	0.02950087	0.2248389	Degradation/Utilization/Assimilation
PANTO-PWY	uninjured	0.49246267	0.16849219	0.01920983	0.2248389	Biosynthesis
PANTOSYN-PWY	uninjured	0.43462868	0.1722755	0.03564908	0.2248389	Biosynthesis
PENTOSE-P-PWY	uninjured	0.9527345	0.3816468	0.03715115	0.2248389	Generation of Precursor Metabolites and Energy
PEPTIDOGLYCANSYN-PWY	uninjured	0.35610326	0.11770988	0.01642739	0.2248389	Biosynthesis
PHOSLIPSYN-PWY	uninjured	1.25269238	0.38701734	0.01193496	0.2248389	Biosynthesis
PRPP-PWY	uninjured	1.8351902	0.6492363	0.02226334	0.2248389	Superpathways
PWY-241	uninjured	2.8547415	1.13183599	0.03568507	0.2248389	Generation of Precursor Metabolites and Energy
PWY-5030	uninjured	1.09503141	0.40946055	0.02817263	0.2248389	Degradation/Utilization/Assimilation
PWY-5100	uninjured	0.50014818	0.13160799	0.00523452	0.2248389	Generation of Precursor Metabolites and Energy
PWY-5103	uninjured	0.40616559	0.1562243	0.03162334	0.2248389	Biosynthesis
PWY-5345	uninjured	1.37146804	0.57535533	0.04428995	0.2248389	Biosynthesis
PWY-5347	uninjured	1.69187862	0.6618642	0.03384481	0.2248389	Biosynthesis
PWY-5659	uninjured	0.45092145	0.17214951	0.03068097	0.2248389	Biosynthesis
PWY-6125	uninjured	1.16721436	0.46308483	0.03577981	0.2248389	Biosynthesis
PWY-6126	uninjured	1.16503362	0.48489061	0.04299699	0.2248389	Biosynthesis
PWY-6168	uninjured	0.95430113	0.29055846	0.01111507	0.2248389	Biosynthesis
PWY-6385	uninjured	0.34673141	0.11134193	0.01435591	0.2248389	Biosynthesis
PWY-6386	uninjured	0.37274021	0.11363316	0.01118436	0.2248389	Biosynthesis
PWY-6387	uninjured	0.27810897	0.11637263	0.04386855	0.2248389	Biosynthesis
PWY-6545	uninjured	0.79914786	0.35361633	0.05372833	0.2248389	Biosynthesis

PWY-6583	uninjured	0.44186542	0.19786425	0.05601884	0.2248389	Generation of Precursor Metabolites and Energy
PWY-6901	uninjured	0.84448773	0.33546681	0.03595683	0.2248389	Degradation/Utilization/Assimilation
PWY-6902	uninjured	0.70295466	0.3166869	0.05720753	0.2248389	Degradation/Utilization/Assimilation
PWY-6936	uninjured	2.05207004	0.76794359	0.02826732	0.2248389	Biosynthesis
PWY-6969	uninjured	0.91780598	0.25358032	0.00678866	0.2248389	Generation of Precursor Metabolites and Energy
PWY-7115	uninjured	1.01201591	0.41567942	0.04090721	0.2248389	Generation of Precursor Metabolites and Energy
PWY-7117	uninjured	2.76693746	1.1170647	0.0382928	0.2248389	Generation of Precursor Metabolites and Energy
PWY-7184	uninjured	0.81032487	0.35604991	0.05240771	0.2248389	Biosynthesis
PWY-7196	uninjured	2.57978153	0.83831947	0.01517835	0.2248389	Biosynthesis
PWY-7197	uninjured	1.07211594	0.37425697	0.02100076	0.2248389	Biosynthesis
PWY-7198	uninjured	0.71574774	0.26047313	0.02514133	0.2248389	Biosynthesis
PWY-7199	uninjured	0.59551276	0.20735088	0.02076489	0.2248389	Biosynthesis
PWY-7208	uninjured	1.05767177	0.36742927	0.02055654	0.2248389	Biosynthesis
PWY-7210	uninjured	0.79871793	0.31946056	0.03693005	0.2248389	Biosynthesis
PWY-7211	uninjured	0.97605426	0.37196245	0.03045754	0.2248389	Biosynthesis
PWY-7220	uninjured	1.24998535	0.5141876	0.04113861	0.2248389	Biosynthesis
PWY-7222	uninjured	1.24998535	0.5141876	0.04113861	0.2248389	Biosynthesis
PWY-7228	uninjured	1.08149104	0.41691938	0.03191379	0.2248389	Degradation/Utilization/Assimilation
PWY-7229	uninjured	1.10591502	0.49447253	0.05572417	0.2248389	Degradation/Utilization/Assimilation
PWY-7234	uninjured	2.49348075	0.93233785	0.02816774	0.2248389	Biosynthesis
PWY-724	uninjured	0.42119658	0.17904718	0.04650427	0.2248389	Biosynthesis
PWY-7282	uninjured	1.14544779	0.45908309	0.03722651	0.2248389	Biosynthesis
PWY-7400	uninjured	0.65928115	0.28259697	0.04794132	0.2248389	Biosynthesis
PWY-7456	uninjured	0.55108805	0.21958566	0.03638951	0.2248389	Degradation/Utilization/Assimilation

PWY-7948	uninjured	0.78693128	0.19961051	0.0042818	0.2248389	Degradation/Utilization/Assimilation
PWY-7953	uninjured	0.36421194	0.1137434	0.0125735	0.2248389	Biosynthesis
PWY-8004	uninjured	1.2134309	0.46918951	0.032302	0.2248389	Degradation/Utilization/Assimilation
PWY-8178	uninjured	0.33553467	0.14487692	0.049226	0.2248389	Generation of Precursor Metabolites and Energy
PWY-8182	uninjured	0.6042541	0.14209647	0.0027899	0.2248389	Degradation/Utilization/Assimilation
PWY-841	uninjured	0.99784743	0.4265276	0.0474551	0.2248389	Biosynthesis
PWY0-1586	uninjured	0.47352928	0.15786895	0.0170844	0.2248389	Biosynthesis
PWY0-162	uninjured	1.05418394	0.32467455	0.0117556	0.2248389	Biosynthesis
PWY0-781	uninjured	1.55455599	0.6505806	0.0438907	0.2248389	Superpathways
PWY0-845	uninjured	1.34117258	0.50987961	0.0301608	0.2248389	Biosynthesis
PWY4FS-7	uninjured	1.38112963	0.53095082	0.0315570	0.2248389	Biosynthesis
PWY4FS-8	uninjured	1.38112963	0.53095082	0.0315570	0.2248389	Biosynthesis
PWY66-409	uninjured	0.80870711	0.3552459	0.0523589	0.2248389	Biosynthesis
PWY66-429	uninjured	0.45162839	0.19424733	0.0485377	0.2248389	Biosynthesis
PYRIDNUCSYN-PWY	uninjured	0.49466832	0.22205104	0.0564972	0.2248389	Biosynthesis
PYRIDOXSYN-PWY	uninjured	1.37336403	0.51778787	0.0291485	0.2248389	Biosynthesis
RIBOSYN2-PWY	uninjured	0.47482779	0.19640506	0.0420074	0.2248389	Biosynthesis
THRESYN-PWY	uninjured	0.39840612	0.15833083	0.0360163	0.2248389	Biosynthesis
PWY-1042	uninjured	0.29798843	0.13880741	0.0640963	0.2266670	Generation of Precursor Metabolites and Energy
PWY-5097	uninjured	0.3312793	0.15392027	0.0635493	0.2266670	Biosynthesis
PWY-5130	uninjured	1.34778626	0.62864537	0.0643788	0.2266670	Degradation/Utilization/Assimilation
PWY-5265	uninjured	1.18096914	0.53703195	0.0590798	0.2266670	Biosynthesis
PWY-5686	uninjured	0.30892553	0.14261781	0.0621946	0.2266670	Biosynthesis
PWY-6121	uninjured	0.28589192	0.13140561	0.0612770	0.2266670	Biosynthesis

PWY-7221	uninjured	0.38119334	0.17326613	0.05898974	0.2266704	Biosynthesis
PWY-7790	uninjured	0.30892553	0.14261781	0.06219465	0.2266704	Biosynthesis
PWY-7791	uninjured	0.30892553	0.14261781	0.06219465	0.2266704	Biosynthesis
TRNA-CHARGING-PWY	uninjured	0.28088193	0.13006386	0.06283153	0.2266704	Biosynthesis
PWY-2942	uninjured	0.34087674	0.16008627	0.06586148	0.2294967	Biosynthesis
DTDPRHAMSYN-PWY	uninjured	0.20220259	0.09607469	0.06844177	0.2352223	Biosynthesis
PWY-7316	uninjured	-1.8604526	0.88576829	0.06889647	0.2352223	Biosynthesis
ARGSYNBSUB-PWY	uninjured	0.28671391	0.14050087	0.07559685	0.2390106	Biosynthesis
ARO-PWY	uninjured	0.28873117	0.14126046	0.07520976	0.2390106	Biosynthesis
GLYCOLYSIS-E-D	uninjured	0.57461555	0.27726021	0.07195153	0.2390106	Generation of Precursor Metabolites and Energy
P41-PWY	uninjured	0.57226105	0.27978579	0.07504752	0.2390106	Generation of Precursor Metabolites and Energy
PWY-5136	uninjured	0.38785029	0.18878715	0.07399721	0.2390106	Biosynthesis
PWY-5913	uninjured	1.37615407	0.67455556	0.07566327	0.2390106	Generation of Precursor Metabolites and Energy
PWY-6147	uninjured	1.06387092	0.51237651	0.07152024	0.2390106	Biosynthesis
PWY-6992	uninjured	0.97966821	0.48015766	0.07563799	0.2390106	Degradation/Utilization/Assimilation
GLYCOGENSYNTH-PWY	uninjured	0.31936752	0.15789122	0.07773173	0.2410397	Biosynthesis
P221-PWY	uninjured	-1.0586785	0.52324828	0.07766247	0.2410397	Degradation/Utilization/Assimilation
PWY-7237	uninjured	0.27930682	0.13890942	0.07919077	0.2433316	Degradation/Utilization/Assimilation

Table 2. The abundance of KEGG orthologs identified by shotgun metagenomics of DNA from the gut microbiome of injured mice. The abundance of KEGG orthologs is represented in the table. Negative values are indicated in red and indicate values that are upregulated in injured animals. Maaslin2 was used to generate values with standard qval of .25 classified as significant.

feature	value	coef	stderr	pval	qval
K15505	uninjured	4.538121229	0.461571705	9.63E-06	0.016007809
K15780	uninjured	-4.231839592	0.437216812	1.08E-05	0.016007809
K18314	uninjured	1.420384857	0.135185706	5.86E-06	0.016007809
K21453	uninjured	5.464832615	0.565069815	1.09E-05	0.016007809
K22297	uninjured	1.564579719	0.170562642	1.61E-05	0.018941302
K01178	uninjured	-5.491483761	0.629425169	2.33E-05	0.022808849
K15545	uninjured	3.062632302	0.363171225	2.98E-05	0.025050169
K00094	uninjured	5.111159919	0.641869883	4.52E-05	0.026086488
K02100	uninjured	2.753533584	0.33902241	3.92E-05	0.026086488
K08783	uninjured	-3.471249633	0.4406677	4.88E-05	0.026086488
K12152	uninjured	-5.229466974	0.651614589	4.27E-05	0.026086488
K03680	uninjured	4.328974413	0.561705795	5.71E-05	0.027966308
K01707	uninjured	1.411411941	0.193442608	8.42E-05	0.038079687
K21400	uninjured	2.506342322	0.350626145	9.73E-05	0.040851191
K22307	uninjured	-2.374452086	0.339453813	0.000113211	0.044378848
K06937	uninjured	1.038040365	0.157323099	0.000169715	0.062370164
K15771	uninjured	-0.496656757	0.077070349	0.000199534	0.06901523
K04518	uninjured	-0.896361572	0.141926068	0.000228887	0.070834518
K07511	uninjured	-4.266826101	0.670580956	0.000217589	0.070834518
K20448	uninjured	-1.585868987	0.255319856	0.000256255	0.07533886
K00682	uninjured	-1.327493947	0.223265521	0.000343589	0.077733105
K00701	uninjured	-3.319695172	0.545192788	0.000292994	0.077733105
K05349	uninjured	-0.262903655	0.043883542	0.000326677	0.077733105
K05613	uninjured	0.773182601	0.126276073	0.00028225	0.077733105
K05964	uninjured	0.723668207	0.121717512	0.000343718	0.077733105
K07126	uninjured	-0.490935641	0.081661973	0.00031917	0.077733105
K04792	uninjured	5.580379272	0.945252933	0.000360288	0.07846268
K13735	uninjured	1.879887306	0.329145287	0.00044844	0.094172346
K01115	uninjured	2.520101273	0.452989966	0.000532631	0.094905168
K03928	uninjured	-1.371518933	0.242754877	0.00048153	0.094905168
K06900	uninjured	1.687651127	0.302434088	0.000522162	0.094905168
K21399	uninjured	2.956548771	0.527065962	0.000504658	0.094905168
K21909	uninjured	1.744744125	0.312693585	0.000522469	0.094905168

K01160	uninjured	1.172959633	0.217466862	0.000650863	0.109611948
K16928	uninjured	-2.079340977	0.385656112	0.000652452	0.109611948
K03315	uninjured	0.472528626	0.089874731	0.000766698	0.125065849
K08965	uninjured	1.135346326	0.216829036	0.000786979	0.125065849
K03780	uninjured	-1.800853787	0.349507427	0.000871593	0.134867481
K01431	uninjured	1.271847773	0.252564488	0.001006952	0.137694891
K08258	uninjured	4.454460289	0.876796761	0.000952683	0.137694891
K11144	uninjured	-1.051553228	0.206322789	0.000933716	0.137694891
K22222	uninjured	1.861237412	0.368424692	0.000986946	0.137694891
K22399	uninjured	-1.999807216	0.394981818	0.000973376	0.137694891
K17994	uninjured	2.014823803	0.403255544	0.001057579	0.141331064
K03839	uninjured	0.619301159	0.126864684	0.001221898	0.159661367
K01629	uninjured	-0.635249788	0.130614992	0.001250191	0.159807066
K21905	uninjured	3.685498004	0.770422334	0.001384032	0.173151256
K00142	uninjured	2.234468758	0.476022682	0.00155339	0.173440371
K04715	uninjured	1.588050392	0.338667623	0.001563323	0.173440371
K07978	uninjured	-2.489653324	0.526197893	0.001480252	0.173440371
K09284	uninjured	5.052473287	1.075334761	0.001544429	0.173440371
K10918	uninjured	2.808799369	0.592876727	0.001468527	0.173440371
K11907	uninjured	2.756284475	0.580946648	0.00145556	0.173440371
K00848	uninjured	-0.250435656	0.054381522	0.001743652	0.178026272
K02636	uninjured	-0.486726185	0.104776478	0.001654597	0.178026272
K09695	uninjured	1.155389713	0.249949323	0.001704642	0.178026272
K10716	uninjured	0.452030401	0.098272958	0.001756041	0.178026272
K14392	uninjured	-1.48828805	0.323133563	0.001742201	0.178026272
K07699	uninjured	-0.410662856	0.090122958	0.001857956	0.1791948
K09607	uninjured	1.28036209	0.281775933	0.001889469	0.1791948
K11356	uninjured	1.953660471	0.429793157	0.001885294	0.1791948
K21417	uninjured	0.781271251	0.170733991	0.001811585	0.1791948
K02521	uninjured	0.648532574	0.143262607	0.001932299	0.1803479
K14571	uninjured	-3.737408031	0.839388448	0.002132098	0.184363794
K18313	uninjured	2.759115079	0.613740566	0.002013849	0.184363794
K18783	uninjured	2.99123803	0.670921819	0.002115554	0.184363794
K21337	uninjured	-2.011544986	0.449045834	0.00205689	0.184363794
K22074	uninjured	-0.748056628	0.167494025	0.002093846	0.184363794
K08225	uninjured	-1.334846097	0.302011838	0.002226947	0.189774627
K00974	uninjured	-0.165484515	0.038093379	0.002464487	0.204101165
K03779	uninjured	-2.135709113	0.490594781	0.002434438	0.204101165
K01813	uninjured	-0.348369622	0.080540369	0.002527587	0.206419624

K01692	uninjured	0.939611117	0.218131679	0.002589242	0.208558093
K06908	uninjured	-0.735016601	0.173379319	0.002839961	0.219221754
K09834	uninjured	-1.592246372	0.375411387	0.002832315	0.219221754
K13311	uninjured	-3.648063211	0.857519137	0.002783201	0.219221754
K13713	uninjured	2.937818135	0.694284829	0.002870761	0.219221754
K15652	uninjured	1.163649574	0.275882486	0.002924114	0.220433234
K00627	uninjured	0.571405453	0.136914498	0.003107385	0.228071581
K01208	uninjured	-0.64162342	0.15655913	0.003445929	0.228071581
K01463	uninjured	-0.472102801	0.114847182	0.003387342	0.228071581
K01483	uninjured	-1.297352431	0.31204497	0.003175739	0.228071581
K01905	uninjured	-0.921032127	0.222294328	0.003238654	0.228071581
K02190	uninjured	0.564798836	0.137467792	0.003397236	0.228071581
K03639	uninjured	-0.497350284	0.120495914	0.003309701	0.228071581
K08851	uninjured	-4.938325001	1.188811027	0.003191378	0.228071581
K09946	uninjured	-1.010490973	0.246642542	0.003452104	0.228071581
K20862	uninjured	4.608895476	1.11669006	0.003310821	0.228071581
K20881	uninjured	-3.793011334	0.908281706	0.003096411	0.228071581
K20791	uninjured	-0.945385971	0.233497547	0.003690331	0.241101593
K00382	uninjured	0.572481265	0.14236571	0.003834733	0.242856991
K00883	uninjured	0.949916382	0.237393713	0.003941851	0.242856991
K01897	uninjured	0.286104985	0.071888552	0.004062602	0.242856991
K07714	uninjured	-0.480460403	0.120420968	0.00400621	0.242856991
K09512	uninjured	-3.378514543	0.841086992	0.003858085	0.242856991
K11635	uninjured	0.602953968	0.151409021	0.004048735	0.242856991
K15983	uninjured	-1.675556714	0.418130127	0.003909961	0.242856991
K19303	uninjured	-2.783816809	0.700291624	0.004088919	0.242856991
K20025	uninjured	1.097421192	0.272300625	0.003787096	0.242856991
K05876	uninjured	2.858563588	0.724928994	0.004276442	0.244130863
K07798	uninjured	-0.709362432	0.179271174	0.004195083	0.244130863
K15770	uninjured	-0.200246199	0.050752385	0.004262538	0.244130863
K19666	uninjured	3.81244028	0.965308557	0.004239273	0.244130863
K01729	uninjured	-5.03673568	1.279585967	0.004318749	0.24417542
K16027	uninjured	-1.01154212	0.257628932	0.004379084	0.245228693
K00571	uninjured	-0.327857262	0.084593927	0.004703552	0.245667815
K04940	uninjured	0.647463988	0.166605993	0.004634032	0.245667815
K05618	uninjured	0.92018034	0.237646104	0.004727542	0.245667815
K12369	uninjured	-6.391279695	1.652585532	0.00475853	0.245667815
K15772	uninjured	-0.371170337	0.09538218	0.00460012	0.245667815
K16437	uninjured	2.505833065	0.64256678	0.004546423	0.245667815

K19068	uninjured	0.274425495	0.070818592	0.004707616	0.245667815
K21053	uninjured	3.144227339	0.807062493	0.00457107	0.245667815
K21902	uninjured	-0.585882731	0.151516687	0.004762947	0.245667815

Table 3. Significantly expressed PFAMs from metatranscriptomic analysis of the gut microbiome. PFAMs expression was determined, with the top 30 PFAMS shown in the table. Values that are increased in the injured cohort are in red. Qval is set at .25 as standard by Maaslin2 output.

Feature	value	coef	stderr	pval	qval
PF08859	uninjured	-2.9070828	0.30189051	1.12E-05	0.0255386
PF12811	uninjured	-7.0818845	0.70588068	8.28E-06	0.0255386
PF05128	uninjured	-4.5949458	0.51045444	1.85E-05	0.02802399
PF07581	uninjured	-2.8181788	0.39066221	9.12E-05	0.09668844
PF12961	uninjured	-4.0757245	0.57753361	0.00010641	0.09668844
PF02469	uninjured	3.67107738	0.56862299	0.00019704	0.11189235
PF15534	uninjured	1.80331404	0.27040533	0.00015769	0.11189235
PF17161	uninjured	2.74926783	0.424801	0.00019377	0.11189235
PF05709	uninjured	1.99776363	0.32495073	0.00027463	0.13862624
PF16861	uninjured	-0.9953344	0.16652924	0.00033182	0.15074783
PF13895	uninjured	6.02990902	1.02605094	0.00037134	0.15336205
PF00544	uninjured	-2.424991	0.46383738	0.0007947	0.17227499
PF00565	uninjured	-4.2487997	0.80874692	0.0007705	0.17227499
PF03894	uninjured	-2.1698807	0.41446946	0.00078776	0.17227499
PF06107	uninjured	0.44045225	0.07990405	0.00056551	0.17227499
PF06197	uninjured	-3.5242154	0.67330362	0.00078882	0.17227499
PF06280	uninjured	-2.3356751	0.44811105	0.00081018	0.17227499
PF09363	uninjured	-2.2011269	0.42416236	0.00083317	0.17227499
PF09364	uninjured	-2.1938482	0.42284684	0.00083426	0.17227499
PF09684	uninjured	-2.073049	0.37722304	0.00057676	0.17227499
PF11655	uninjured	2.46886423	0.43420787	0.00046183	0.17227499
PF16404	uninjured	-2.1197552	0.40811632	0.00082845	0.17227499
PF09682	uninjured	1.03433722	0.20131202	0.00088733	0.17526747
PF05270	uninjured	4.98527328	0.99759378	0.00105639	0.19996511
PF09956	uninjured	-2.2426219	0.45968639	0.00122655	0.22288778
PF00047	uninjured	4.16757271	0.88198408	0.00149208	0.24448698
PF01823	uninjured	-4.7925895	1.0268417	0.00160812	0.24448698
PF14195	uninjured	-1.4442051	0.30963188	0.00161449	0.24448698
PF14681	uninjured	0.25217304	0.05404647	0.00161116	0.24448698
PF17133	uninjured	3.20083009	0.68326818	0.00157251	0.24448698

Table 4. The top 30 COGs identified by metatranscriptomic analysis of the gut microbiome. COG expression was determined utilizing SqueezeMeta. Red rows indicate COGs that are increased in injured animals. A qval was utilized with all values below .25 significant as standard with Maaslin2 output.

feature	metadata	value	coef	stderr	pval	qval
ENOG410XVFE	Procedure	uninjured	5.53082243	0.41399743	9.43E-07	0.01489691
ENOG410ZMBG	Procedure	uninjured	1.32451553	0.12049871	4.17E-06	0.02197872
ENOG410ZYBE	Procedure	uninjured	7.43945085	0.65347742	3.20E-06	0.02197872
ENOG410YTB4	Procedure	uninjured	1.16637709	0.11935268	1.01E-05	0.0318517
ENOG410Z0I0	Procedure	uninjured	-7.0807918	0.70775489	8.46E-06	0.0318517
ENOG410Y5TQ	Procedure	uninjured	-3.2048318	0.35061529	1.65E-05	0.03732908
ENOG410ZJPN	Procedure	uninjured	4.58259192	0.49873217	1.59E-05	0.03732908
ENOG4111IKD	Procedure	uninjured	-2.4773703	0.27967582	2.08E-05	0.04114501
ENOG410YYU0	Procedure	uninjured	-8.2454475	0.97896477	3.01E-05	0.04266895
ENOG4111CSG	Procedure	uninjured	3.51737669	0.42187862	3.24E-05	0.04266895
ENOG4111SRE	Procedure	uninjured	-4.4689722	0.53067874	3.01E-05	0.04266895
ENOG4112ANZ	Procedure	uninjured	8.14643816	0.97175624	3.11E-05	0.04266895
ENOG411258X	Procedure	uninjured	-2.4843318	0.3124558	4.56E-05	0.05549038
ENOG410XZQE	Procedure	uninjured	4.32907205	0.56120253	5.67E-05	0.06401097
ENOG410ZA8C	Procedure	uninjured	-4.3044656	0.57101605	6.68E-05	0.07040354
ENOG410XWEA	Procedure	uninjured	3.03022323	0.41157875	7.90E-05	0.07343649
ENOG41121TV	Procedure	uninjured	-1.4935044	0.20188413	7.64E-05	0.07343649
ENOG410Z56V	Procedure	uninjured	7.61227078	1.04872885	8.73E-05	0.07667518
ENOG410ZJBM	Procedure	uninjured	3.4819786	0.49644055	0.00011109	0.09240854
COG3948	Procedure	uninjured	-2.2351494	0.32228794	0.00012018	0.09352033
ENOG410YA2Z	Procedure	uninjured	-3.0379667	0.4401485	0.00012426	0.09352033
COG4683	Procedure	uninjured	2.42254718	0.36347724	0.00015834	0.10010326
ENOG4110V8B	Procedure	uninjured	-8.7700378	1.29302064	0.00014029	0.10010326
ENOG4111RCH	Procedure	uninjured	-5.4562026	0.81754137	0.00015687	0.10010326
ENOG4111VYZ	Procedure	uninjured	2.67673902	0.39855693	0.0001502	0.10010326
ENOG410ZEV8	Procedure	uninjured	2.27911641	0.35304035	0.00019712	0.10942613
ENOG410ZI6N	Procedure	uninjured	-6.4825741	0.99931962	0.0001907	0.10942613
ENOG4111IE7	Procedure	uninjured	-2.3181724	0.36005847	0.00020078	0.10942613
ENOG41121TR	Procedure	uninjured	2.88045633	0.44207693	0.00018501	0.10942613

Table 5. Top 25 gene ontologies altered in the colon of animals with PTOA.
DEGS were analyzed to identify enriched GO terms. padj of <.05 were considered significant

Description	pvalue	padj
lipid biosynthetic process	8.04E-11	4.30E-07
sterol biosynthetic process	1.90E-08	5.07E-05
cholesterol biosynthetic process	4.61E-08	8.22E-05
steroid biosynthetic process	7.68E-08	0.00010261
secondary alcohol biosynthetic process	9.93E-08	0.00010615
fatty acid metabolic process	1.45E-06	0.00128587
steroid metabolic process	1.68E-06	0.00128587
extracellular structure organization	2.45E-06	0.00157473
carboxylic acid biosynthetic process	2.69E-06	0.00157473
organic acid biosynthetic process	2.95E-06	0.00157473
cholesterol transport	5.35E-06	0.00244735
positive regulation of lipid metabolic process	5.49E-06	0.00244735
sterol transport	6.64E-06	0.00273137
organic hydroxy compound biosynthetic process	1.23E-05	0.0047075
angiogenesis	1.59E-05	0.00534497
phagocytosis, engulfment	1.60E-05	0.00534497
regulation of lipid biosynthetic process	2.16E-05	0.00679308
ossification	2.71E-05	0.00805342
BMP signaling pathway	3.19E-05	0.00859798
positive regulation of lipid biosynthetic process	3.22E-05	0.00859798
regulation of telomere maintenance	4.59E-05	0.01102779
fatty acid biosynthetic process	4.69E-05	0.01102779
phagocytosis	4.74E-05	0.01102779
anatomical structure homeostasis	5.02E-05	0.01118522
cholesterol metabolic process	5.27E-05	0.01126166

10. Appendix 2: Hendesi et al, Manuscript Draft

Mitigation of Posttraumatic Osteoarthritis via Dietary Supplementation with Hydrolyzed Hyaline Cartilage is Associated with Anti-inflammatory Shifts in the Gut Microbiome

Honey Hendesi*[,1], Sara Soniwala*[,2], Eric Schott[3], David A. Villani[4], Qurratul-Ain Dar[5], Ana Ferreira Ruble[1], Andrew Wu[6], Ann Gill[7], Samantha H. Landgrave[4], Lacey J. Favazzo[1], Manja Zec[1], Steven R Gill[7], Janne Prawitt[8], Michael Zuscik[1]

[1]Colorado Program for Musculoskeletal Research, Department of Orthopedics, University of Colorado Anschutz Medical Campus, Aurora, CO, USA

[2]UPMC – information needed

[3]Solarea Bio, Cambridge, MA, USA

[4]Cell Biology, Stems Cells and Development Program, Anschutz Medical Campus, University of Colorado, Aurora, CO, USA

[5]Thomas Jefferson – information needed

[6]Johns Hopkins University – information needed

[7]Department of Microbiology and Immunology, University of Rochester Medical Center, Rochester, NY, United States.

[8]Rousselot BVBA, Gent, Belgium

Corresponding Author:
Michael J. Zuscik
MICHAEL.ZUSCIK@CUANSCHUTZ.EDU

INTRODUCTION

Osteoarthritis (OA) is a progressive joint degenerative disease of cartilage, synovium, and subchondral bone tissues. As one of the leading causes of disability, OA impacts approximately 500 million individuals worldwide (Ref). Because of the multifactorial etiology (i.e., age, injury, genetics, sex, and obesity) and the heterogeneity in the severity of symptoms and progression speed, developing a disease-modifying OA drug (DMOAD) has remained a significant unmet need (Ref). Currently, medical intervention in OA patients is limited to symptom-mitigating palliative care and, eventually, joint replacement surgeries (Ref). Considering the debilitating nature of OA and the absence of an accepted DMOAD, dietary interventions that can potentially decelerate the progression, alleviate symptoms, and improve patients' quality of life, are highly desirable and in need of further investigation.

Nutraceuticals, including various preparations of cartilage structural molecules, have been advertised as joint health supplements with potential benefits for OA patients. Dietary supplements like glucosamine, chondroitin sulfate, and undenatured type II collagen have shaped a multibillion-dollar industry in the United States (Ref). Despite the variable reported efficacy of these products, which has largely precluded them from inclusion in clinically accepted treatment guidelines, it is common for OA patients to use these supplements in combination with prescription and over-the-counter medications (Ref).

Type II collagen (Col2) is the most abundant protein component of articular cartilage (Ref), and preparations of Col2 are reported to have the potential as a dietary intervention to support joint health. A randomized clinical trial by Trentham et al. was the first to provide evidence that Col2 consumption reduces flares in rheumatoid arthritis patients (Trentham et al., 1993). Without information about potential underlying mechanisms of action, clinical and animal studies continued to provide support for OA protective effects of Col2. These clinical studies have relied primarily on patient-reported outcomes such as Western Ontario and McMaster

Universities Osteoarthritis Index (WOMAC) and Visual Analogue Scale (VAS) to evaluate nutraceuticals' effectiveness (ref). Multiple clinical studies ranging from 90 days to 6 months have reported improvement in WOMAC and VAS scores in OA patients supplementing their diet with Col2 (ref). These studies have claimed that Col2 is superior to other commonly used nutraceuticals (i.e., chondroitin sulfate and glucosamine) in mitigating OA symptoms (Ref), however more data are needed to corroborate these findings.

Although cartilage-derived dietary supplements can alleviate joint pain in various contexts (Refs), the molecular basis of their action is not determined. Complex first-pass metabolism, variable absorption levels and broad systemic distribution leave open questions about the portion of supplement metabolic fractions that reach the joint and their underlying mechanism(s) of action undetermined (Ref). We and others have recently proposed that shifts in the gut microbiome caused by metabolic breakdown products of consumed supplements with prebiotic effects might mechanistically underlie their biological effects in the host (Refs). It is now understood that the microbial community members comprising the gut microbiome, composed of the whole microbial ecosystem within the gastrointestinal tract, can utilize various breakdown products from consumed nutraceuticals as a source of metabolic energy (Ref). Moreover, it is now accepted that shifts in abundance of the individual gut microbial taxa, which lead to host-impacting functional changes, can alter the course of diseases with underlying inflammatory and metabolic dysregulations, including Alzheimer’s disease (Ref), Parkinson’s (Ref), IBD, Crohn’s Disease (Ref), rheumatoid arthritis (Ref), osteoporosis (Ref), Type 2 Diabetes (Ref), metabolic syndrome (Ref), and notably OA (Refs), with several studies identifying a its potential role in OA progression. These studies found a correlation between WOMAC score and lipopolysaccharides (LPS) serum levels, a pro-inflammatory microbiome metabolite. Moreover, pre- or probiotic interventions have shown the ability to decelerate OA progression via inflammation-suppressing pathways (Refs), suggesting that targeting the gut

microbiome may be an effective symptom-mitigating and disease modifying strategy for the treatment of OA.

The mechanistic basis for cartilage-derived nutraceutical effects in any context, particularly in joint health, are unknown. Therefore, in the present study, using a mouse model of surgery-induced posttraumatic OA (PTOA), we investigated the impact of hydrolyzed hyaline cartilage (hHC), a nutraceutical mainly composed of Col2 and proteoglycans, on PTOA progression. First, we assessed short-term and long-term degenerative changes and inflammatory and apoptotic responses in the articular cartilage. In addition, we evaluated hHC-induced shifts in gut microbiome composition to identify changes that might be expected to suppress inflammation in the host, and thus reduce inflammation in joints. In aggregate, we document that hHC supports chondroprotective effects in PTOA that are associated with changes in the gut microbiome, providing a rationale for future work aimed at the study of key microbial taxa and the moleculaes they produce as mechanistically linked to the joint protective effects of various nutraceutical interventions.

MATERIALS AND METHODS

Animals and Diet: The experimental procedures performed in this study were reviewed and approved by the University of Rochester IACUC (University Committee on Animal Resources). Six week old C57BL/6J male mice were purchased from Jackson laboratory and were single-housed in ventilated cages in a room with a 12-hour light/dark schedule. Six week old mice were fed a defined diet (Open-Source Diets, D12450B, 10% kCal from fat) *ad libitum*. After eight weeks on this diet, mice (now 14 weeks of age), were provided daily supplementation with 0.62mg/g body weight hHC incorporated into 120 µL hazelnut cream (or hazelnut cream alone as a negative control) as we have previously done (Ref). hHC is a preparation of porcine tracheal cartilage comprised of Col2 peptides, proteoglycans, and other endogenous cartilage matrix components produced by Rousselot BVBA. After 4 weeks of supplementation, mice (now 18 weeks old) were administered DMM surgery to induce PTOA. We continued hHC supplementation until harvest time points at 3 weeks or 12 weeks post-DMM. Mice were euthanized using an American Veterinary Medical Association-approved (AMVA-approved) method.

Destabilization of the Medial Meniscus: PTOA was surgically induced in 18 weeks old mice via destabilization of the medial meniscus (DMM) (10, 11) as we have previously performed (Ref). In brief, mice were anesthetized via i.p. injection of 60 mg/kg ketamine (Ketalar, Par Pharmaceutical Inc.) and 4 mg/kg xylazine (AnaSed, Akorn Animal Health). Briefly, a 5mm skin incision was made on the medial aspect of the knee. Under a dissecting microscope, an deeper incision was made along the medial side of the patellar tendon, opening the joint space. Using a #11 scalpel, the medial meniscotibial ligament (MMTL) was transected, releasing the medial meniscus to move freely. After surgery, 4-0 silk sutures were used to close the incision using an interrupted pattern. Mice were provided analgesia via i.p. injection of buprenorphine (0.5 mg/kg) every 12 hours for 72 hours, and sutures were removed after seven

days. After 3 or 12 weeks post-DMM mice were euthanized via induction of CO_2 narcosis followed by cervical dislocation.

Tissue Sample Preparation: After euthanizing mice at 3 or 12 weeks post-DMM, the knee joints were dissected with the femur and tibia intact to maintain knee joint structure. Tissues were fixed in 4% paraformaldehyde at 4°C for 72 hours, decalcified in 5% formic acid for ten days, processed using a microwave processor, and embedded in paraffin. Tissue blocks were then serially sectioned in the midsagittal plane through the medial compartment of the joint. A series of 5μm thick sections were cut at three distinct levels within the medial compartment, mounted on positively-charged glass slides, and stored for histology, immunohistochemistry, and TUNEL assay. For the histomorphometric study of cartilage tissue, the embedded slides were baked at 60 degrees C overnight, de-paraffinized in xylene, rehydrated with ethanol in descending concentration, and stained with 0.1 Fast Green stain and 0.08% Safranin-O (Saf-O) stain as we have previously performed (Ref).

Histomorphometric Analysis: Femur and tibia articular cartilage area and the number of Saf-O-positive articular chondrocytes were quantified by a blinded observer using OsteoMetrics as previously described (9, 10). Briefly, Saf-O/Fast-Green stained sections were individually viewed using an Olympus DP74 light microscope interfaced with the OsteoMetrics System via a digital camera, and images were obtained at 400x magnification. The OsteoMetrics stylus pen was used to outline projected images and mark cells. For each specimen, measurements were taken from one slide at the three levels (50μm apart) on the tibial plateau and femoral condyle in a 200μm-wide area of interest centered on the joint. OsteoMeasure 64 V1.0.3.0 software was used to determine femur and tibia uncalcified cartilage area, calcified cartilage area, and chondrocyte number including total cells and Saf-O-positive cells. These quantified parameters were averaged across the three levels for each specimen. We normalized data to the same architectural assessments collected from sham knees.

Immunohistochemistry: For TNF-α IHC, paraffin-embedded slides were baked overnight at 60°C and rehydrated stepwise in descending concentrations of ethanol. Endogenous peroxidases were quenched with BLOXALL (Vector, CAT #) for 10 min at room temperature, followed by a 30 min treatment with normal horse serum for blocking. Slides were incubated overnight at 4°C with a rabbit anti-mouse TNF-α polyclonal antibody (1:200; Abcam catalog #ab6671) or PBS for negative control. For TNF-α detection, slides were then rinsed with PBS containing 0.5% Tween-20 and incubated for 30 minutes at room temperature with Rabbit IgG Polymer secondary antibody (Vector ImmPress Rabbit Polymer Detection Kit, MP-7401). Antibody binding to TNF-α was detected after applying DAB Immpact solution (Vector, SK-4105) for 2 minutes. Nuclei were counterstained for 15 seconds with Mayer's Hematoxylin (Sigma-Aldrich, CAT #). The slides were dehydrated and preserved with Cytoseal (Fisher Scientific, catalog #23-244257). Immunostained slides were then independently graded by three expert observers blinded to treatment groups to gauge intensity of TNF-α staining. In brief, staining intensity was graded in the synovial membrane at the knee's anterior and distal junction to the tibia plateau, an area nearest to the injured meniscotibial ligament. Staining intensity was graded as 0, 1, 2, or 3 by each observer separately, with 0 representing background-equivalent staining and 3 the strongest intensity staining. This scale was modified from an existing publication (13).

TUNEL Assay: To assess chondrocyte apoptosis in histology sections of joint tissue, the Click-iT Plus TUNEL Assay for In Situ Apoptosis Detection kit was used following manufacturer’s protocol (Invitrogen, # C10617). Hoescht counterstain (Invitrogen, # H3570) was used to detect nuclei. Fluorescent images of the slides were captured using a Photometrics CoolSNAP DYNO equipped Nikon Eclipse 80i microscope. The number of apoptotic nuclei were counted and fluorescence staining intensity was determined using ImageJ (14).

16S rRNA Sequencing: Freshly produced fecal pellets were harvested from mice after scruffing and immediately frozen at -80°C. DNA was extracted using the ZR Fecal DNA Extraction Kit (Zymo Research, CAT#) as directed by the manufacturer. 16S ribosomal DNA (rDNA) was amplified with Phusion High-Fidelity polymerase (Thermo Fisher Scientific) using dual indexed primers specific to the V3-V4 hypervariable regions (319F: 5′ ACTCCTACGGGAGGCAGCAG 3′; 806R: 3′ ACTCCTACGGGAGGCAGCAG 5′). Amplicons were pooled and paired-end sequenced on an Illumina MiSeq (Illumina) in the University of Rochester Genomics Research Center. Each sequencing run included positive controls consisting of a 1:5 mixture of *Staphylococcus aureus, Lactococcus lactis, Porphyromonas gingivalis, Streptococcus mutans*, and *Escherichia coli*, and negative controls consisting of sterile saline. Raw data from the Illumina MiSeq was first converted into FASTQ format using the bcl2fastq program, version 1.8.4, provided by Illumina. Format conversion was performed without demultiplexing, and the Extended Adaptive Multi-mode Search (EAMMS) algorithm was disabled. All other settings were default. Sequence processing and microbial composition analysis were performed with the Quantitative Insights into Microbial Ecology (QIIME) software package (73), version 1.9.1. Reads were multiplexed using a configuration described previously (74). Briefly, for both reads in a pair, the first 12 bases were a barcode, which was followed by a primer, then a heterogeneity spacer, and then the target 16S rRNA sequence. Using a custom Python script, the barcodes from each read pair were removed, concatenated together, and stored in a separate file. Read pairs were assembled using fastq-join from the ea-utils package, requiring at least 40 bases of overlap and allowing a maximum of 10% mismatched bases. Read pairs that could not be assembled were discarded. The concatenated barcode sequences were prepended to the corresponding assembled reads, and the resulting sequences were converted from FASTQ to FASTA and QUAL files for QIIME analysis. Barcodes, forward primer, spacer, and reverse primer sequences were removed during demultiplexing. Reads containing more than 4 mismatches to the known primer sequences or more than 3 mismatches to all

barcode sequences were excluded from subsequent processing and analysis. Assembled reads were truncated at the beginning of the first 30-base window with a mean Phred quality score of less than 20 or at the first ambiguous base, whichever came first. Resulting sequences shorter than 300 bases or containing a homopolymer longer than 6 bases were discarded. Operational taxonomic units (OTUs) were picked using the reference-based USEARCH (version 5.2) (75) pipeline in QIIME, using the May 2013 release of the GreenGenes 99% OTU database as a closed reference (76, 77). An indexed word length of 128 and otherwise default parameters were used with USEARCH. Chimera detection was performed *de novo* with UCHIME, using default parameters (75). OTU clusters with fewer than four sequences were removed, and representative sequences used to make taxonomic assignments for each cluster were selected based on abundance. The RDP Naive Bayesian Classifier was used for taxonomic classification with the GreenGenes reference database, using a minimum confidence threshold of 0.85 and otherwise default parameters (78).

Statistical Analysis: For histology-based outcome measures, cell numbers, and cartilage areas (after normalizing to cartilage area of sham controls), for IHC immunograding, and for Tunnel assays, we conducted unpaired two-tailed student t-tests. All analyses and graphing of the data were carried out using GraphPad Prism software (version 10.0.0). Differences between groups were considered significant when $p<0.05$ was achieved.

RESULTS

Oral hHC supplementation delays cartilage loss in mid to late stage PTOA: To examine the impact of hHC supplementation on joint architecture in PTOA, mice provided daily hHC or vehicle control to their diet were administered DMM injury, and joint tissues were assessed histologically 3 and 12 weeks later. Although cartilage areas on the femur and tibia in hHC supplemented and control mice were similar 3 weeks post-DMM, and overall cartilage matric architecture was similar between the groups as well, there was evidence of increased % of Safranin O-positive chondrocytes in the femoral articular cartilage in the supplemented group (Fig. 1A-C, I).

posttraumatic cartilage degeneration, mice were euthanized three weeks after DMM surgery. The DMM-operated and contralateral sham knees were collected, processed, sectioned, and stained with Safranin O/Fast Green for histology evaluation. The cartilage and chondrocyte morphology in DMM-operated and contralateral sham knees upon 3 weeks of hHC post-DMM administration is presented in Figure 1, A-C. Given that cartilage degradation and reduced proteoglycan production are hallmarks of osteoarthritis, we measured the area of calcified and uncalcified cartilage and the number of total and Safranin O positive chondrocytes in both tibia plateau and femoral condyle The area of calcified and uncalcified cartilage and the number of total and Safranin O positive chondrocytes in both tibia plateau and femoral condyle are presented in Figure 1. D-O. We detected a significantly higher ($p<0.01$) percentage of Safranin O positive chondrocytes in the femoral cartilage of mice supplemented with hHC than in the vehicle control mice (Figure 1. I). In the tibia, we measured a borderline significant ($p=0.06$) larger calcified cartilage area (Figure 1. L). These results suggest that hHC can preserve the health of chondrocytes and possibly decelerate degenerative cartilage changes early after trauma.

The long-term impact of hydrolyzed cartilage on cartilage degradation and matrix production

The impact of long-term hHC supplementation on the progress of arthritis, in DMM and sham-operated knees twelve weeks after the surgery is presented in Figure 2. The advanced loss of proteoglycans and cartilage degradation were notable in the vehicle cohort mice (Figure 2, B). Remarkably, histomorphometric evaluation showed that except for the total and calcified femoral cartilage area (Figure 2, D and F), all histomorphometrics were superior in the hHC-supplemented mice ($p<0.05$) when compared to the control (Figure 2, D-O). Our results suggest that long time daily ingestion of the hHC can significantly protect against posttraumatic arthritic changes in cartilage.

The impact of hydrolyzed cartilage on local inflammation

Joint inflammation following trauma can positively predict the progress of cartilage degeneration (Ref). Tumor Necrosis Factor Alpha (TNF-α) is one of the major inflammatory cytokines involved in the advancement of OA that can be produced by chondrocytes, synoviocytes, mononuclear cells, and osteoblasts (Ref). TNF-α suppresses the synthesis of proteoglycans and type II collagen by chondrocytes, and increases the synthesis of matrix metalloproteases (MMP1, MMP3, MMP13) and ADAMTS-4, also enhancing chondrocyte apoptosis (Ref). To examine the expression of TNF-α in knee joints of hHC and control mice, we performed immunohistochemistry staining at three and twelve weeks post-DMM and graded a region that the DMM primarily impacted for the intensity of the stain (Figure 3). The hHC supplementation induced no differences in TNF-α upon 3 weeks, however, at 12 weeks post-DMM, we detected a borderline significant ($p<0.055$) decrease in TNF-α expression (Figure 3, C

and D). This finding suggests that hHC can damper the inflammatory response to trauma, and its anti-inflammatory effect is persistent later when OA is well progressed.

The impact of hydrolyzed cartilage on chondrocytes apoptosis

The health of cartilage tissue is highly dependent on the health and function of its only resident cells, chondrocytes. Therefore, the death of chondrocytes can lead to the failure of the cartilage tissue. What we see in the histology of the arthritic cartilage in the form of empty lacuna and hypocellularity are indications of apoptosis of chondrocytes that, in early stages, can be detected by visualizing fragmented DNA.

Multiple factors, such as proinflammatory cytokines, NOS, and mechanical stress, can contribute to chondrocyte apoptosis in arthritic cartilage. Although it is not yet clear whether chondrocyte apoptosis is the primary cause of cartilage damage or itself is a consequence of cartilage matrix degradation, a positive correlation between chondrocyte apoptosis and OA progression is well accepted (Ref).

To evaluate chondrocytes' apoptosis following the DMM, we did a TUNEL assay to visualize the DNA fragmentation at three and twelve weeks post-DMM (Figure 4). At three weeks' timepoint, we detected a significantly lower ($p<0.001$) number of the TUNEL positive cells in hHC-supplemented mice compared to the control mice (Figure 4, A, and C). Although, as expected, the overall number of TUNEL-positive cells increased by twelve weeks, we did not detect a significant difference in the number of cells between hHC and control cohorts (Figure 4. B and C). This finding suggests that the early protection against apoptosis by hHC may have resulted in lower long-term cartilage loss in supplemented mice.

The impact of hydrolyzed cartilage on gut microbiota composition

To characterize the effect of hHC supplementation on gut microbiota composition, we performed 16s rRNA sequencing on fecal samples of hHC and control mice at three and twelve weeks timepoints. Principle coordinate Analysis (PCoA) of microbial community based on Bray-Curtis dissimilarity (Beta-Diversity) identified two distinct clusters with significant separation (PERMENOVA, $p=0.023$; Fig 5. A). Next, we explored each mouse's percentage abundance of different phyla (Figure 5. B). Although we did not detect a difference in the alpha-diversity (distribution of taxa abundances in each mouse) of hHC and control groups (data not shown), the difference in microbial composition between the two cohorts was noticeable (Figure 5. B). At the phylum level, we observed an increase in Firmicutes and Tenericutes at the expense of a decrease in Actinobacteria and Bacteroides in hHC mice (Fig 5. B). However, the differences did not gain statistical significance when we averaged the phyla abundance percentages from each treatment group (Figure 5. C). A deeper analysis of taxa abundances revealed a significant increase in not-defined genera in the family of *Ruminococcaceae* ($p<0.05$), an important butyrate producing bacteria (Ref), in hHC group. Total loss of rc4-4 ($p<0.0001$), recognized for its pro-inflammatory properties (Ref), was another notable finding in hHC mice. In addition, we observed a decreased in *Dehalobacterium* ($p<0.05$) and *Akkermensia* (*Akkermensia muciniphila sp.*) ($p<0.05$) in the hHC cohort (Figure 5. D). An increase in the only species of Tenericutes phylum, *anaeroplasma sp.,* in the hHC group was not statistically significant ($p=0.1$, data not shown).

Overall, our microbiome sequencing data revealed a dissimilarity in microbial composition of two treatment groups. A distinct decline in the population of pro-inflammatory *rc4-4* and an increase in butyrate producing *Ruminococcaceae* in hHC mice can be contributing factors to the slower progress of OA in supplemented mice (Figure 5).

DISCUSSION

We used a commonly used posttraumatic OA model in non-obese mice on a defined diet to examine the impact of hHC on the progress of OA and recognize shifts in gut microbiome with joint health implications. hHC supplement is a mixture of hydrolyzed type II collagen with low molecular weight and different high molecular weight proteoglycans. Because of the unique profile of hHC, we expected to detect distinctive changes in the gut microbiome and cartilage tissue, and our results demonstrate…

Despite OA being a global health issue, no effective pharmacological treatment has been developed for it to date. Because of OA's progressive and debilitating nature, many patients consume dietary supplements and nutraceuticals, including collagen, glucosamine, and chondroitin sulfate, in addition to prescribed palliative drugs to manage their symptoms. Although several clinical studies using patient-reported outcomes have claimed that nutraceuticals can improve symptoms of OA, their mechanism of effect and whether they can impact the course of the disease stays speculative.

Collagen supplements are by-products of the food industry. Different formulations of collagen are produced with undenatured and hydrolyzed forms being the most common types. Undenatured type II collagen (UC-II) is a patented glycosylated collagen often derived from chicken cartilage (Ref). In comparison, hydrolyzed collagen is denatured and hydrolyzed native collagen broken into small fragments to increase its bioavailability (Ref). Processing collagen and its hydrolysates may result in formulations with differing peptide and amino acid profiles, affecting patient outcomes (Schadow et al.). This lack of product standardization has been a major challenge for research and the healthcare community.

Following Trentham et al. study that showed Collagen type II reduces RA flares, clinical and animal studies continued supporting OA protective effects of type II collagen. A study on a rat model of posttraumatic osteoarthritis (PTOA) showed that oral type II collagen supplements

reduce cartilage degeneration and improve weight bearing (Bagi et al.). Deparle et al. supplemented obese arthritic dogs with type II collagen and witnessed a symptom-mitigating effect (Ref). Clinical studies using patient-reported outcomes have declared daily oral consumption of collagen supplements safe (Ref). A multicenter study of 191 OA patients showed improved WOMAC scores following six months of undenatured type II collagen consumption (Lugo et al.,2016). Another study on 110 OA patients showed 12 weeks of consumption of type II collagen resulted in improved WOMAC scores (Luo et al., 2022), and a study on 52 OA patients recognized that even 90 days of supplementation with type II collagen is sufficient to detect improvement in WOMAC scores (Crowley et al., 2009). The above-stated studies compared type II collagen's effect to chondroitin sulfate, and glucosamine (Bottegoni, Henroitin, Bruyers, Favazzo). Despite the beneficial impact of chondroitin sulfate and glucosamine, in all studies, type II collagen showed a more robust symptom-mitigating effects (Ref).

The beneficial effect of collagen supplements for arthritis is not limited to type II. Clinical and translational studies have established that type I collagen can be as effective. Using a mouse model of surgically induced PTOA, Dar et al. confirmed a cartilage protective effect for daily oral consumption of type I collagen (Ref). A randomized placebo-controlled trial on hundred women has reported a significant improvement in WOMAC scores of patients upon 6-months hydrolyzed collagen I supplementation (Jiang et al., 2014). Puegdellivol et al. used a mix of hydrolyzed gelatin, chondroitin sulfate, and glucosamine sulfate and reported an improved WOMAC and VAS after six months (Ref). Additionally, a 24-week clinical trial on 147 healthy athletes with activity-related joint pain showed improved joint discomfort and pain in walking, standing, lifting and carrying weight, running, and resting in athletes who were administered hydrolyzed collagen supplements (Ref). This study suggests the benefits of collagen supplementation in a joint disease free population.

In vitro studies have suggested that collagen peptides absorbed postprandially can potentially accumulate in cartilage and induce ECM synthesis by chondrocytes; however, whether these phenomena occur in vivo is not confirmed yet (REF). Low bioavailability of collagen and glycoproteins, variation in patients' response to nutraceuticals, and the impact of first-pass metabolism have turned attention toward the possible role of unabsorbed ingested peptides. Unabsorbed molecules reaching the colon might have probiotic effects, and the role of some taxa in the degradation of chondroitin sulfate in human gut is recognized (REF). Differences in individuals' gut microbiota may underscore the interpersonal variability in response in OA upon treatments with nutraceuticals.

Numerous studies investigated the gut microbiome's role in OA's progress in various OA models, e.g., obesity-induced OA, posttraumatic OA. Schott et al. used prebiotic oligofructose to reduce obesity dysbiosis and alleviate OA (Ref), elucidating possibly supportive role of *Bifidobacterium pseudolongum* in joint health. On the other hand, some gut community members (e.g., *Clostridiu*m) were recognized for their OA-inducing effect (Schott et al., Rios et al.). A clinical study showed a correlation between serum lipopolysaccharides (LPS), an inflammatory microbiome metabolite, with the WOMAC (Western Ontario and McMaster Universities Osteoarthritis) score and accumulation of macrophages in the joint of OA patients (Huang et al., 2016). Furthermore, Boer et al. used 16s sequencing data from Rotterdam Cohort participants and established a correlation between gut microbiome abundance of *Streptococcus* species and joint pain in OA patients (Boer et al., 2019). These studies support the notion that OA is a systemic disease with an inflammatory and metabolic undertone and not solely a localized joint illness.

Our knowledge of cartilage-derived supplements' impact on the gut microbiome is limited. In a study of PTOA in mice, Favazzo et al. investigated the progress of OA and shifts in the microbial community following supplementation with undenatured type II collagen or

glucosamine, demonstrating shifts in microbiome reflective of reduced inflammation (REF). Additionally, they observed lower cartilage degeneration in mice supplemented with both nutraceuticals (Ref). Our 16s data showed an increase in an undefined member of the *Ruminococcacea* family in supplemented mice. Previous studies have not established an association between *Ruminococcaceae* and OA. *Ruminococcaceae* plays an important role in maintaining gut health through its ability to produce butyrate and other SCFAs. Low abundance of *Ruminococcaceae* has been implicated in some inflammatory bowel diseases, including ulcerative colitis and Crohn's disease (Ref). Another detected shift was the total elimination of the *rc-4-4* genus of the *Peptococcaceae* family. The *rc4-4* is recognized for its pro-inflammatory effect in the context of different diseases (ref). Previous OA studies showed that prebiotics reduces *rc4-4* abundance, which protects cartilage from arthritic degradation (Ref). Furthermore, a low abundance of *Dehalobacterium* is associated with high BMI (fu et al., 2015), and in our study…. The overall limited knowledge about physiological roles of *Dehalobacterium* makes driving conclusions difficult. Furthermore, we detected a decrease in *Akkermensia mucinaphia* species. *Akkermensia mucinaphia* is a mucin digester and SCFA producer bacterium, regulating mucin thickness and gut barrier integrity (REF) and preventing a leaky gut conditions. Its declined levels are linked to diabetes, metabolic syndrome, and IBD (Ref). The established benefits associated with *A. muciniphila* have turned it into one of the commercially available prebiotic supplements (REF). The detected decrease in *A. muciniphila* in hHC-supplemented mice may be result of a dramatic shift in the source of energy in the gut from mucin to non-glycosylated proteins.

We acknowledge a few limitations in our study approach. Firstly, studying OA progression without exploring synovium and subchondral bone changes is incomplete. A holistic look into the impact of hHC on various joint compartments should assessed in the future studies. Furthermore, the 16S sequencing provides a limited view into the taxonomic

characterization of the gut microbiome with serious limitations in recognizing bacterial species. In future studies, multiomics approaches using metagenomics and metatranscriptomic analysis of gut microbiome will enable us to detect members of the commensal community with higher precision and recognize changes in their activity. Metabolomic analysis of fecal and serum samples will allow us to evaluate released microbial metabolites. Part of the observed changes in inflammation and apoptosis in the knee may be a direct effect of microbial metabolites that needs to be investigated. To establish a causal role for the gut microbiome in hHC-induced changes in cartilage, we will implement microbiome ablation and transplantation techniques in our future investigations and apply robust omics strategies. Finally, although mice provide a strong model for translational OA and microbiome studies, there are notable differences in human and mouse microbiome composition and joint anatomy. Uncovering the impact of hHC on the progress of OA, the causal role of the gut microbiome, and the extent of its influence on the course of OA development requires further investigation, which must include clinical studies.

REFERENCES

Under Development

Figure 1:

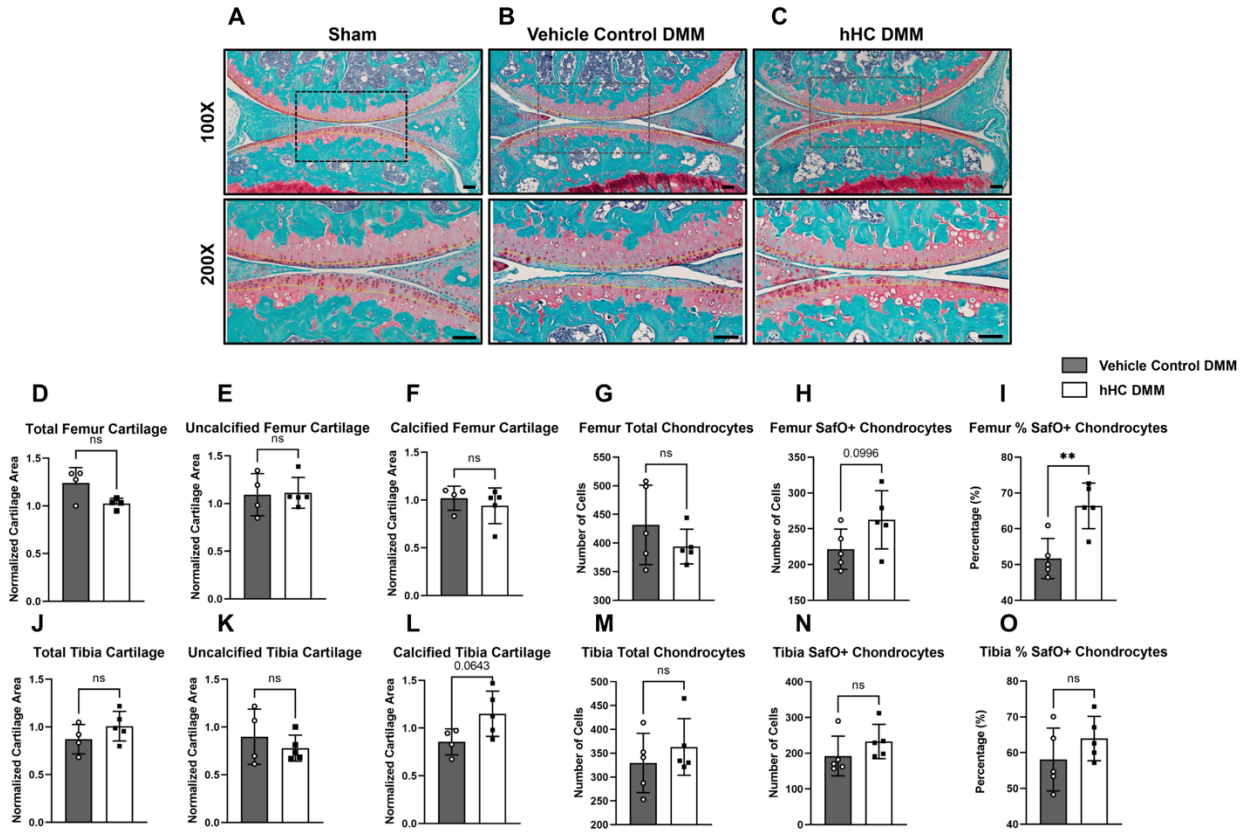

Figure 1. Three weeks of hydrolyzed hyaline cartilage have minimal effect on post-traumatic cartilage degeneration. A) Three weeks post-DMM representative images of Safranin O/Fast Green stained histology slides of sham and (B and C) DMM knee joint sections of mice that have received hHC supplementation (B) or control vehicle (C). The yellow dotted line separates calcified and uncalcified cartilage. Scale bar= x, D) Histomorphometric evaluation of Total area of femur cartilage comparing hHC mice to control mice. Data is normalized to numbers in sham knees and repeated for several metrics in femoral condyle cartilage: E) Area of uncalcified femur cartilage, F) Area of calcified femur cartilage, G)Total number of chondrocytes in femur, H) Number of Safranin O positive chondrocytes in femur, I) Percentage of Safranin O positive chondrocytes in femur, and the same metrics in tibia plateau cartilage: J) Total area of tibia cartilage, E) Area of uncalcified tibia cartilage, F) Area of calcified tibia cartilage, G)Total number of chondrocytes in tibia, H) Number Safranin O positive chondrocytes in tibia, I) Percentage of Safranin O positive chondrocytes in tibia. (n= 5). Significant differences between groups were identified by unpaired student t-test, error bar= SEM,** $p < 0.01$.

Figure 2:

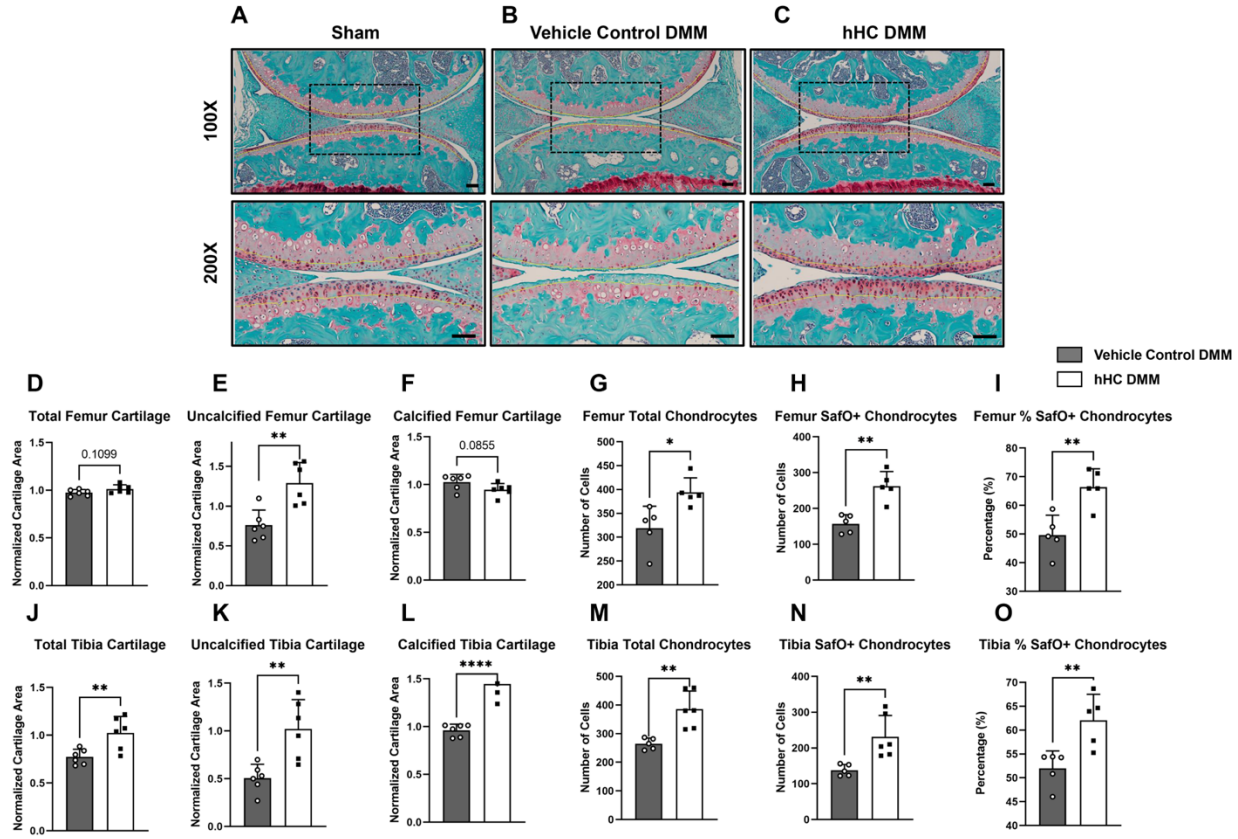

Figure 2. Twelve weeks of hydrolyzed hyaline cartilage supplementation significantly protects against post-traumatic arthritic changes. A) Twelve weeks post-DMM representative images of Safranin O/Fast Green stained histology slides of sham and (B and C) DMM knee joint sections of mice that have received hHC supplementation (B) or control vehicle (C). The yellow dotted line separates calcified and uncalcified cartilage. Scale bar= ?, D) Histomorphometric evaluation of Total area of femur cartilage comparing hHC mice to control mice. Data is normalized to numbers in sham knees and repeated for several metrics in femoral condyle cartilage: E) Area of uncalcified femur cartilage, F) Area of calcified femur cartilage, G)Total number of chondrocytes in femur, H) Number Safranin O positive chondrocytes in femur, I) Percentage of Safranin O positive chondrocytes in femur, and the same metrics in tibia plateau cartilage: J) Total area of tibia cartilage, E) Area of uncalcified tibia cartilage, F) Area of calcified tibia cartilage, G)Total number of chondrocytes in tibia, H) Number Safranin O positive chondrocytes in tibia, I) Percentage of Safranin O positive chondrocytes in tibia. (n= 5). Significant differences between groups were identified by unpaired student t-test, error bar= SEM, * $p < 0.05$, ** $p < 0.01$, **** $p < 0.0001$.

Figure 3:

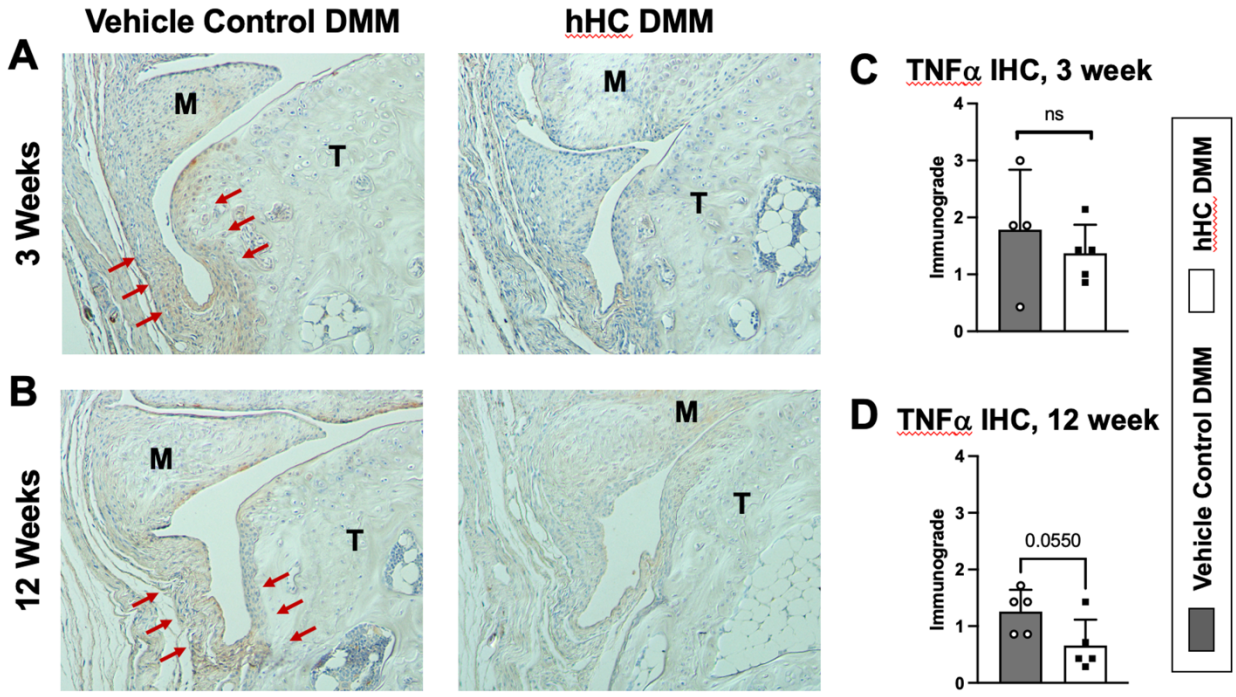

Figure 3. Hydrolyzed hyaline cartilage supplement reduces synovial inflammation in PTOA. A) representative TNF-alpha immunohistochemical stained slides of knee joints from hHC and control mice collected three weeks post-DMM, and B) twelve weeks post-DMM. M= meniscus, T= tibia, arrows point to the area of intense positive stain in synovium tissue. C) Immunograding of TNF-alpha IHC slides three weeks post-DMM and D) twelve weeks post-DMM. (N= 5), error bar= SEM, IHC= Immunohistochemistry.

Figure 4:

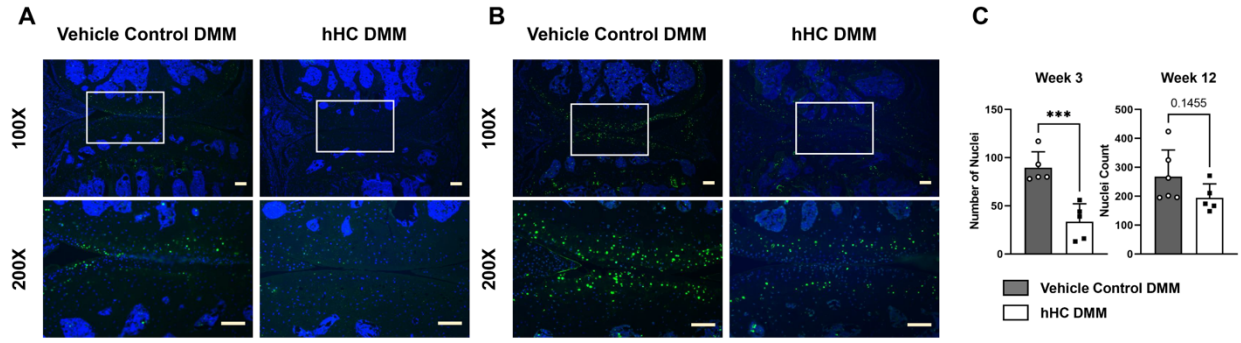

Figure 4. Hydrolyzed hyaline cartilage reduces chondrocyte apoptosis in PTOA. A) representative slides showing TUNEL staining in knee joints of hHC and control mice harvested three weeks-post DMM and B) twelve weeks post-DMM. Green=TUNEL positive nucleus, Blue= Dapi counter stained nucleus. Scale bar=?, C) Comparison of the number of TUNEL positive nuclei in hHC and control mice at three and twelve weeks time points. (N= 5), Significant differences between groups were identified by unpaired student t-test, error bar= SEM, ***p<0.001. TUNEL= Terminal deoxynucleotidyl transferase dUTP nick end labeling.

Figure 5:

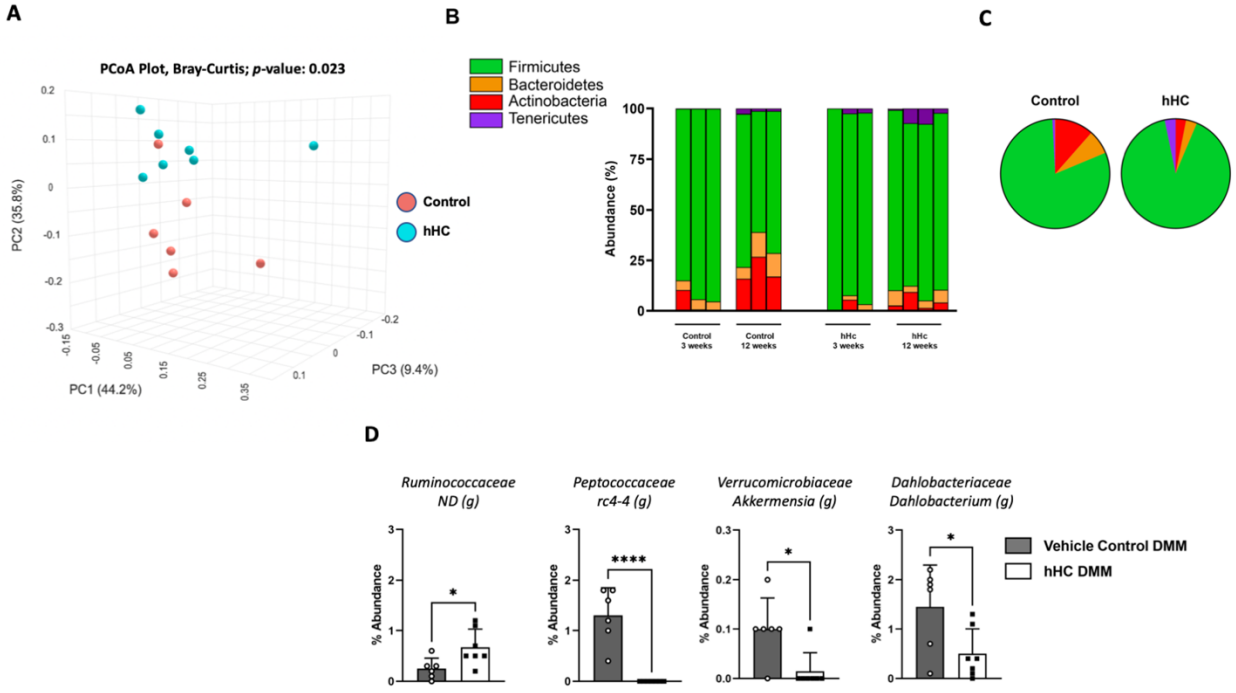

Figure 5. Hydrolyzed hyaline cartilage shifts gut microbiome composition. A) Principal coordinate analysis was performed on 16s sequencing data of fecal samples from all hHC and control group mice. The dissimilarity of the relative abundance of samples in three-dimensional space corresponds to the Bray-Curtis Beta-diversity of samples at the genus level. Permutational multivariant analysis of variance (PERMANOVA) test resulted in p=0.023. B) The relative abundance of phyla in hHC and control mice three or twelve weeks post-supplementation is depicted by bar charts (n=3 or 4/time point). C) The average abundance of phyla in hHC and control mice is depicted by pie charts (n=6 or 7/ treatment group). D) Relative abundance of a not-defined genus in the family of *Ruminococcacea*, rc4-4 genus in the family of *Peptococcaceae*, *Akkermensia* genus in the family of *Verrucomicrobiaceae*, and *Dahlobacterium* genus in the family of *Dahlobacteriaceae* were significantly different between two treatment groups (n=6 or 7/ treatment group). Significant differences between groups were identified by unpaired student t-test, * $p < 0.05$, **** $p< 0.0001$.

11. Appendix 3: Villani et al, Manuscript In Revision, JCI Insight

Obesity Related Gut Dysbiosis Promotes Synovial Inflammation and B Cell Infiltration Prior to Osteoarthritic Cartilage Degeneration

David A. Villani*[,1,2], Eric M. Schott*[,3], Jacquelyn A. Myers *[,4], Jun Zhang[5], Ann Lindley Gill[6], David Claypool[7], Christopher W. Farnsworth[8], Javier Rangel-Moreno[9], Honey Hendesi[1], Samantha H. Landgrave[1,2], Karin A. Payne[1], Larry W. Moreland[1,7], Jennifer H. Anolik[9,10], Lacey J. Favazzo[1], Robert A. Mooney[10], Kristine A. Kuhn[7], Steven R. Gill[6,#], and Michael J. Zuscik[1,2,#]

[1]Colorado Program for Musculoskeletal Research, Department of Orthopedics, University of Colorado, Anschutz Medical Campus, Aurora, CO, USA

[2]Cell Biology, Stems Cells & Development PhD Program, University of Colorado, Anschutz Medical Campus, University of Colorado, Aurora, CO, USA

[3]Solarea Bio, Cambridge, MA, USA

[4]Genomics Research Center, University of Rochester Medical Center, Rochester, NY, USA

[5] Center for Plastic & Reconstructive Surgery, Department of Orthopedics, Zhejiang Provincial People's Hospital, Hangzhou, Zhejiang, China.

[6]Department of Microbiology & Immunology, University of Rochester Medical Center, Rochester, NY, USA

[7]Division of Rheumatology, Department of Medicine, University of Colorado, Anschutz Medical Campus, Aurora, CO, United States.

[8]Department of Pathology & Immunology, Washington University, St. Louis, MO.

[9]Division of Allergy, Immunology and Rheumatology, University of Rochester Medical Center; Rochester, NY, USA

[10]Center for Musculoskeletal Research, University of Rochester Medical Center, Rochester, NY, USA

*equal first author contribution
[#]equal senior author contribution

Corresponding Author
Michael J. Zuscik, PhD
Colorado Program for Musculoskeletal Research
Department of Orthopedics
Anschutz Medical Campus
michael.zuscik@cuanschutz.edu

Abstract

A dysbiotic gut microbiome contributes to obesity-associated osteoarthritis (OA) via an inflammatory signature radiating from the gut to the joint. Here we hypothesize that this chronic inflammatory cascade in obesity precedes initiation of OA, and thus is pathogenic. To explore this, knee joints were collected from obese mice to study tissue-level joint structure and support RNA-seq analysis of synovium. Despite no evidence of OA, synovium from obese mice had a pro-inflammatory gene expression profile, with evidence of a B cell signature that was confirmed by flow cytometry. To determine if enhanced trafficking of B cells from the gut to the joint was involved, we used KikGR photoconvertible mice. After photoconversion of colon-localized cells from KikGreen to KikRed, knees from obese mice were found to have more KikRed CD19+ B cells than lean controls, indicating enhanced migration from gut to joint in obesity. Obese OA patients undergoing total knee arthroplasty had increased numbers of B cells as well, establishing human relevance. Overall, the obese synovium has a B cell+ inflammatory signature that involves migration of these cells from the gut, suggesting a pre-OA impact of obesity on the synovium that may be an initiating event in the OA of obesity.

Introduction

Osteoarthritis (OA) is one of the most prevalent disabling diseases in the United States, with 25% of the US population projected to be diagnosed with some form of OA by 2030 [1]. Patients with OA experience physical impairment due to joint pain, which is the primary cause of disability [2]. Consequently, OA has a significant economic impact, evidenced by its $136 million annual cost [3]. Since symptom palliation is the only clinically available treatment strategy to treat OA, a disease modifying approach to treat OA is a critical unmet need [4]. Obesity is a critical risk factor for developing OA, and its prevalence is increasing globally due in large part to the expanding consumption of a Western high-fat diet [5]. By 2030, it is projected that 38% of the global adult population will be overweight, and an additional 20% will be obese [6]. This contributes to an increased prevalence of OA with 66% of adults diagnosed with OA overweight or obese [7].

Historically it has been hypothesized that overweight and obese patients are at elevated risk for arthritis because of increased mechanical load in weightbearing joints; however, although increased loading is a factor, it cannot explain the increased risk of OA in the non-weight bearing upper extremity joints of obese patients [8]. Rather, as we and others have shown, there are systemic inflammatory changes caused by obesity that lead to increased immune cell populations and inflammatory cytokines in joint tissues [9-14]. This systemic signature of inflammation leads to various impacts on joints, including synovial hyperplasia, osteophyte formation, and the production of cartilage-degrading catabolic proteins by chondrocytes and other cells, each contributing to the OA degenerative process [9, 10]. Additionally, injury models of post-traumatic OA reveal that obese mice experience accelerated disease progression compared to non-obese mice [9, 15]; however, even in the absence of injury, obese mice spontaneously develop OA pathologies [16]. Despite the known associations between obesity, inflammation, and accelerated OA in the context of established disease, the underlying factors that initiate the OA of obesity remain undetermined.

The synovial membrane, comprised of fibroblast-like synoviocytes (FLSs) and numerous resident and infiltrating immune system cell types, is an important component of the diarthrodial joint,

providing lubrication via the production of lubricin and hyaluronic acid, which support low friction joint articulation [17]. The synovium helps maintain cartilage homeostasis through the delivery of essential nutrients to chondrocytes as well as through the removal of metabolic waste and turn-over of degraded matrix components [17]. In obesity, the synovial membrane becomes a source of proinflammatory cytokines and chemokines, resulting in the infiltration of monocytes and macrophages that potentiate the proinflammatory state [17-19]. Catabolic proteins, such as matrix metalloproteinases (MMPs) and aggrecanases, are secreted into the synovial fluid by both synoviocytes and infiltrating immune cells, leading to the degeneration of the cartilage matrix [17-19].

One potential source of this synovial inflammation is the gut microbiome, a known driver of obesity-associated inflammation [20]. Studies have demonstrated that transplantation of the obese gut microbiome reproduces the inflammation associated with obesity in germ-free animals [21, 22]. Obesity and its associated inflammatory impacts are known to have dramatic effects on immune cell populations [23]. Alterations in both immune cell migration and immune cell number have been reported in the context of obesity [24-26]. In fact, obesity has been shown to cause alterations in the immune cell populations present within the intestinal immune system [27, 28]. It follows that we and others have shown that obesity in the context of OA is associated with gut microbiome dysbiosis [29-32] ,with our group documenting that correction of the dysbiosis protects against acceleration of obesity-associated OA via a decrease in both systemic inflammation and reduction of immune cells present within the joint, particularly infiltrating monocytes and macrophages [29]. Recent studies provide evidence that immune cells from the intestine can migrate from the colon to sites of metabolically altered tissues [28]. However, no studies to date have directly assessed the impact of the microbiome on immune cell migration from the colon to the joint in the context of OA.

We have previously observed development of synovial hyperplasia histologically in a murine model of high fat diet-induced OA [29, 33]. Based on this finding, and from the perspective of the work summarized above, we hypothesized that early obesity-induced dysregulation of the synovium is an event that precedes the development of joint degeneration in the OA of obesity. To test this hypothesis,

we first performed bulk RNA sequencing of synovial tissues from both lean and diet-induced obese mice. Transcriptome analyses support our previous findings that obesity leads to an enhanced inflammatory state in synovial tissues [33], with a novel B cell signature in the synovium of obese animals, as well as an enrichment in other inflammatory pathways and a monocyte/macrophage lineage cell signature. The translational relevance of these findings was confirmed by enrichment of B cells in human synovium from low and high BMI patients undergoing total knee arthroplasty for terminal OA. Lastly, we utilized the KikGR mouse model, which contains a photoconvertible GFP protein that rapidly converts from KikGreen to KikRed upon exposure to 405nm light, to determine if the synovial inflammatory profile involves immune system cells, particularly B cells, trafficking from the dysbiotic obese gut to the joint.

This study provides the first evidence that synovial dysregulation occurs before tissue-level evidence of joint degeneration in the OA of obesity. Further, it offers the first direct evidence of immune cell migration from the gut to the joint, demonstrating that obesity, prior to the onset of OA, alters this immune cell migratory pattern. This suggests a potential obese gut-related programming of migrating cells that might be causative in initiating degeneration of joints. Overall, these data argue that therapeutics targeting synovial inflammation and immune cell migration to the joint before OA symptoms develop could provide protection against joint degeneration in the context of obesity.

Results

Synovial hyperplasia precedes cartilage degeneration in obese mice: Male mice consuming high fat or lean control diet for 16 weeks, starting at 5 weeks of age, were euthanized and their joints were harvested for histology. Histomorphometric analysis of Safranin-O/Fast/Green-stained knee samples revealed that there is no evidence of cartilage damage in either lean or obese mice at this early time point (Supplemental Figure 1, A-G). The only evidence of tissue level change was the regular presence of a thickened synovial membrane in the obese cohort, highlighted in the representative image (Supplemental Figure 1A).

RNA-seq reveals differential expression of genes, with cell signatures identifying a proinflammatory phenotype in the obese synovium: Transcriptome analysis of peri-articular soft tissue (PAST) isolated from obese and lean mice after 16 weeks of lean control or high-fat diet demonstrated significant alterations in the synovial gene profile in the context of obesity, well before any visible pathologic joint changes occurred. Expression analysis revealed 1,122 differentially expressed genes (DEGs), 719 of which were upregulated and 403 of which were downregulated in obesity (Figure 1A, Supplemental Table 1 and 2). Principle component analysis (PCA) based on quantification of gene signature dissimilarity revealed that the synovial gene profile of lean mice was distinct from the synovial gene profile of obese mice (Figure 1B). Following initial characterization of DEGs, we performed a cell type enrichment analysis (Cten) to examine cell mediators, revealing that the number of macrophages was significantly increased in the synovium of obese mice, based on 29.9% of all upregulated genes being associated with this cell type (macrophage and mix) (Figure 1C). Surprisingly, a strong B cell signature was also identified (Figure 1C). Although B cells are rarely implicated as mediators of OA [34], they could be involved in the early pathogenesis of the OA in the specific context of obesity. These data provide evidence supporting the hypothesis that synovial gene expression profile and inflammatory cell signatures preexist in the synovium of obese mice, preceding evidence of cartilage degeneration or any other joint tissues changes associated with OA.

Pathway analysis reveals upregulation of genes associated with inflammatory signaling: We performed an enrichment analysis with Enrichr, which contains a diverse set of gene libraries capable of identifying enriched gene ontology (GO) terms and transcription factors based on the input data. GO enrichment identified terms associated with inflammation and immune cell trafficking, including *Leukocyte Activation, Inflammatory Response*, and *Positive Regulation of Cytokine Production,* as represented by gene set enrichment graphs (GSEA) (Figure 2A). Enrichr also identified significantly upregulated transcription factors, many of which play a role in the activation of immune cells (Supplemental Figure 2B). To identify pathways potentially involved in the early pathogenesis of the OA of obesity, we evaluated DEGs with Ingenuity Pathway Analysis (IPA), and identified 97 significant canonical pathways, with 29 predicted to be activated, and 5 predicted to be inhibited based on activation score (Z-score). The top 25 significantly activated pathways are shown in Table 1. At the top of the table, we highlight 10 key pathways associated with obesity and inflammatory processes. Not surprisingly, these pathways included IL-8 Signaling, *NFkB* Signaling, VEGF Signaling, Dendritic Cell Maturation and Type II Diabetes Mellitus Signaling. Six of the highlighted pathways are implicated in immune cell signaling: Leukocyte Extravasation Signaling, Production of Nitric Oxide and Reactive Oxygen Species in Macrophages, *FC* Receptor-mediated Phagocytosis in Macrophages and Monocytes, FcγRIIB signaling in B lymphocytes and B Cell Receptor Signaling. Interestingly, the identification of FcγRIIB signaling in B lymphocytes and B Cell Receptor Signaling suggests that B cells maybe involved in the onset of the OA of obesity. Of note, more than half of the top 25 canonical pathways are associated with inflammatory pathways, highlighting the strength of concept that obesity leads to a pre-OA inflammatory process in the synovial membrane.

The upregulation of the canonical pathways identified by IPA in obese mice is shown in a heatmap displaying individual genes involved in *Leukocyte Extravasation Signaling, FC Receptor Mediated Phagocytosis, NF-kB Signaling*, and *IL8 Signaling* (Figure 2, B-E). These heatmaps demonstrate that the predicted activation score is not based on merely a few genes in the pathway, but rather every gene in the pathway is upregulated in obesity. A Venn Diagram separating genes involved

in the activated pathways shows minor overlap (Supplemental Figure 2B), confirming that the pathway results are not based on a few strongly upregulated genes. These data detail the strength of the inflammatory response in the synovium of obese mice early in the degenerative process that later leads to joint degeneration.

Diseases and Functions analysis uncovers a rheumatoid arthritis-like signature: In addition to identifying significant canonical pathways, analysis of the DEG with IPA revealed various Diseases and Functions associated with the DEGs. Twenty-eight Diseases and Functions annotations are involved in the inflammatory response, 40 play a role in cellular movement, and 34 impact immune cell trafficking. Highlighted in Figure 3 are four of the Diseases and Functions found to be significant, including *Leukocyte Migration*, *Inflammation of the Joint*, *Rheumatoid Arthritis*, and *Leukocyte Activation* (Figure 3, A-D). To visualize the depth of the overlap between these four highlighted diseases and functions, a Venn Diagram comparing the individual differentially expressed genes in each was developed (Figure 3E). Genes involved in *Inflammation of the Joint* and *Leukocyte Migration* are very similar to those in the *Rheumatoid Arthritis* signature, suggesting that the pathogenesis of the obesity-associated OA may have some similarity to the disease process that underlies other types of inflammatory joint pathologies. Overall, the analysis of gene signatures that correspond to specific Diseases and Functions provides strong evidence for the involvement of inflammation and immune cells in the early stages of the OA of obesity. Collectively, these data provide additional rationale for targeting immune cell activation and migration as a therapeutic strategy to treat this unique disease process.

B cells may be involved in early synovial changes in the OA of obesity: Analysis of the transcriptome of synovial tissues from lean and obese mice not only provides further evidence for inflammation in the OA of obesity, but it implicates B cells as potential mediators of the disease. IPA yielded three significant canonical pathways relating to B cell function, including *PI3K Signaling in B Lymphocytes*, *B cell Receptor Signaling*, and *FcγRIIB Signaling in B Lymphocytes*, all of which are indicative of B cell activity (Figure 4A). Additionally, two Diseases and Functions related to B cells were

found to be significant including *Quantity of B Lymphocytes* (Figure 4, A and B) and *Proliferation of B Lymphocytes* (Figure 4A), possibly suggesting the synovium of obese mice contains increased B cells compared to lean mice. To confirm this, we performed flow cytometry on PAST cells isolated from the knee joints of lean and obese mice. We identified a greater than 2-fold increase in the number of CD19+ B cells in the joint (Figure 4C), validating the concept that B cell numbers are increased in the pre-OA phase in the context of obesity. These data suggest a potential role for a novel inflammatory/immune system mediator in the OA of obesity

B cells are present in the synovium of obese human patients: To determine if the B cell signature we found in obese mice is present in human OA, we examined synovial tissue obtained from OA patients undergoing a total knee arthroplasty using an immunofluorescence approach. Mirroring our findings in mouse knees, we found that OA patients with a normal BMI (<25) had minimal evidence of immune cells in their synovium (Figure 5A). Comparatively, OA patients who were overweight (BMI 25-30) or obese (BMI>30) had accumulations of lymphocytes under the synovial lining and around blood vessels (Figure 5A). The morphological features of these clusters resemble ectopic lymphocytic aggregates (ELAs) commonly present in rheumatoid arthritis patients [35]. We next proceeded to define the cellular composition of the ELAs in the synovium of OA patients using immunofluorescence (Figure 5B). Obese and overweight human patients showed evidence of ELAs within the synovial membrane (Figure 5C). Consistent with previous studies, ELAs were mainly composed of follicles densely populated by CD20+ B cells intermixed with CD3+ T cells (Figure 5, B and D). CD68+ macrophages were found sparingly within ELAs and were preferentially located in the lining of the synovium (Figure 5, B and E). Quantification of each cell type within ELAs revealed higher numbers of CD20+ B cells compared to CD3+ T cells or CD68+ macrophages (Figure 5E).

Assessing the role of the gut microbiome in initiating the inflammatory signature in joints: Previous work from our group and others has established that consumption of the high-fat diet induces changes within the microbiome that contribute to OA progression [29-32]. Our interest in exploring the potential impact of this gut dysbiosis on immune cell trafficking from the gut to the joint,

which could explain some of the phenotype revealed by our RNA-seq findings, led us to employ the KikGR transgenic mouse to examine if an obesity-induced gut dysbiosis and intestinal inflammation led to alterations in immune cell trafficking to joints. In the KikGR model, all somatic cells encode a photoconvertible GFP transgene that constitutively emits green light (KikGreen) but that can be converted to red emission (KikRed) upon exposure to 405 nm light. We placed KikGR mice on the lean or high fat defined diets and confirmed that high fat fed mice displayed an increase in body mass and blood glucose compared to lean controls (Supplemental Figure 3, A, B, and C) confirming our previously described obese phenotype [29, 33].

We also confirmed the presence of a dysbiotic shift in the gut microbiome in the obese context in the KikGR model. At the phylum level, *Actinobacteria* were decreased in obese animals, with a concomitant increase in *Firmicutes* (Supplemental Figure 4A). At the genus level, the mean relative abundance of *Sutterella* was reduced within the obese gut, with increases in *Lactococcus, AF12,* and an unidentified genus of the Peptostreptococcaceae *family* (Supplemental Figure 4, B and C). To further examine these differences, linear discriminant analysis of effect size (LEfSe) was performed. LEfSe analysis identified 11 taxa differentially present between the animals consuming the high fat and lean control diet (Supplemental Figure 5, A and B). Interestingly, 9 of the 10 taxa that increased in the high fat-fed animals were from the phylum *Firmicutes*, which has previously been associated with obesity [36, 37]. *Faecalibaculum rodentium*, a species known to decrease inflammation within the colon and have anti-obesity effects [38], was increased within the lean animals (Supplemental Figure 5B). These data confirm that consumption of the high fat diet shifts the microbial community in obese KikGR transgenic mice, largely mirroring shifts that have been previously established in the murine context.

Migration of immune system cells between the colon and the joint occurs in the context of obesity: In response to shifts in the gut microbiome caused by obesity, it is established that associated shifts in immune system surveillance plays out at the gut barrier, characterized particularly by increases in pro-inflammatory immune cell populations in the distal colon [29, 39]. To determine if this shift in colon immune cell populations plays a role in the early inflammatory signature observed in

the joint, we utilized KikGR mice to directly assess if migration of immune cells from the gut to the joint occurs in the context of obesity. The cells of the distal colon of KikGR mice were photoconverted from KikGreen to KikRed using a fiberoptic colonoscope with a laser tuned to 405 nm (Supplemental Figure 6A). Optimization was performed to identify both the ideal duration of photoconversion and the appropriate harvest timepoint of the joint (Supplemental Figure 6, B and C). Minimal photoconversion was seen within the lamina propria and mesenteric lymph nodes (Supplemental Figure 6D). Flow cytometry was performed on mouse joints harvested from lean and obese KikGR mice (Figure 6A). Like the finding shown in Figure 4C, the number and percent of CD19+ B cells were significantly increased in the synovium of obese KikGR mice compared to lean controls (Figure 6B), as were F4/80+ macrophages (Supplemental Figure 7A, B). Remarkably, there was also a significant increase in the number of CD19+ KikRed+ B cells, which based on their red color indicated their origination in the distal colon (Figure 6C). Other immune cells that could migrate from the colon to the joint, including CD3+ T cells, Nk1.1+ natural killer cells, and F480+ macrophages, also display the propensity to migrate, but did not show a discernible difference in the magnitude of gut to joint migration in high fat-fed obese and lean-fed control mice (Figure 6, D, E, and F). These data suggest that immune cell populations do indeed translocate from the colon to the joint, with the presence of obesity driving an increase in B cell migration specifically. This is the first direct evidence of immune cell migration from the distal colon to the joint in the context of obesity, further supporting the potential role of the B cell in the OA of obesity.

Discussion

It has been established that the OA of obesity is a disease process distinct from other forms of OA, with inflammation playing a primary role [2, 4, 9, 13, 14, 40-42]. However, we do not yet understand the early disease process that may serve to initiate OA degeneration, which we hypothesize takes place in the context of obesity before evidence of cartilage degeneration. Although key changes that play out directly in chondrocytes/cartilage and in osteoblasts/subchondral bone leads to initiation of OA disease generally, the key role of inflammation in the OA of obesity likely depends on a significant involvement of the synovium, which is a focal point for the production of cytokines and factors that impact cartilage and bone [33, 43-45]. Therefore, in this study, we focus on understanding how the synovium plays a critical role in the early stages of joint degeneration that play out in the OA of obesity. Here we provide the first evidence of a pro-inflammatory synovial environment, downstream of a gut microbiome dysbiosis that leads to the trafficking of immune cells, particularly B cells, as an early signal that precedes joint degeneration during obesity.

To explore the pathogenic role of the synovium in the OA of obesity, we performed bulk RNA-seq of synovial tissue from lean and obese mice after four months of high-fat or lean diet, a time point where no evidence of cartilage destruction is histologically present. Cell type enrichment analysis (Cten) found that almost 30% of all upregulated genes were related to macrophages, strongly suggesting their role in the early stages of the OA of obesity (Figure 1). In recent studies, populations of macrophages have been identified in the synovium of obese mice and humans, making them a candidate target for therapeutic intervention [10, 46]. Paradoxically, systemic depletion of macrophages in obese mice led to more severe OA, with an influx of T cells and neutrophils to the synovium [47]. Specific targeting of pro-inflammatory macrophages using resolvin D1 resulted in protection in the OA of obesity via a reduction of pro inflammatory cytokines and a decrease in the total number of infiltrating macrophages [48]. These data suggest that tissue resident macrophages are necessary for joint homeostasis, and their depletion may lead to potentiation of disease [47, 48].

Our RNA-seq analyses also identified a strong upregulation of genes associated with inflammatory pathways, immune cell activation, and immune cell infiltration, providing evidence that inflammation drives the OA of obesity. One of the top activated canonical pathways was *Type 2 Diabetes Signaling* (Table 1). Obesity is a major risk factor for the development of T2D [49-53] which is associated with elevated levels of systemic inflammation and insulin resistance [49-51, 54]. Though the synovium is not thought of as a classically insulin responsive tissue, it is possible that insulin signaling plays a role in joint homeostasis, as it has been shown to have anti-inflammatory effects in various tissues, acting as an NFkB antagonist [55, 56].

Along with T2D signaling, analysis of canonical pathways identified *NFkB Signaling* as an activated pathway in the synovium of obese mice. NFkB is thought to play a role in OA by activating expression of various proinflammatory cytokines and catabolic enzymes including MMPs, IL-1b, and TNF [57, 58]. A recent study demonstrated that heterozygous chondrocyte-specific deletion of *Rela/p65,* a key mediator of NFkB signaling, is protective in an injury model of OA by decreasing chondrocyte apoptosis and the matrix degrading and inflammatory mediators *Adamts5* and *Hif2a* [59]. These data align with our transcriptome results, demonstrating that NFkB may be an important driver of early synovial changes in the OA of obesity.

Activation of immune cell specific pathways, including *IL8 Signaling*, was another signature of the obese synovial membrane (Figure 2). IL-8 is a chemoattractant protein that contributes to an immune cell phenotype in the synovial membrane via recruitment and activation of neutrophils and some subsets of T-cells [60]. Additionally, IL-8 is known to induce MMP13, a key enzyme involved in OA progression [61]. Clinically, IL-8 has been found at elevated levels in the synovial fluid of OA patients.

In agreement with the pathway and cell type enrichment analyses, IPA analysis of Diseases and Functions supports the role of immune cell activation and inflammation in the OA of obesity. We observed a strong upregulation of genes associated with pathways related to ‘Inflammation of the Joint’ and ‘Activation and Migration of Leukocytes’ in obese synovium (Figure 3). Of note, ‘Rheumatoid

Arthritis' (RA) was one of the most significant Diseases and Functions signatures identified by IPA (Figure 3). RA is an autoimmune disorder characterized by synovial inflammation and autoantibody production, leading to cartilage and bone erosion [62]. While OA and RA both lead to significant cartilage degeneration, RA is associated with a significantly more robust inflammatory response, characterized by an influx of B cells, T cells, and macrophages that lead to more rapid cartilage and bone destruction than is found in OA [63, 64]. However, based on our understanding of accelerated joint degeneration in the OA of obesity, as well as data presented in this study, the OA of obesity may share some characteristics of RA, further differentiating the etiology of the OA of obesity from other forms of OA, and arguing that therapeutic strategies need to be tailored to the underlying cause of disease.

Supporting the concept that the OA of obesity has an RA-like gene signature, both the canonical pathway analysis and the Diseases and Functions analyses identified gene sets associated with B cell signaling and function. To confirm the increased presence of B cells, we performed flow cytometry, and found that B cells were indeed increased in obese joints compared to lean controls (Figure 4). In OA, B cells have been identified in synovial samples from patients at end stage disease but their abundance, heterogeneity, and role in the disease process is not well understood [34]. The obesity situation was not identified in this study, and to date B cells have not been formally implicated in the OA of obesity. In obesity, B cells can mediate metabolic syndrome by acting as antigen presenting cells that activate visceral adipose T-cells and macrophages, leading to the production of inflammatory cytokines [65, 66]. B cell depleted mice on a high-fat diet are protected from metabolic syndrome, despite the adiposity and weight gain, indicating that B cells are crucial to the development of inflammation and insulin resistance in obesity [65]. In RA, B cells contribute to disease in both autoantibody-dependent and -independent mechanisms [67, 68]. Autoantibodies produced by B cells can target various joint components, including type-I and type-II collagens, leading to the breakdown of the cartilage matrix [68]. Thus, it is possible that B cells could play both an autoantibody-dependent and -independent role in the OA of obesity.

Our animal model work yields compelling data about the role of obesity and immune cell changes in OA. To address human relevance, we performed immunofluorescence assays on human synovium from patients undergoing total knee arthroplasty. Importantly, we observed a relationship between formation of ELAs in the synovium and obesity in human OA, a previously unreported phenotype (Figure 5). ELAs develop in chronically inflamed, nonlymphoid tissues in response to systemic pro-inflammatory cytokines and chemokines, synoviocytes and resident macrophages recruit B cells, T cells, monocytes, and macrophages to the joint [69]. In RA, the presence of ELAs and B cell infiltrates associate with joint damage over time [70, 71]. ELAs are involved in T cell priming and the formation of RA autoantibody production [72]. Our data support a role for ELAs in OA disease pathogenesis. Importantly, identification of a unique lymphoid pathotype in overweight/obese OA patients refutes the concept of OA as non-inflammatory disease and reveals cellular targets for designing personalized therapies based on the unique histopathological features detected in an individual's synovial tissue.

One source of inflammation in obesity is the gut microbiome [73]. The gut microbiome is an ecosystem of microbes present in the host, with the highest abundance found within the cecum and colon [74]. Numerous studies indicate that the gut microbiome plays a role in the metabolic and inflammatory effects of obesity [21, 75, 76], with the composition of the microbiome significantly impacted by obesity [22, 77]. Moreover, germ-free and antibiotic-treated mice are both protected from the metabolic effects of obesity, implicating the dysbiotic obese gut microbiome as a potential therapeutic target in obesity [78, 79]. In trying to understand where the inflammatory cascade might initiate in the OA of obesity that could feed either the macrophage or B cell contributions to disease, we confirmed a shift in the microbes present within the obese gut niche leading to a classic obesity-associated gut dysbiosis [29] (Supplemental Figure 4). LEfSe analysis identified 11 different taxa with differing abundance between the high fat and lean control animals (Supplemental Figure 5). Of these 11 taxa, 10 of them belonged to the Firmicutes phylum which has been associated with increases in inflammation and decreases in general health [80]. We also saw a decrease in Actinobacteria within the

obese animals, with specific decreases seen within *Bifidobacterium*, a genus associated with positive health effects, and particularly with protection in the OA of obesity [29, 81]. Interestingly, *Faecalibaculum rodentium*, a species associated with decreases in inflammation and protection in obesity, was elevated within lean animals [38].

Since many body systems rely on signals from the gut microbiome to function optimally, changes in the microbial makeup can impact distal tissues [82]. The presence of microbial antigens contributes to modulation of immune cell function, evidenced by the dysfunctional immune system of germ-free mice [82, 83]. Obesity and gut microbiome changes have been shown to impact both the systemic and colonic immune system activity [39, 84, 85]. Obesity leads to a pro-inflammatory shift within the intestinal immune environment in the form of an increase in CD8+ T cells and T_H1 cells and a decrease in protective TH17 cells and IL10+ T regulatory cell (T_{regs}) within the colon, all of which have been implicated in inflammatory disease processes in the gut [86-89]. Interestingly, B cells have also been implicated in obesity, with details emerging that obesity leads to a decrease in the number of B cells within the gut [85]. In addition to altering the number of these immune cells, function, differentiation and migration patterns are also impacted [90-93]. IgA+ B cells have been shown to migrate to the liver, increasing in liver disease [91] and can make their way into systemic circulation and migrate to other sites of inflammation [90]. Furthermore, migration of B cells to the synovium was observed in a collagen-induced rheumatoid arthritis model [94]. Thus, it is entirely plausible that immune cells could migrate from the colon to other metabolically compromised tissues, such as the synovium, in the context of obesity.

Individual members of the microbiome have been implicated in altered immune cell function and migration. *Bifidobacterium,* a genus that is present within the lean samples and virtually absent in obese animals, has been shown to impact both T cell and B cell function within the gut [95, 96]. Systemically, *Bifidobacteria* can restore immune cell imbalances seen in obesity as well as decrease B cells and macrophages in the mesenteric lymph nodes [97]. However, no studies have directly assessed the effects of *Bifidobacterium* on the colon immune system.

The impact of obesity on immune cell migration from the colon to the joint has not been previously investigated. Here we used the KikGR mouse model to directly evaluate immune cell migration from the colon to the joint. The KikGR protein is a green-to-red photoconvertible protein that is constitutively expressed under a CAG promoter [98]. The protein is stable under normal conditions and undergoes rapid photoconversion from green emitting to red emitting after exposure to 405nm light [98]. Using a method to selectively photoconvert the colon without injury, in which gut-joint T cell trafficking has been previously demonstrated, we employed an endoscopic colonoscope in obese and lean mice to circumvent the off target photoconversion produced by more invasive methods of photoconversion and limited photoconversion to the distal colon [99-102]. In agreement with a prior report of T cell trafficking from the colon to the joint, we noted T cell migration in our model [102]. Although migration of T cells, monocyte/macrophage lineage cells, and NK cells also were observed to move from the colon to the joint in our model, only CD19+ B cells were found to have enhanced migration under the influence of obesity (Figure 6).

To date, this is the first study to show that obesity, possibly as a result of a gut microbiome dysbiosis, leads to enhanced B cell migration from the gut to the joint. Importantly, this ramped-up migration of B cells occurs without any evidence of OA in the joint, raising the possibility that in obesity increased trafficking from the gut to the joint could be an initiating signal in the joint degenerative process.

From the data presented in this study, we propose a model describing early synovial changes that may be pathogenic in the OA of obesity (Figure 7). Systemic inflammation that is present in obesity induces synoviocytes to secrete chemoattractant factors [29, 103] leading to the recruitment of macrophages and B cells to home to the joint. Inflamed synoviocytes and activated macrophages secrete proinflammatory cytokines and proteolytic enzymes into the synovial fluid that then degrade the cartilage matrix. It is still unknown what role the B cell plays in the OA of obesity, but three possible mechanisms may contribute to joint degeneration: B cells may act as antigen presenting cells to activate other local immune system cells such as T cells, they may produce autoantibodies that target

native joint tissues, or they may produce pro-inflammatory cytokines that augment the inflammatory environment in the joint. In either of these scenarios, data presented here strongly support the notion that the OA of obesity is preceded by a disease state in the synovial membrane, which drives further degeneration joint specific tissues.

Conclusion: This study provides the first evidence of inflammation in the pre-OA obese synovium, leading us to propose that molecular and cellular changes in the synovial membrane initiates the development of OA in the obese context. We document that B cells, previously unappreciated mediators of the OA of obesity, are increased in the synovial tissues of obese mice. This corresponds with evidence of B cell signaling pathways that may play a significant role in the initiation or early development of obesity-associated OA. Finally, we demonstrate for the first time that various immune system cells migrate from the gut to the joint, with B cells specifically moving with higher frequency when an obesity-associated gut microbiome dysbiosis is present. This offers the possibility that the obesity gut microbiome may uniquely prime these cells to contribute to the initiation of cartilage degeneration. These findings provide a new perspective on OA of obesity disease pathogenesis, underscoring the potential of a novel therapeutic strategy targeting early inflammation and gut dysbiosis that warrants further investigation.

Methods

Animals: Handling of mice and all experimental procedures were reviewed and approved by either the University of Rochester Committee on Animal Resources (UCAR) or the University of Colorado Anschutz Medical Campus IACUC. Mice (C57BL/6J) were purchased from The Jackson Laboratories and housed at a density of 4-5 mice per micro-isolator cage in a room with a 12-hour light/dark schedule. At 5 weeks of age, mice were provided ad lib access to either a low-fat (Lean) diet (10% kcal from fat, Open Source Diets, #D12450J) or high fat (Obese) diet (60% kcal from fat, Open Source Diets, #D12492) (Open Source Diets; Research Diets Inc.). Mice were maintained on these diets until termination of the experiment (21 weeks of age). For immune cell trafficking experiments, KikGR mice (Tg(CAG-KikGR)33Hadj/J, Jackson Lab catalog #013753) were placed on high fat or lean diets as above for 28 weeks.

Knee joint tissue histologic analysis: After feeding protocols, mice were euthanized using CO2 followed by cervical dislocation, an American Veterinary Medical Association (AMVA)-approved method. The right knee joint was removed and fixed in 10% neutral buffered formalin (NBF) at room temperature for 72 hours. After 3 rinses in PBS, knee joints were then decalcified in EDTA for 2 weeks, followed by processing using a microwave processor, followed by embedding in paraffin using an established protocol [29, 104]. Tissue blocks were then cut in 5-micron thick sections in the midsagittal plane through the medial compartment of the joint at three levels, with 50 microns between each level. Sections from the joints were stained with Safranin O/Fast Green for analysis and unstained knee sections were used for immunohistochemical (IHC) staining.

Mouse synovial capsule tissue isolation: From the left knee of the euthanized mice, joint capsules were immediately removed as previously described [29] and flash frozen in liquid nitrogen. Briefly, the skin of the lower extremity was removed, followed by removal of the muscle and connective tissue adjacent to the joint capsule. Next, the patella and surrounding joint capsule was removed by making perpendicular incisions at both the proximal (femur) and distal (tibia) ends of the patellar tendon. These incisions were extended as far as possible to the anterior of the joint on both the medial

and lateral sides, and longitudinal incisions were made to connect the proximal and distal incisions on both sides. The result is a rectangular piece of peri-articular synovial tissue (PAST). Before flash freezing in liquid nitrogen, the patella, patellar tendon, and patellar fat pad were removed and discarded. The remaining rectangular pieces of PAST were then flash frozen in liquid nitrogen and stored at -80°C until further processing.

RNA extraction and sequencing: Frozen synovial tissue samples were homogenized in TRIzol (Life Technologies), followed by chloroform phase separation according to manufacturer's instructions. The aqueous layer was isolated, mixed with 100% ethanol in a 1:1 ratio, and the RNA was purified using the GeneJet RNA Purification kit per manufacturer's instructions (Thermo Scientific). Total RNA concentration was determined with the NanopDrop 1000 spectrophotometer (NanoDrop, Wilmington, DE) and RNA quality assessed with the Agilent Bioanalyzer (Agilent, Santa Clara, CA). The TruSeq Stranded mRNA Sample Preparation Kit (Illumina, San Diego, CA) was used for next generation sequencing library construction per manufacturer's protocols. Briefly, mRNA was purified from 200ng total RNA with oligo-dT magnetic beads and fragmented. First-strand cDNA synthesis was performed with random hexamer priming followed by second-strand cDNA synthesis using dUTP incorporation for strand marking. End repair and 3` adenylation was then performed on the double stranded cDNA. Illumina adaptors were ligated to both ends of the cDNA, purified by gel electrophoresis and amplified with PCR primers specific to the adaptor sequences to generate cDNA amplicons of approximately 200-500bp in size. The amplified libraries were hybridized to the Illumina single end flow cell and amplified using the cBot (Illumina, San Diego, CA). Single end reads of 100nt were generated for each sample using Illumina's HiSeq2500v4.

RNA-seq processing and differential expression analysis: Illumina sequencing data were processed using bcltofastq (v-1.8.4) to generate raw FASTQ files. Trimmomatic (v.0.32) was used to remove low quality bases and residual adapter sequences. Quality reads were aligned to GRCm38.p4 (Gencode-M6 annotation) using STAR (v2.4.2a) and gene level quantifications were generated using htseq-count (v0.6.1). Library size normalization and differential expression were performed using

DeSeq2 (v1.12.3) within the R statistical framework (v3.3.0). Significantly differentially expressed genes (DEGs) were defined as any gene with an adjusted p-value < 0.05. Cell type enrichment analysis was performed on up-regulated genes using CTen (http://www.influenza-x.org/~jshoemaker/cten/upload.php). Enriched canonical pathways and Diseases and Functions were evaluated using Ingenuity Pathway Analysis (IPA) using all significantly differentially expressed genes as defined above to drive these post-hoc analyses. Gene Ontology enrichments were evaluated by creating a ranked list of genes (using adjusted p-values and log2 fold change) and the preranked GSEA tool developed by the Broad Institute.

PAST cell flow cytometry from wild type mice: Cells isolated from the PAST of intact joints were assessed as previously described [29]. In short, PAST was harvested from mice and digested in collagenase for 2 hours to obtain periarticular soft tissue cells. Digested samples were filtered through a 70-μM nylon strainer (Corning Inc.) in ice cold PBS with 1% FBS and EDTA. Suspended cells were then pelleted and stained with fixable viability stain v450 (catalog 562247, BD Biosciences) for 40 minutes. Following washing, Fc block with rat anti–mouse CD16/CD32 (catalog 565502, BD Biosciences) was performed for 5 minutes prior to staining. All staining was performed for 30 minutes on ice at a concentration of 1:100. The following antibodies were used for phenotyping of cells: APC-Cy 7 rat anti–mouse CD19 (BD Biosciences, #557655), BV510 rat anti–mouse Ly-6G and –Ly-6C (BD Biosciences, #563040), Alexa Fluor 700 rat anti–mouse CD3 (BD Biosciences, #561388), Per-CP Cy5.5 hamster anti–mouse CD69 (BD Biosciences, #551113), BV711 rat anti–mouse F4/80 (BD Biosciences, #565612), Alexa Fluor 700 rat anti–mouse CD4 (BD Biosciences, #561025), BV605 rat anti–mouse CD45 (BD Biosciences, #563053), PE-Cy7 anti–mouse CD11c (eBioscience, #25-0114-82), PE anti–mouse CD11b (eBioscience, #15-0112-82), and eFluor 660 anti–mouse CD169 (eBioscience, #50-5755-82). All analyses were performed on a BD LSR II 18-color flow cytometer (BD Biosciences). Compensation was completed using anti-mouse or anti-rat/hamster compensation control beads (BD Biosciences, #560497 or #552845), and fluorescent minus 1 (FMO) control was used to determine positive gating. All data was analyzed using Cytobank software.

Collection and analysis of human synovial samples: Human synovial samples were collected from normal, overweight, and obese patients undergoing total knee arthroplasty for a diagnosis of advanced/terminal OA. Tissues were collected using a protocol reviewed and approved by the University of Rochester Institutional Review Board. Immediately following surgical removal of joint tissues, synovium was dissected free from other joint structures, placed in NBF, and fixed for 72 hours at room temperature. Following this, after 3 rinses in PBS, synovial tissue was processing using a microwave processor, followed by embedding in paraffin using a standard approach [105]. Tissue blocks were cut into 5-micron thick sections for staining and immuno-visualization of target proteins. A standard H&E staining protocol was used to support visualization of tissue organization. For analysis using immunofluorescence methods, synovial sections were incubated at 60^{o}C to melt the paraffin, and quickly transferred to xylenes. Slides were then progressively hydrated in absolute alcohol, 95% alcohol, 70% alcohol and water. Antigens were unmasked by boiling the slides for 30 minutes in a plastic coplin jar filled with antigen retrieval solution (Dakocytomation, S1699). Non-specific binding of antibodies was prevented by incubating slides at room temperature with 5% normal donkey serum (Jackson ImmunoResearch Laboratories, #017-000-121) dissolved in PBS containing 0.1% Tween 20 and Triton-X-100. Slides were incubated overnight, in a humid chamber at room temperature with goat anti-CD3e (Santa Cruz Biotechnology, clone M20), rabbit anti-human CD20 (Abcam, clone BV11) and mouse anti-human CD68 (Thermo Fisher Scientific, clone PG-M1). Primary antibodies were visualized with Alexa Fluor 568 donkey anti-goat Ig G (Thermo Fisher Scientific, #A11057), Alexa Fluor 488 F(ab')$_2$ donkey anti-rabbit Ig G (Jackson ImmunoResearch Laboratories, #711-546-152) and Alexa Fluor 647 F(ab')2 donkey anti-mouse Ig G (Jackson ImmunoResearch Laboratories, #715-606-151). Slides were briefly washed with PBS and mounted with vectashield mounting solution with DAPI (H-1200, Vector Laboratories). Pictures were taken with a Zeiss Axioplan microscope outfitted with a Hamamatsu camera. Immune cells populations were counted in 3-5 randomly chosen 200x fields per individual synovial section, using an automated count tool. Morphometric analyses were performed in a blinded manner.

Flow Cytometry of knee joints from KikGR mice: KikGR mice were sacrificed 72 hours post photoconversion with CO2 gas, followed by cervical dislocation. An established protocol was adapted to harvest cell suspensions from knee joints [106]. Briefly, intact joints were harvested, and care was taken to ensure bones were cut to exclude the growth plate. Tissues were washed with 10 mL of PBS to remove any residual marrow. Joints were then minced into small pieces with dissecting scissors and placed into wells of a 6-well plate filled with digestion media consisting of collagenase VIII (Sigma-Aldrich, #C2139, final concentration 1 mg/mL) and hyaluronidase (Sigma-Aldrich, #H3506, 2.5mg/ml) in RPMI 1640 supplemented with 10% FBS. After 30 minutes, the digestion solution was removed and quenched with RPMI1640 supplemented with 20% FBS, and new digestion media was added for an additional 30 minutes. Next, the final solution was quenched with RPMI 1640 supplemented with 20% FBS. The tissue was further disaggregated by passing the tissue through a 100μm cell strainer and rubber syringe. Cells were then washed in PBS and prepared for staining. A five-laser Cytek Aurora was utilized for KikGR flow cytometry experiments. All cells were handled in black wall tubes or protected from light until fixation occurred. Cells were stained for 30 minutes at a dilution of 1:100. Mouse BD FC Block (BD Biosciences, #553141) was used per manufacturer's instructions. The following antibodies were used**:** Brilliant Violet 421 Rat anti-Mouse F4/80 (BD Biosciences, #565411), APC-Cy7 Armenian Hamster anti-Mouse CD3 (BD Biosciences, #557596), Brilliant Violet 605 Rat anti-Mouse CD45R (Sony, #1116220), PE-Cy5 Rat anti-Mouse CD19 (Thermo Fisher Scientific, #15-0193-82), APC Rat anti-Mouse CD11b (BD Biosciences, #553312), PE-Cy7 Rat anti-Mouse Ly-6C (BD Biosciences, #560593), Alexa Fluor 700 Rat anti-Mouse Ly-6G (BD Biosciences, #561236), Brilliant Violet 650 Rat anti-Mouse CD161 (BD Biosciences, #564143) and Ghost Dye Violet 510 (Tonbo Biosciences, #13-0870). FMO controls were used to determine positive gating.

Colonic photoconversion in KikGR mice: After completion of the lean and high fat feeding regimens, KikGR mice were anesthetized with 3-5% inhaled isoflurane. At a depth of 20mm, a 7 French (2.3 mm) rigid colonoscope (Storz) was introduced into the colon. All colonoscopies were visualized with the attached camera. A 100 mW handheld laser light source provided light of 405 nm wavelength,

which was applied for 1 minute at each location (i.e., every 2.5 mm) before the apparatus was retracted. Total exposure time of colonic tissue was 8 minutes.

Cecal sample preparation, 16S sequencing, and taxonomic analysis: At the time of sacrifice, mice were euthanized using CO2 gas, followed by cervical disolcation. The cecum was isolated, and the contents were placed into a cryovial. The cryovial was then flash-frozen in liquid nitrogen and stored at -80°C. Total genomic DNA and RNA were extracted from samples using a modification of the ZymoBIOMICS^{TM} DNA/RNA Miniprep Kit (Zymo Research, Irvine, CA) and FastPrep mechanical lysis (MPBiomedicals, Irvine, CA). 16S ribosomal RNA (rRNA) was amplified using Phusion High-Fidelity DNA polymerase (New England Biolabs, Ipswich, MA) and primers specific to the V3-V4 hypervariable regions (338F: TCGTCGGCAGCGTCAGATGTGTATAAGAGACAGACTCCTACGGGAGGCAGCAG and 806R: GTCTCGTGGGCTCGGAGATGTGTATAAGAGACAGGGACTACHVGGGTWTCTAAT) followed by dual-indexed adapters P5: AATGATACGGCGACCACCGAGATCTACACxxxxxxxxTCGTCGGCAGCGTC and P7: CAAGCAGAAGACGGCATACGAGATxxxxxxxxGTCTCGTGGGCTCGG, similar to the method of Holm, et al. [107]. Amplicons were elucidated by agarose gel electrophoresis, pooled, and paired-end sequenced on an Illumina MiSeq (Illumina; San Diego, CA) at the University of Rochester Genomics Research Center. Sequencing runs include a positive control (a mock community of equal parts *Staphylococcus aureus, Lactococcus lactis, Porphyromonas gingivalis, Streptococcus mutans*, and *Escherichia coli* DNA) and two negative controls consisting of sterile water (amplification control) or buffer only (extraction control). Background microbiota were monitored at multiple stages of sample collection and processing. All sterile water, buffers, reagents, and plasticware used for sample collection, extraction and amplification of nucleic acid were UV irradiated to eliminate possible DNA background contamination. Raw reads from the Illumina MiSeq basecalls were demultiplexed using bcl2fastq version 2.19.1 requiring exact barcode matches. QIIME 2021.2 was used for subsequent processing [108]. Cleaning, joining, and denoising were performed using DADA2 prior to taxonomic

classification with a pretrained naïve Bayesian classifier trained with full-length 16S sequences **[109]**. Genus level differences between groups were analyzed by linear discriminant analysis (LDA) of effect size (LEfSe) [110, 111]. The LEfSe algorithm utilizes the non-parametric factorial Kruskal-Wallis sum-rank test to detect those features which are differentially abundant between groups, followed by pairwise Wilcoxon rank-sum tests and finally LDA to estimate the effect size of each differentially abundant feature.

Statistical analyses: non-omics data were analyzed and plotted using Graphpad Prism (version 9.4.1). Standard t tests or 2-way ANOVA tests (with appropriate post-hoc testing) were used to test significance, with specifics for each analysis described in the figure legends; p values < 0.05 were considered significant.

Acknowledgements

This work was supported by NIH NCATS TR000042 (RAM & MJZ), NIH NIAMS P50 AR054041-5471 (MJZ), DOD W81XWH1910807 (MJZ), NIH NIAMS R01 AR078414 (MJZ), NIAID R01 AI111914 (JRM), a trainee slot on NIH NIAMS T32 AR053459 (CWF), and Core services supported by NIH NIAMS P30 AR069665 and NIH NIDDK P30 DK116073 (Barbara Davis Center Cell and Tissue Analysis Core at the University of Colorado Diabetes Research Center).

Contributions

DAV, EMS, RAM, SRG and MJZ contributed to design of the study. DAV, EMS, JZ, ALG, DC, CWF, JRM, HH, SHL and LJF contributed to data acquisition. DAV, EMS, JAM, JZ, ALG, CWF, JRM, HH, SHL, JHA, LJF, RAM, KAK, SRG and MJZ contributed to data analysis and interpretation. DAV, EMS, JAM, HH, LJF, RAM, SRG and MJZ contributed to drafting and revising the text. DAV, EMS, JAM, JZ, ALG, DC, CWF, JRM, HH, SHL, KAP, LWM, JHA, LJF, RAM, KAK, SRG and MJZ read and approved the manuscript.

Tables

Pathways Associated with Obesity and Inflammatory Processes			
Ingenuity Canonical Pathway	**-log(B-H *p*-value)**	**B-H *p*-value**	**z-score**
IL-8 Signaling	2.65	2.239E-03	4.264
Dendritic Cell Maturation	3.59	2.570E-04	4.2
Leukocyte Extravasation Signaling	2.96	1.096E-03	3.8
NFkB Signaling	1.40	3.981E-02	3.638
FC Receptor-mediated Phagocytosis in Macrophages and Monocytes	1.76	1.738E-02	3.464
VEGF Signaling	1.53	2.951E-02	3
Production of Nitric Oxide and Reactive Oxygen Species in Macrophages	1.61	2.455E-02	2.982
Type II Diabetes Mellitus Signaling	1.32	4.786E-02	2.714
FcγRIIB Signaling in B Lymphocytes	2.27	5.370E-03	2.333
B Cell Receptor Signaling	2.00	1.000E-02	2.183
Colorectal Cancer Metastasis Signaling	2.27	5.370E-03	3.674

Other Pathways in Top 25			
Ingenuity Canonical Pathway	**-log(B-H *p*-value)**	**B-H *p*-value**	**z-score**
Role of NFAT in Regulation of the Immune Response	2.00	1.000E-02	3.5
Th1 Pathway	2.20	6.310E-03	3.357
Role of Pattern Recognition Receptors in Recognition of Bacteria and Viruses	1.62	2.399E-02	3.162
Tec Kinase Signaling	1.53	2.951E-02	3.051
TREM1 Signaling	1.95	1.122E-02	2.714
Gαq Signaling	1.49	3.236E-02	2.673
Macropinocytosis Signaling	2.11	7.762E-03	2.646
Paxillin Signaling	2.19	6.457E-03	2.53
Actin Cytoskeleton Signaling	2.61	2.455E-03	2.524
Renin-Angiotensin Signaling	1.46	3.467E-02	2.496
iCOS-iCOSL Signaling in T Helper Cells	1.43	3.715E-02	2.496
Signaling by Rho Family GTPases	1.49	3.236E-02	2.357
eNOS Signaling	1.53	2.951E-02	2.324
Phospholipase C Signaling	2.61	2.455E-03	2.236

Table 1: Top 25 pathways identified to be activated in the obese synovium based on IPA. The top 10 pathways associated with obesity and inflammatory processes are listed at the top of the table. B-H p-value = Benjamini-Hochberg adjusted *p*-value.

References

1. Hootman, J.M. and C.G. Helmick, *Projections of US prevalence of arthritis and associated activity limitations.* Arthritis and rheumatism, 2006. **54**(1): p. 226-229.
2. Litwic, A., et al., *Epidemiology and burden of osteoarthritis.* Br Med Bull, 2013. **105**: p. 185-99.
3. Yelin, E., S. Weinstein, and T. King, *The burden of musculoskeletal diseases in the United States.* Semin Arthritis Rheum, 2016. **46**(3): p. 259-260.
4. Martel-Pelletier, J., et al., *Osteoarthritis.* Nat Rev Dis Primers, 2016. **2**: p. 16072.
5. Kelly, T., et al., *Global burden of obesity in 2005 and projections to 2030.* Int J Obes (Lond), 2008. **32**(9): p. 1431-7.
6. Smith, K.B. and M.S. Smith, *Obesity Statistics.* Prim Care, 2016. **43**(1): p. 121-35, ix.
7. Shih, M., et al., *Physical activity in men and women with arthritis National Health Interview Survey, 2002.* Am J Prev Med, 2006. **30**(5): p. 385-93.
8. Lohmander, L.S., et al., *Incidence of severe knee and hip osteoarthritis in relation to different measures of body mass: a population-based prospective cohort study.* Annals of the rheumatic diseases, 2009. **68**(4): p. 490-496.
9. Mooney, R.A., et al., *High-fat diet accelerates progression of osteoarthritis after meniscal/ligamentous injury.* Arthritis Res Ther, 2011. **13**(6): p. R198.
10. Hamada, D., et al., *Suppressive Effects of Insulin on Tumor Necrosis Factor–Dependent Early Osteoarthritic Changes Associated With Obesity and Type 2 Diabetes Mellitus.* Arthritis & Rheumatology, 2016. **68**(6): p. 1392-1402.
11. Raghu, H., et al., *CCL2/CCR2, but not CCL5/CCR5, mediates monocyte recruitment, inflammation and cartilage destruction in osteoarthritis.* Ann Rheum Dis, 2017. **76**(5): p. 914-922.
12. Rowe, M.A., et al., *Reduced Osteoarthritis Severity in Aged Mice With Deletion of Macrophage Migration Inhibitory Factor.* Arthritis & rheumatology (Hoboken, N.J.), 2017. **69**(2): p. 352-361.
13. Griffin, T.M., et al., *Extreme obesity due to impaired leptin signaling in mice does not cause knee osteoarthritis.* Arthritis Rheum, 2009. **60**(10): p. 2935-44.
14. Griffin, T.M., et al., *Induction of osteoarthritis and metabolic inflammation by a very high-fat diet in mice: Effects of short-term exercise.* Arthritis & Rheumatism, 2012. **64**(2): p. 443-453.
15. Louer, C.R., et al., *Diet-induced obesity significantly increases the severity of posttraumatic arthritis in mice.* Arthritis Rheum, 2012. **64**(10): p. 3220-30.
16. Griffin, T.M., et al., *Induction of osteoarthritis and metabolic inflammation by a very high-fat diet in mice: effects of short-term exercise.* Arthritis Rheum, 2012. **64**(2): p. 443-53.
17. Scanzello, C.R. and S.R. Goldring, *The role of synovitis in osteoarthritis pathogenesis.* Bone, 2012. **51**(2): p. 249-57.
18. Sellam, J. and F. Berenbaum, *The role of synovitis in pathophysiology and clinical symptoms of osteoarthritis.* Nat Rev Rheumatol, 2010. **6**(11): p. 625-35.
19. Loeser, R.F., et al., *Osteoarthritis: a disease of the joint as an organ.* Arthritis Rheum, 2012. **64**(6): p. 1697-707.
20. Scheithauer, T.P.M., et al., *Gut Microbiota as a Trigger for Metabolic Inflammation in Obesity and Type 2 Diabetes.* Front Immunol, 2020. **11**: p. 571731.
21. Ridaura, V.K., et al., *Gut microbiota from twins discordant for obesity modulate metabolism in mice.* Science, 2013. **341**(6150): p. 1241214.

22. Turnbaugh, P.J., et al., *An obesity-associated gut microbiome with increased capacity for energy harvest.* Nature, 2006. **444**(7122): p. 1027-31.
23. Khan, S., et al., *Emerging concepts in intestinal immune control of obesity-related metabolic disease.* Nat Commun, 2021. **12**(1): p. 2598.
24. Friedrich, K., et al., *Perturbation of the Monocyte Compartment in Human Obesity.* Front Immunol, 2019. **10**: p. 1874.
25. Liu, R. and B.S. Nikolajczyk, *Tissue Immune Cells Fuel Obesity-Associated Inflammation in Adipose Tissue and Beyond.* Front Immunol, 2019. **10**: p. 1587.
26. Weitman, E.S., et al., *Obesity impairs lymphatic fluid transport and dendritic cell migration to lymph nodes.* PLoS One, 2013. **8**(8): p. e70703.
27. Luck, H., et al., *Gut-associated IgA(+) immune cells regulate obesity-related insulin resistance.* Nat Commun, 2019. **10**(1): p. 3650.
28. Kawano, Y., et al., *Colonic Pro-inflammatory Macrophages Cause Insulin Resistance in an Intestinal Ccl2/Ccr2-Dependent Manner.* Cell Metab, 2016. **24**(2): p. 295-310.
29. Schott, E.M., et al., *Targeting the gut microbiome to treat the osteoarthritis of obesity.* JCI Insight, 2018. **3**(8).
30. Collins, K.H., et al., *Taxonomic changes in the gut microbiota are associated with cartilage damage independent of adiposity, high fat diet, and joint injury.* Scientific Reports, 2021. **11**(1): p. 14560.
31. Guss, J.D., et al., *The effects of metabolic syndrome, obesity, and the gut microbiome on load-induced osteoarthritis.* Osteoarthritis Cartilage, 2019. **27**(1): p. 129-139.
32. Collins, K.H., et al., *Relationship between inflammation, the gut microbiota, and metabolic osteoarthritis development: studies in a rat model.* Osteoarthritis Cartilage, 2015. **23**(11): p. 1989-98.
33. Hamada, D., et al., *Suppressive Effects of Insulin on Tumor Necrosis Factor-Dependent Early Osteoarthritic Changes Associated With Obesity and Type 2 Diabetes Mellitus.* Arthritis Rheumatol, 2016. **68**(6): p. 1392-402.
34. Da, R.R., et al., *B cell clonal expansion and somatic hypermutation of Ig variable heavy chain genes in the synovial membrane of patients with osteoarthritis.* J Immunol, 2007. **178**(1): p. 557-65.
35. Dennis, G., Jr., et al., *Synovial phenotypes in rheumatoid arthritis correlate with response to biologic therapeutics.* Arthritis Res Ther, 2014. **16**(2): p. R90.
36. Stojanov, S., A. Berlec, and B. Štrukelj, *The Influence of Probiotics on the Firmicutes/Bacteroidetes Ratio in the Treatment of Obesity and Inflammatory Bowel disease.* Microorganisms, 2020. **8**(11).
37. Crovesy, L., D. Masterson, and E.L. Rosado, *Profile of the gut microbiota of adults with obesity: a systematic review.* European Journal of Clinical Nutrition, 2020. **74**(9): p. 1251-1262.
38. Zagato, E., et al., *Endogenous murine microbiota member Faecalibaculum rodentium and its human homologue protect from intestinal tumour growth.* Nat Microbiol, 2020. **5**(3): p. 511-524.
39. Khan, S., et al., *Emerging concepts in intestinal immune control of obesity-related metabolic disease.* Nature Communications, 2021. **12**(1): p. 2598.
40. Gierman, L.M., et al., *Metabolic stress–induced inflammation plays a major role in the development of osteoarthritis in mice.* Arthritis & Rheumatism, 2012. **64**(4): p. 1172-1181.

41. June, R.K., et al., *Emerging role of metabolic signaling in synovial joint remodeling and osteoarthritis.* J Orthop Res, 2016. **34**(12): p. 2048-2058.
42. Murphy, L., et al., *Lifetime risk of symptomatic knee osteoarthritis.* Arthritis Rheum, 2008. **59**(9): p. 1207-13.
43. Hu, W., et al., *Microenvironment in subchondral bone: predominant regulator for the treatment of osteoarthritis.* Ann Rheum Dis, 2021. **80**(4): p. 413-422.
44. Hügle, T. and J. Geurts, *What drives osteoarthritis?-synovial versus subchondral bone pathology.* Rheumatology (Oxford), 2017. **56**(9): p. 1461-1471.
45. van der Kraan, P.M. and W.B. van den Berg, *Chondrocyte hypertrophy and osteoarthritis: role in initiation and progression of cartilage degeneration?* Osteoarthritis Cartilage, 2012. **20**(3): p. 223-32.
46. Sun, A.R., et al., *Obesity-associated metabolic syndrome spontaneously induces infiltration of pro-inflammatory macrophage in synovium and promotes osteoarthritis.* PLoS One, 2017. **12**(8): p. e0183693.
47. Wu, C.L., et al., *Conditional Macrophage Depletion Increases Inflammation and Does Not Inhibit the Development of Osteoarthritis in Obese Macrophage Fas-Induced Apoptosis-Transgenic Mice.* Arthritis Rheumatol, 2017. **69**(9): p. 1772-1783.
48. Sun, A.R., et al., *Pro-resolving lipid mediator ameliorates obesity induced osteoarthritis by regulating synovial macrophage polarisation.* Sci Rep, 2019. **9**(1): p. 426.
49. Gregor, M.F. and G.S. Hotamisligil, *Inflammatory mechanisms in obesity.* Annu Rev Immunol, 2011. **29**: p. 415-45.
50. Hotamisligil, G.S., N.S. Shargill, and B.M. Spiegelman, *Adipose expression of tumor necrosis factor-alpha: direct role in obesity-linked insulin resistance.* Science, 1993. **259**(5091): p. 87-91.
51. Wellen, K.E. and G.S. Hotamisligil, *Obesity-induced inflammatory changes in adipose tissue.* J Clin Invest, 2003. **112**(12): p. 1785-8.
52. Boden, G., *Obesity, insulin resistance and free fatty acids.* Curr Opin Endocrinol Diabetes Obes, 2011. **18**(2): p. 139-43.
53. Ginter, E. and V. Simko, *Type 2 diabetes mellitus, pandemic in 21st century.* Adv Exp Med Biol, 2012. **771**: p. 42-50.
54. Bastard, J.P., et al., *Adipose tissue IL-6 content correlates with resistance to insulin activation of glucose uptake both in vivo and in vitro.* J Clin Endocrinol Metab, 2002. **87**(5): p. 2084-9.
55. Aljada, A., et al., *Insulin inhibits NFkappaB and MCP-1 expression in human aortic endothelial cells.* J Clin Endocrinol Metab, 2001. **86**(1): p. 450-3.
56. Andersson, C.X., et al., *Insulin antagonizes interleukin-6 signaling and is anti-inflammatory in 3T3-L1 adipocytes.* J Biol Chem, 2007. **282**(13): p. 9430-5.
57. Roman-Blas, J.A. and S.A. Jimenez, *NF-kappaB as a potential therapeutic target in osteoarthritis and rheumatoid arthritis.* Osteoarthritis Cartilage, 2006. **14**(9): p. 839-48.
58. Rigoglou, S. and A.G. Papavassiliou, *The NF-kappaB signalling pathway in osteoarthritis.* Int J Biochem Cell Biol, 2013. **45**(11): p. 2580-4.
59. Kobayashi, H., et al., *Biphasic regulation of chondrocytes by Rela through induction of anti-apoptotic and catabolic target genes.* Nat Commun, 2016. **7**: p. 13336.
60. Matsukawa, A., et al., *Neutrophil accumulation and activation by homologous IL-8 in rabbits. IL-8 induces destruction of cartilage and production of IL-1 and IL-1 receptor antagonist in vivo.* J Immunol, 1995. **154**(10): p. 5418-25.

61. Borzi, R.M., et al., *Chemokines in cartilage degradation.* Clin Orthop Relat Res, 2004(427 Suppl): p. S53-61.
62. McInnes, I.B. and G. Schett, *The pathogenesis of rheumatoid arthritis.* N Engl J Med, 2011. **365**(23): p. 2205-19.
63. Yap, H.Y., et al., *Pathogenic Role of Immune Cells in Rheumatoid Arthritis: Implications in Clinical Treatment and Biomarker Development.* Cells, 2018. **7**(10).
64. Zhang, F., et al., *Defining inflammatory cell states in rheumatoid arthritis joint synovial tissues by integrating single-cell transcriptomics and mass cytometry.* Nat Immunol, 2019. **20**(7): p. 928-942.
65. DeFuria, J., et al., *B cells promote inflammation in obesity and type 2 diabetes through regulation of T-cell function and an inflammatory cytokine profile.* Proc Natl Acad Sci U S A, 2013. **110**(13): p. 5133-8.
66. Winer, D.A., et al., *B cells promote insulin resistance through modulation of T cells and production of pathogenic IgG antibodies.* Nat Med, 2011. **17**(5): p. 610-7.
67. Marston, B., A. Palanichamy, and J.H. Anolik, *B cells in the pathogenesis and treatment of rheumatoid arthritis.* Curr Opin Rheumatol, 2010. **22**(3): p. 307-15.
68. Song, Y.W. and E.H. Kang, *Autoantibodies in rheumatoid arthritis: rheumatoid factors and anticitrullinated protein antibodies.* Qjm, 2010. **103**(3): p. 139-46.
69. Nerviani, A. and C. Pitzalis, *Role of chemokines in ectopic lymphoid structures formation in autoimmunity and cancer.* Journal of Leukocyte Biology, 2018. **104**(2): p. 333-341.
70. Manzo, A., et al., *Secondary and ectopic lymphoid tissue responses in rheumatoid arthritis: from inflammation to autoimmunity and tissue damage/remodeling.* Immunological Reviews, 2010. **233**(1): p. 267-285.
71. Humby, F., et al., *Synovial cellular and molecular signatures stratify clinical response to csDMARD therapy and predict radiographic progression in early rheumatoid arthritis patients.* Ann Rheum Dis, 2019. **78**(6): p. 761-772.
72. Jones, G.W., et al., *Interleukin-27 inhibits ectopic lymphoid-like structure development in early inflammatory arthritis.* Journal of Experimental Medicine, 2015. **212**(11): p. 1793-1802.
73. Boulangé, C.L., et al., *Impact of the gut microbiota on inflammation, obesity, and metabolic disease.* Genome Med, 2016. **8**(1): p. 42.
74. Donaldson, G.P., S.M. Lee, and S.K. Mazmanian, *Gut biogeography of the bacterial microbiota.* Nat Rev Microbiol, 2016. **14**(1): p. 20-32.
75. Bäckhed, F., et al., *The gut microbiota as an environmental factor that regulates fat storage.* Proc Natl Acad Sci U S A, 2004. **101**(44): p. 15718-23.
76. Muscogiuri, G., et al., *Gut microbiota: a new path to treat obesity.* International Journal of Obesity Supplements, 2019. **9**(1): p. 10-19.
77. Liu, R., et al., *Gut microbiome and serum metabolome alterations in obesity and after weight-loss intervention.* Nature Medicine, 2017. **23**(7): p. 859-868.
78. Rabot, S., et al., *Germ-free C57BL/6J mice are resistant to high-fat-diet-induced insulin resistance and have altered cholesterol metabolism.* Faseb j, 2010. **24**(12): p. 4948-59.
79. Fujisaka, S., et al., *Antibiotic effects on gut microbiota and metabolism are host dependent.* J Clin Invest, 2016. **126**(12): p. 4430-4443.
80. Bai, S., et al., *Gut Microbiota-Related Inflammation Factors as a Potential Biomarker for Diagnosing Major Depressive Disorder.* Front Cell Infect Microbiol, 2022. **12**: p. 831186.

81. Arboleya, S., et al., *Gut Bifidobacteria Populations in Human Health and Aging.* Front Microbiol, 2016. **7**: p. 1204.
82. Zheng, D., T. Liwinski, and E. Elinav, *Interaction between microbiota and immunity in health and disease.* Cell Research, 2020. **30**(6): p. 492-506.
83. Round, J.L. and S.K. Mazmanian, *The gut microbiota shapes intestinal immune responses during health and disease.* Nat Rev Immunol, 2009. **9**(5): p. 313-23.
84. Kiner, E., et al., *Gut CD4(+) T cell phenotypes are a continuum molded by microbes, not by T(H) archetypes.* Nat Immunol, 2021. **22**(2): p. 216-228.
85. Luck, H., et al., *Gut-associated IgA(+) immune cells regulate obesity-related insulin resistance.* Nat Commun, 2019. **10**(1): p. 3650.
86. Luck, H., et al., *Regulation of obesity-related insulin resistance with gut anti-inflammatory agents.* Cell Metab, 2015. **21**(4): p. 527-42.
87. Garidou, L., et al., *The Gut Microbiota Regulates Intestinal CD4 T Cells Expressing RORγt and Controls Metabolic Disease.* Cell Metab, 2015. **22**(1): p. 100-12.
88. Hong, C.P., et al., *Gut-Specific Delivery of T-Helper 17 Cells Reduces Obesity and Insulin Resistance in Mice.* Gastroenterology, 2017. **152**(8): p. 1998-2010.
89. Monteiro-Sepulveda, M., et al., *Jejunal T Cell Inflammation in Human Obesity Correlates with Decreased Enterocyte Insulin Signaling.* Cell Metab, 2015. **22**(1): p. 113-24.
90. Rojas, O.L., et al., *Recirculating Intestinal IgA-Producing Cells Regulate Neuroinflammation via IL-10.* Cell, 2019. **176**(3): p. 610-624.e18.
91. Moro-Sibilot, L., et al., *Mouse and Human Liver Contain Immunoglobulin A-Secreting Cells Originating From Peyer's Patches and Directed Against Intestinal Antigens.* Gastroenterology, 2016. **151**(2): p. 311-23.
92. Rosser, E.C., et al., *Regulatory B cells are induced by gut microbiota-driven interleukin-1β and interleukin-6 production.* Nat Med, 2014. **20**(11): p. 1334-9.
93. Frasca, D., et al., *Obesity induces pro-inflammatory B cells and impairs B cell function in old mice.* Mech Ageing Dev, 2017. **162**: p. 91-99.
94. Tajik, N., et al., *Targeting zonulin and intestinal epithelial barrier function to prevent onset of arthritis.* Nature Communications, 2020. **11**(1): p. 1995.
95. Ruiz, L., et al., *Bifidobacteria and Their Molecular Communication with the Immune System.* Front Microbiol, 2017. **8**: p. 2345.
96. Kandasamy, S., et al., *Lactobacilli and Bifidobacteria enhance mucosal B cell responses and differentially modulate systemic antibody responses to an oral human rotavirus vaccine in a neonatal gnotobiotic pig disease model.* Gut Microbes, 2014. **5**(5): p. 639-51.
97. Moya-Pérez, A., A. Neef, and Y. Sanz, *Bifidobacterium pseudocatenulatum CECT 7765 Reduces Obesity-Associated Inflammation by Restoring the Lymphocyte-Macrophage Balance and Gut Microbiota Structure in High-Fat Diet-Fed Mice.* PLoS One, 2015. **10**(7): p. e0126976.
98. Nowotschin, S. and A.-K. Hadjantonakis, *Use of KikGR a photoconvertible green-to-red fluorescent protein for cell labeling and lineage analysis in ES cells and mouse embryos.* BMC Developmental Biology, 2009. **9**(1): p. 49.
99. Nakanishi, Y., et al., *Regulatory T cells with superior immunosuppressive capacity emigrate from the inflamed colon to draining lymph nodes.* Mucosal Immunology, 2018. **11**(2): p. 437-448.

100. Morton, A.M., et al., *Endoscopic photoconversion reveals unexpectedly broad leukocyte trafficking to and from the gut.* Proc Natl Acad Sci U S A, 2014. **111**(18): p. 6696-701.
101. Porter, C., M. Ennamorati, and N. Jain, *In Vivo Photolabeling of Cells in the Colon to Assess Migratory Potential of Hematopoietic Cells in Neonatal Mice.* J Vis Exp, 2018(138).
102. Lefferts, A.R., et al., *Cytokine competent gut-joint migratory T Cells contribute to inflammation in the joint.* Front Immunol, 2022. **13**: p. 932393.
103. Villiger, P.M., R. Terkeltaub, and M. Lotz, *Production of monocyte chemoattractant protein-1 by inflamed synovial tissue and cultured synoviocytes.* J Immunol, 1992. **149**(2): p. 722-7.
104. Dar, Q.A., et al., *Daily oral consumption of hydrolyzed type 1 collagen is chondroprotective and anti-inflammatory in murine posttraumatic osteoarthritis.* PLoS One, 2017. **12**(4): p. e0174705.
105. Sadeghipour, A. and P. Babaheidarian, *Making Formalin-Fixed, Paraffin Embedded Blocks.* Methods Mol Biol, 2019. **1897**: p. 253-268.
106. Akitsu, A. and Y. Iwakura, *Isolation of Joint-infiltrating Cells.* Bio-protocol, 2016. **6**(17): p. e1911.
107. Holm, J.B., et al., *Ultrahigh-Throughput Multiplexing and Sequencing of >500-Base-Pair Amplicon Regions on the Illumina HiSeq 2500 Platform.* mSystems, 2019. **4**(1).
108. Bolyen, E., et al., *Reproducible, interactive, scalable and extensible microbiome data science using QIIME 2.* Nat Biotechnol, 2019. **37**(8): p. 852-857.
109. Bokulich, N.A., et al., *Optimizing taxonomic classification of marker-gene amplicon sequences with QIIME 2's q2-feature-classifier plugin.* Microbiome, 2018. **6**(1): p. 90.
110. Kruskal, W.H. and W.A. Wallis, *Use of Ranks in One-Criterion Variance Analysis.* Journal of the American Statistical Association, 1952. **47**(260): p. 583-621.
111. Segata, N., et al., *Metagenomic biomarker discovery and explanation.* Genome Biol, 2011. **12**(6): p. R60.

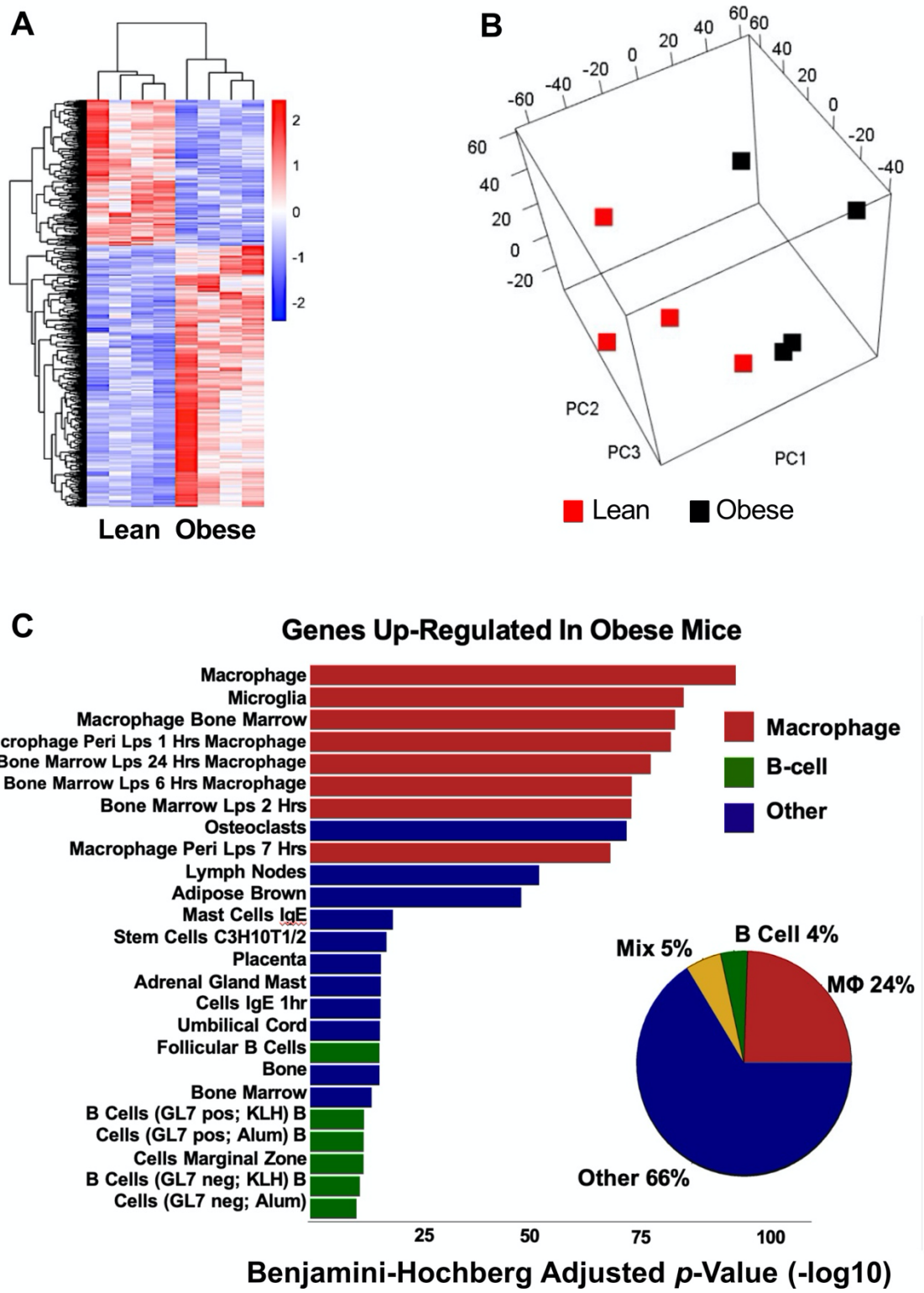
A
2
1
0
-1
-2
Lean Obese
B
60
40
20
0
-20
-40
-60
PC2
PC3
PC1
Lean
Obese
C
Genes Up-Regulated In Obese Mice
Macrophage
Microglia
Macrophage Bone Marrow
Macrophage Peri Lps 1 Hrs Macrophage
Bone Marrow Lps 24 Hrs Macrophage
Bone Marrow Lps 6 Hrs Macrophage
Bone Marrow Lps 2 Hrs
Osteoclasts
Macrophage Peri Lps 7 Hrs
Lymph Nodes
Adipose Brown
Mast Cells IgE
Stem Cells C3H10T1/2
Placenta
Adrenal Gland Mast
Cells IgE 1hr
Umbilical Cord
Follicular B Cells
Bone
Bone Marrow
B Cells (GL7 pos; KLH) B
Cells (GL7 pos; Alum) B
Cells Marginal Zone
B Cells (GL7 neg; KLH) B
Cells (GL7 neg; Alum)
Macrophage
B-cell
Other
Mix 5%
B Cell 4%
MΦ 24%
Other 66%
25
50
75
100
Benjamini-Hochberg Adjusted p-Value (-log10)

Figure 1

Figure 1: RNA-Seq analysis of lean and obese synovial transcriptomes identifies mediators of early synovial pathogenic change. (**A**) Hierarchically clustered and row scaled heat map displaying the significantly differentially expressed genes between lean and obese samples. (**B**) Principal Component Analysis illustrates that PC1 is able to delineate the lean and obese samples based on global gene expression. (**C**) Cell type enrichment analysis identified a macrophage signature driven by 24% of genes upregulated in obese synovium. An additional 9% of up-regulated genes drive a B cell enrichment or a mix of both B cell and macrophage.

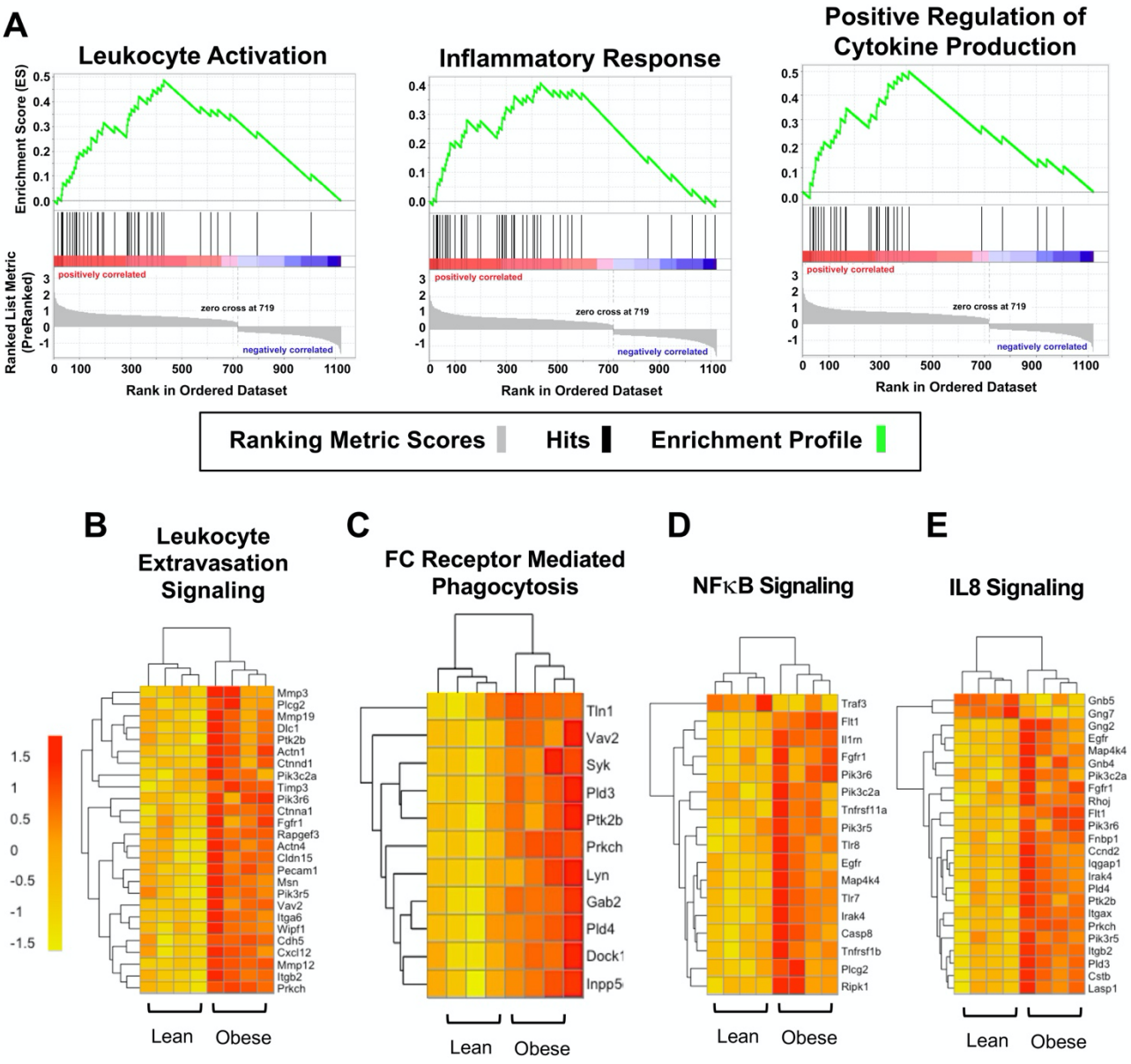
A
Leukocyte Activation
Inflammatory Response
Positive Regulation of Cytokine Production
Enrichment Score (ES)
Ranked List Metric (PreRanked)
positively correlated
zero cross at 719
negatively correlated
Rank in Ordered Dataset
Ranking Metric Scores
Hits
Enrichment Profile
B
Leukocyte Extravasation Signaling
Mmp3
Plcg2
Mmp19
Dlc1
Ptk2b
Actn1
Ctnnd1
Pik3c2a
Timp3
Pik3r6
Ctnna1
Fgfr1
Rapgef3
Actn4
Cldn15
Pecam1
Msn
Pik3r5
Vav2
Itga6
Wipf1
Cdh5
Cxcl12
Mmp12
Itgb2
Prkch
Lean
Obese
C
FC Receptor Mediated Phagocytosis
Tln1
Vav2
Syk
Pld3
Ptk2b
Prkch
Lyn
Gab2
Pld4
Dock1
Inpp5
Lean
Obese
D
NFκB Signaling
Traf3
Flt1
Il1rn
Fgfr1
Pik3r6
Pik3c2a
Tnfrsf11a
Pik3r5
Tlr8
Egfr
Map4k4
Tlr7
Irak4
Casp8
Tnfrsf1b
Plcg2
Ripk1
Lean
Obese
E
IL8 Signaling
Gnb5
Gng7
Gng2
Egfr
Map4k4
Gnb4
Pik3c2a
Fgfr1
Rhoj
Flt1
Pik3r6
Fnbp1
Ccnd2
Iqgap1
Irak4
Pld4
Ptk2b
Itgax
Prkch
Pik3r5
Itgb2
Pld3
Cstb
Lasp1
Lean
Obese

Figure 2

Figure 2: Pathway enrichment analysis identify several immune and inflammatory enrichments. (**A**) PreRanked Gene Set Enrichment Analysis (GSEA) identified significant results based on the normalized enrichment score (NES) for GO terms including Leukocyte Activation, Inflammatory Response and Positive Regulation of Cytokine Production. Hierarchically clustered and row scaled heat maps displaying the genes annotating to Leukocyte Extravasation Signaling (**B**), FC Receptor Mediated Phagocytosis (**C**), NFkB signaling (**D**), and IL8 Signaling (**E**). Notably, all genes that annotate to each of these pathways are altered in the analyzed samples.

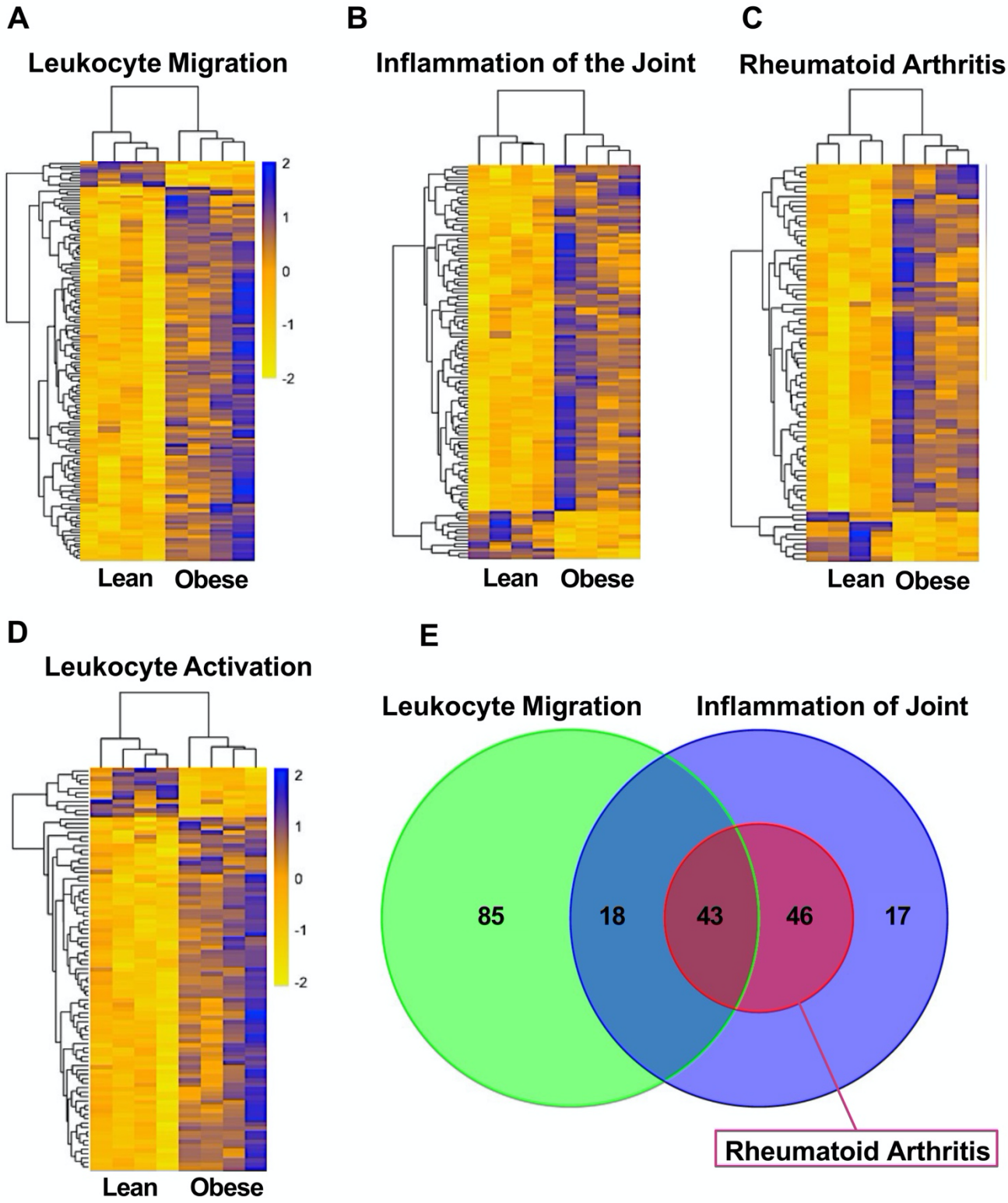
A
Leukocyte Migration
2
1
0
-1
-2
Lean
Obese
B
Inflammation of the Joint
Lean
Obese
C
Rheumatoid Arthritis
Lean
Obese
D
Leukocyte Activation
2
1
0
-1
-2
Lean
Obese
E
Leukocyte Migration
Inflammation of Joint
85
18
43
46
17
Rheumatoid Arthritis

Figure 3

Figure 3: Significant enrichment of Diseases and Functions based on differentially expressed genes. Hierarchically clustered and row scaled heat maps displaying the genes underlying Leukocyte Migration (**A**), Inflammation of the Joint (**B**), Rheumatoid Arthritis (**C**), and Leukocyte Activation (**E**). 3-way Venn diagram suggests the Rheumatoid Arthritis enrichment is driven by genes that completely overlap with "Inflammation of the Joint" and "Leukocyte Migration" enrichments.

A

	Annotation	p-value	z-score
Canonical Pathways	B Cell Receptor Signaling	0.010	2.183
	FcγRIIB Signaling in B Lymphocytes	0.005	2.333
	PI3K Signaling in B Lymphocytes	0.049	1.155
Diseases & Functions	Quantity of B lymphocytes	1.450E-05	0.89
	proliferation of B-lymphocyte Derived Cell Lines	1.270E-04	3.075
Cell Type Enrichment	B cells	1.582E-15	NA

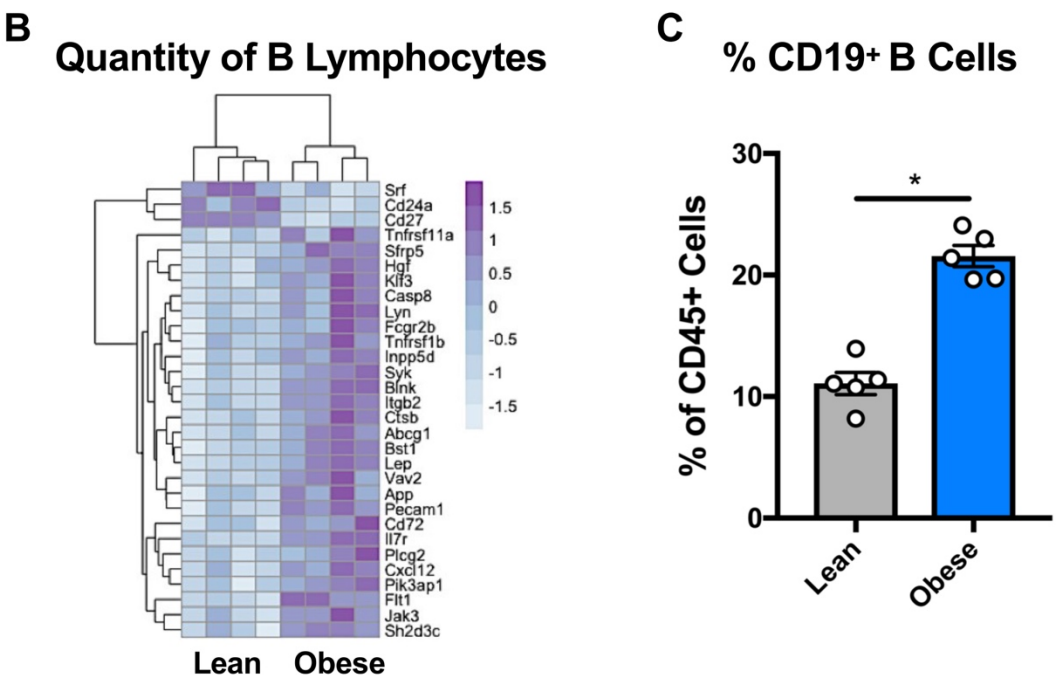

Figure 4

Figure 4: The B cell is a novel mediator of the early pathogenesis of the OA of obesity. (**A**) Table displaying all B cell related significant and sometimes activated (z-score >=2) enrichments identified. (**B**) Hierarchically clustered and row scaled heat maps displaying the genes underlying 'Quantity of B Lymphocytes'. (**C**) CD3-CD19+ B cells are significantly increased in the obese compared to lean synovium (N=5, one-tailed t test, *p=0.0092).

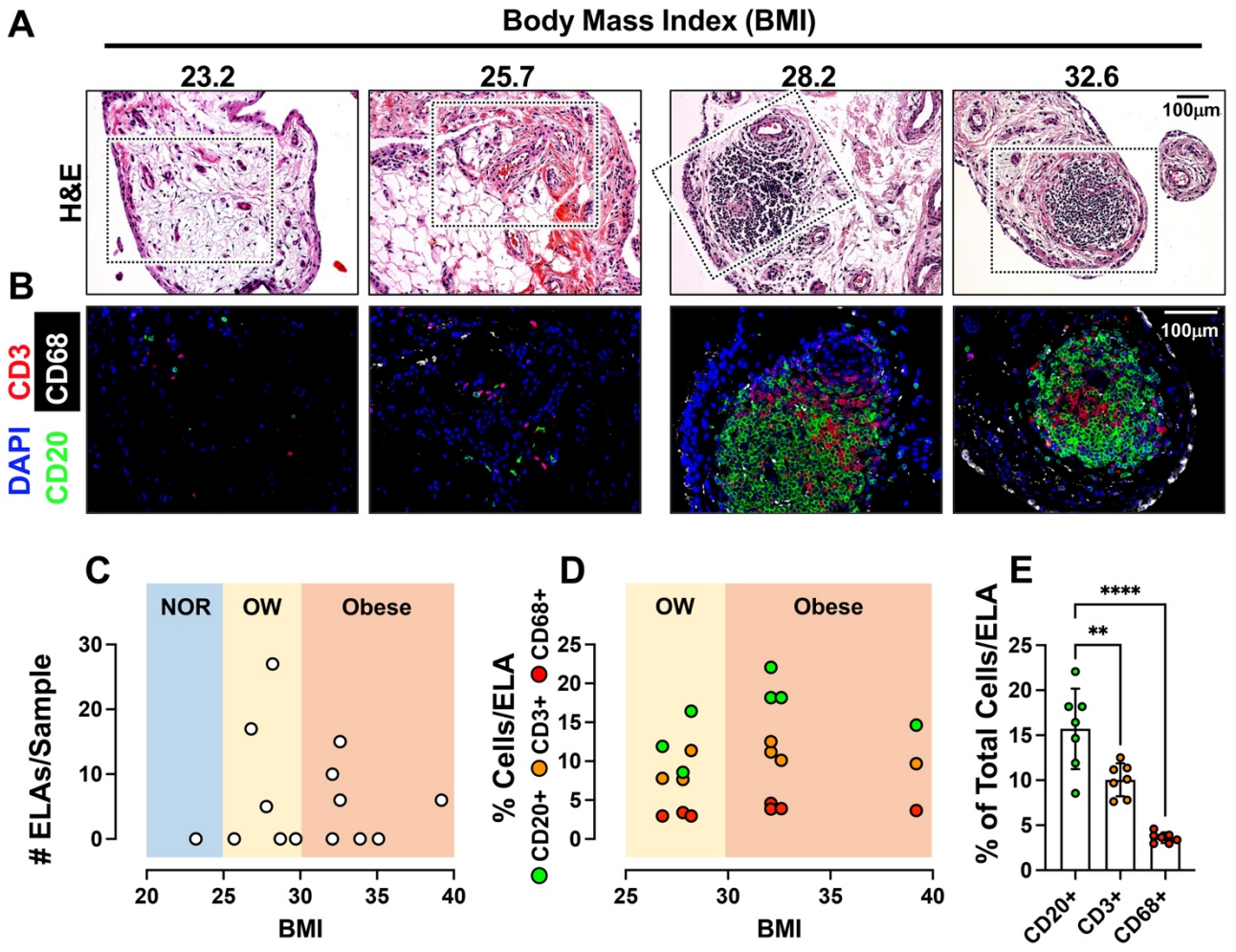
A
Body Mass Index (BMI)
23.2
25.7
28.2
32.6
H&E
100µm
B
CD3
CD68
DAPI
CD20
100µm
C
NOR
OW
Obese
ELAs/Sample
BMI
D
OW
Obese
% Cells/ELA
CD20+ CD3+ CD68+
BMI
E
****
**
% of Total Cells/ELA
CD20+
CD3+
CD68+

Figure 5

Figure 5: ELAs containing B cells are present in the synovia of overweight/obese OA patients. (**A**) and (**B**) depict representative synovial tissue samples collected from patients undergoing total knee arthroplasty for a diagnosis of OA. The top row (**A**) depicts classic H&E stains with the bottom row (**B**) reporting on immunofluorescence staining of CD20+, CD4+ and CD68+ inflammatory cell infiltrates in the boxed areas denoted on the H&E stains in (**A**). A summary of ELA frequency versus BMI in a cadre of patients (normal, <25; overweight, between 25 and 30; obese, >30) is presented in (**C**). A dot plot summarizing the % of each cell type (CD20+ B cells, CD 4+ T cells and CD68+ monocyte/macrophage lineage cells) is displayed across all samples containing ELAs (**D**) with the % of each cell type quantified for statistical analysis (**E**, 2 way ANOVA with a Tukey multiple comparisons test, N=7, $^{**}p<0.01$, $^{****}p<0.0001$).

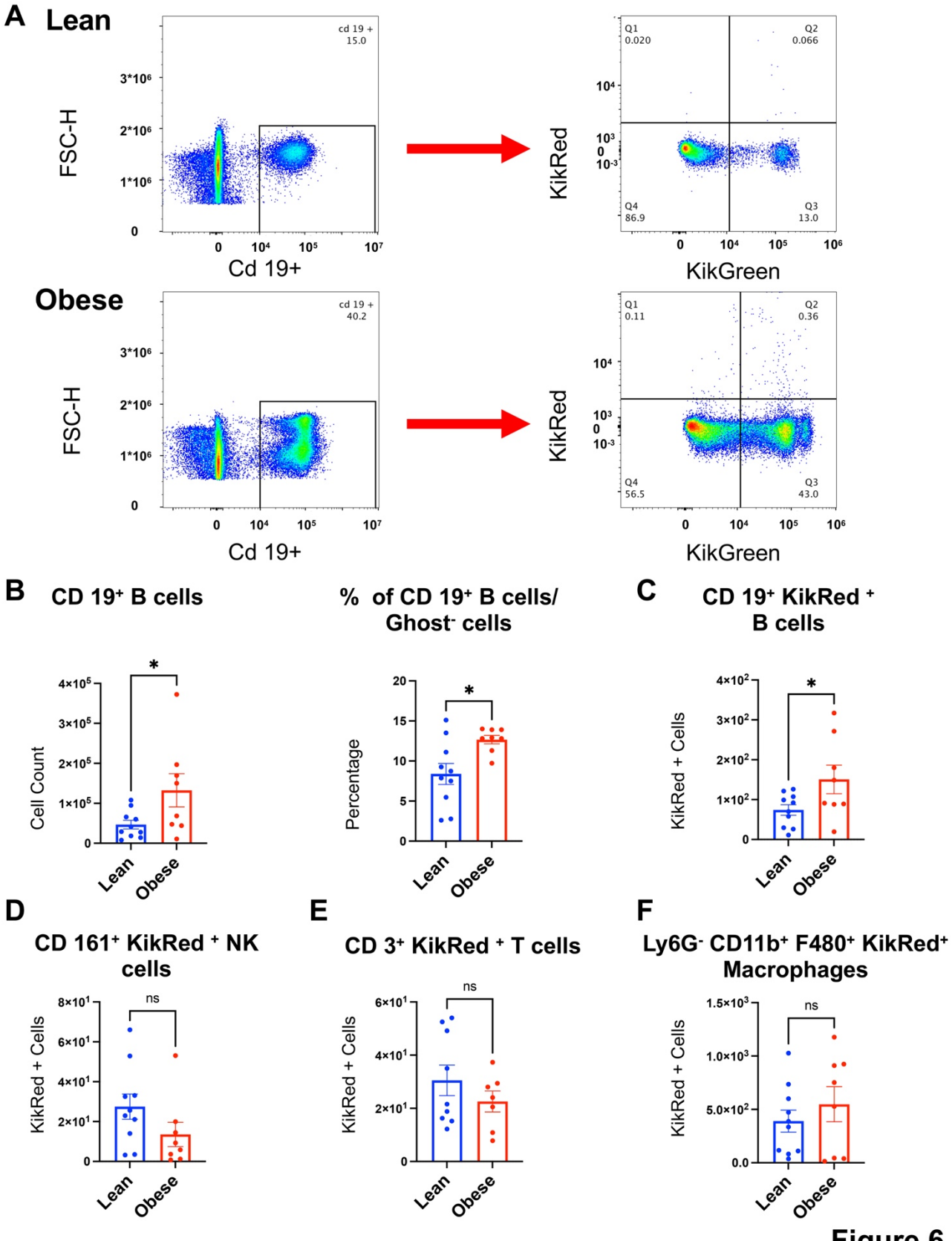
A
Lean
cd 19 +
15.0
FSC-H
Cd 19+
KikRed
KikGreen
Q1
0.020
Q2
0.066
Q4
86.9
Q3
13.0
Obese
cd 19 +
40.2
Q1
0.11
Q2
0.36
Q4
56.5
Q3
43.0
B
CD 19+ B cells
Cell Count
% of CD 19+ B cells/ Ghost- cells
Percentage
C
CD 19+ KikRed + B cells
KikRed + Cells
D
CD 161+ KikRed + NK cells
E
CD 3+ KikRed + T cells
F
Ly6G- CD11b+ F480+ KikRed+ Macrophages
ns
Lean
Obese

Figure 6

Figure 6: Obesity leads to an increase in the number of CD19+ B cells migrating from the gut to the joint. Joints from 4-5 KikGR animals consuming the high-fat or low-fat diet were harvested 72 hours after photoconversion and prepared for flow cytometry. Representative Pseudo color plots are displayed (**A**), with CD19+ B cell populations further gated to display KikRed+ cells for quantification. Quantification of these representative plots is shown in the bar graphs depicting the total number and the percentage of CD19+ B cells present within the joint (**B**), the total number and percentage of KikRed+ CD19+ B cells (**C**) the number of KikRed+ CD161 natural killer cells (**D**), the number of KikRed+ CD3+ T cells (**E**), and the number of KikRed+ Ly6g-CD11b+ F480+ macrophages (**F**). Significant differences between groups (**C**) - (**F**) were identified using an unpaired t-test; *p<0.05, **p<0.01, N=7-10 where each point represents a single joint.

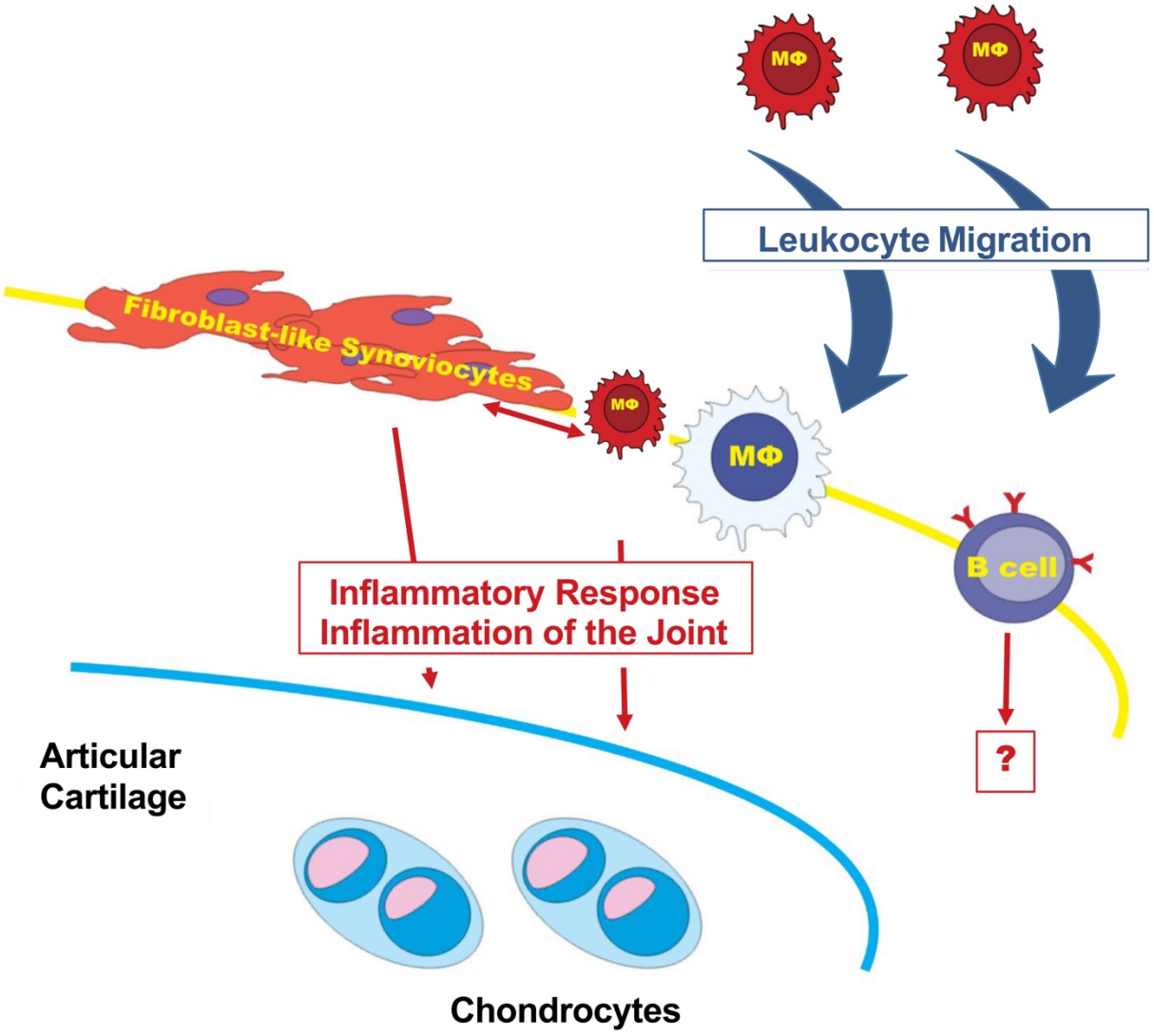
МΦ
МΦ
Leukocyte Migration
Fibroblast-like Synoviocytes
МΦ
МΦ
B cell
Inflammatory Response
Inflammation of the Joint
?
Articular
Cartilage
Chondrocytes

Figure 7

Figure 7: Synovial inflammation develops in obesity. Within the obese joint there is an increase in the number of macrophages and leukocytes in the synovium. These cells may interact with resident fibroblast-like synoviocytes, resulting in potentiation of an inflammatory response. Notably, the number of B cells is increased in the obese joint with potential impacts on the development of OA that are yet to be determined.